DC PULSE-POWERED MICRODISCHARGES ON PLANAR ELECTRODES AND THEIR USE IN VAPOR AND LIQUID PHASE CHEMICAL SENSING IN AMBIENT AIR

by

Bhaskar Mitra

A dissertation submitted in partial fulfillment
of the requirements for the degree of
Doctor of Philosophy
(Electrical Engineering)
in The University of Michigan
2008

Doctoral Committee:

Professor Yogesh B. Gianchandani, Chair
Professor Kensall D. Wise
Professor Fred L. Terry Jr.
Associate Professor John E. Foster
Assistant Professor Michel M. Maharbiz

2008

To ma and baba

TABLE OF CONTENTS

LIST OF FIGURES

LIST OF TABLES

LIST OF SYMBOLS

$\bar{c}$	Particle speed
C_e	Electron generation rate
C_+	Ion generation rate
k	Boltzmann's constant
T	Temperature
$\sigma(v_r)$	Collision cross-section
a_{12}	Sum of the radii of incident and target particles
n_g	Number of gas molecules per unit volume
σ	Collision cross-section
λ	Mean free-path
ν	Collision frequency
v_i	Initial velocity of incident particle
m_i	Mass of incident particle
u_i	Final velocity of incident particle
u_t	Final velocity of target particle
θ	Angle of incidence
E_t/E_i	Fraction of Energy transferred in an elastic collision
eV^*	Excitation potential of atom/molecule
E_s	Threshold energy for excitation

σ_p	Cross-section for photoionization
eV_i	Ionization potential
eV_m	Potential of metastable state
f	Acceleration due to the electric field
F_p	Hydrodynamic Force
P	Pressure
F_{el}	Electromagnetic Force
$\mathbf{v_e}$	Average velocity of electron fluid
$\mathbf{v_n}$	Average velocity of neutral fluid
$\mathbf{v_i}$	Average velocity of ion fluid
F_f	Frictional force between fluids
n_i	Ion density
n_n	Neutral density
n_e	Electron density
α_{ie}	Frictional coefficients for electron-ion interactions
α_{ne}	Frictional coefficients for electron-neutral interactions
v_{ce}	Effective collision frequency for electrons
v_{ci}	Effective collision frequency for ions
v_{ce}	Effective collision frequency for neutrals
$f(\mathbf{r}, \mathbf{v}, t)$	Distribution function in six-dimensional phase space
$\mathbf{u_e}$	Instantaneous velocity (not average) of the electron in phase space
$\mathbf{u_i}$	Instantaneous velocity (not average) of the ion in phase space
$\mathbf{u_n}$	Instantaneous velocity (not average) of the neutral in phase space

∇_v	Gradient in velocity space

Abstract

This report explores DC pulse-powered planar microdischarges and their possible use in handheld chemical sensing systems. Two-electrode discharges are considered, and their temporal evolution is evaluated. Three-electrode discharges are considered for controlling energy distribution. The spectra generated are used directly for chemical sensing in liquid and gas phase samples and indirectly for fluorescing biochemicals in liquid samples. These microdischarges can be driven by small battery-operated systems, and operated in ambient air at atmospheric pressure.

For electrode separations >200μm the two-electrode discharge takes the form of a pulsed arc, providing broadband optical emission and select peaks (lines) from chemical species present in the glow. The separate temporal characteristics of the line and background spectra present opportunities to improve detection. This concept is evaluated by isopropyl alcohol vapors (100ppm without preconcentration) using emission from CN fragments.

For electrode gaps of <75μm, the discharge characteristics are intermediate between arc and glow discharges. These hybrid discharges can be tuned by a ballast resistor and the applied voltage, to have the required glow or arc like characteristics. They have low broadband emission, last longer, and consume less power than the pulsed arc discharges. It is shown that they can detect 17ppm of acetone without pre-concentration in air ambient.

The energy of the microdischarges can be controlled by using a three-electrode (flashFET) scheme, which uses separate electrodes for initiation and powering of the discharge. In particular, a strategically located high impedance gate electrode that permits the use of pulses <100V between the source and drain. It consumes 22.5μJ/discharge in contrast to 470 μJ/discharge for two-electrode discharges. The lower discharge reduces cathode erosion.

Microdischarges employing doped liquid cathodes are used as tunable optical sources for fluorescence of biochemicals in microfluidic systems. A stacked microchip that integrates a microfluidic wavelength-tunable optical source, a biochemical sample reservoir and optical filters is used to realize the system. For DNA fluorescence, a barium chloride solution is used to emit light at 454 and 493nm. For tryptophan fluorescence, the cathode contains lead (II) nitrate solution to provide a 280nm emission.

A liquid discharge microchip, which uses a wetted porous cathode, is developed for analysis of water samples. It has an electrode gap of 50μm, an active area of $1 \times 1 mm^2$ and can detect 2ppm of aqueous Cr. Finally, a handheld system for chemical sensing based on this technology is developed. The system employs a customized sensor chip module (which can accommodate swappable gas and liquid discharge chips) and battery-operated circuit, along with a commercially available portable spectrometer coupled to a PDA for generating the microdischarge and performing the analysis.

Together these results address many of the key challenges in realizing discharge based chemical sensors and demonstrate their feasibility in handheld systems operating in ambient air.

Chapter 1 Introduction

This report concerns the scaling down of electric discharges – in particular discharges between planar electrodes – in size and their application to chemical sensing. The resulting discharges are different from macroscale discharges in important ways and are referred to as microdischarges. At atmospheric pressure, the discharge generally takes the form of a cold cathode glow discharge (referred to as microplasma) or an arc discharge. Emission spectroscopy from these microdischarges is used to analyze the chemical species present in the plasma. All the microdischarges studied in this report operate in air ambient at atmospheric pressure, unless otherwise mentioned.

A condensed qualitative review of gas discharge physics and is presented in section 1.1. Section 1.2 describes prior research in microdischarges. Section 1.3 describes the various chemical sensor technologies and the application of microdischarges in analytical chemistry. Section 1.4 provides a condensed review of micro-optical devices for fluorescence detection of biomolecules.

1.1 Breakdown of Gases in Electric Fields

Electric breakdown is the process of conversion of a non-conducting material (typically a gas) into a conductor by the application of a high enough electromagnetic

field. Generally, ionization reaches such a value that flashes of light from atomic transitions of the ions and neutrals can be seen.

Figure 1.1 illustrates voltage-current (*V-I*) characteristics of the discharge. The external circuit is represented by the load line. The ordinate E represents the applied emf and the slope of the line represents the resistance of the external circuit. The operating point is determined by the intersection of the load line and the discharge *V-I* curve.

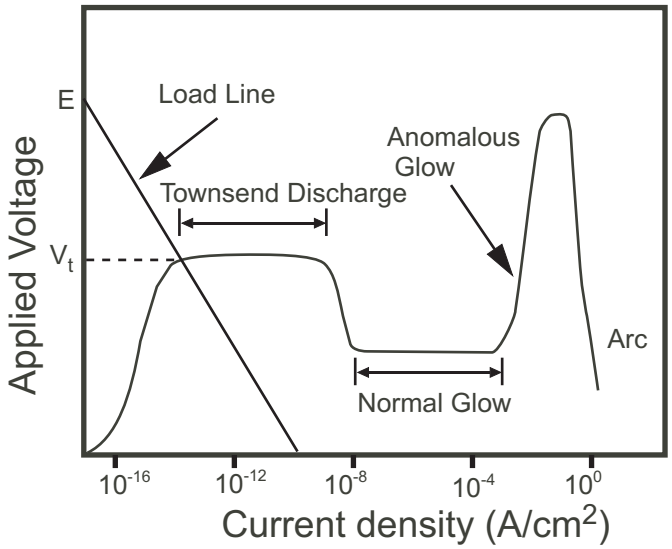

Fig. 1.1: Four different regimes of a plasma discharge-Townsend, normal glow, anomalous glow, and arc regions.

When the voltages are low (below V_t), there is still some current (~ 10^{-15} A), due to the presence of cosmic rays and natural radioactivity. If the gas is intentionally radiated with X-rays, a current of the up to few μAmperes can result, but this is still not enough to result in emission of light.

As the voltage is increased, the non-self sustaining current increases, as the charges are swept to the electrodes before recombination can occur. Finally saturation occurs, being limited by the rate of ionization. If the voltage is increased further, "*field*

intensified ionization" is observed. Such discharges are used in photoelectric cells and radiation counters. In such a discharge, the initial photoelectron gains energy in the electric field and creates more electrons and positive ions by impact ionization, so the initial current is amplified as a result of the avalanche multiplication. However, the electric current can survive only in the presence of an external source of ionization, and the discharge is said to be a *non-self sustaining*.

At still higher voltages, the positive ions created in the discharge gain enough energy to cause ionization. Since the mean free path of the positive ions is small (due to large mass), most of this ionization is in the form of secondary emission from the cathode (the work function of metals is usually much lower than the ionization potential of a gas). This effect is especially relevant in photodetectors where the cathode has low work function. However, in this regime, the secondary emission is quite low, and an external source is required to sustain the discharge.

If the external field is large enough (greater than V_t), a *self-sustained discharge* is created, which lasts as long as the field is applied. This kind of a discharge does not require of an external ionizing source to be present. If the resistance of the external circuit is high, the ionization and currents are small and no glow is seen. This kind of a discharge is called a *Townsend discharge* [Fri04][Rai97]. In such a discharge, there is uniform field in the gap as the space charge is not large enough to distort the fields.

If the current is gradually increased, either by increasing the applied voltage E, or lowering the resistance of the external circuit, a point is reached where the voltage across the electrodes begins to decrease with increasing current. After a certain point the fall stops and the current density remains constant. This is the glow discharge region. In

practice the discharge does not go through all the discharge regimes. When a voltage greater than the glow discharge threshold is applied (with the appropriate resistor), a glow discharge is formed. The high level of ionization results in an inhomogenous electric field concentrated over the cathode, and the discharge can be sustained at a lower applied voltage. Electrons are accelerated in the high field region and cause impact ionization of the gas. The positive ions thus formed bombard the cathode and cause secondary emission of electrons. In this way a constant source of electrons is created, which are accelerated in the field, and create more electrons and ions by impact ionization, which in turn create more electrons, and so on until an appreciable level of ionization is reached (typically an ionization of above 10^{-8} ions/atoms [Rai97]). The discharge is accompanied by a bright glow from optical emission from atoms and ions excited to higher energy state by collisions with energetic electrons. Photoemission from these photons arriving on the cathode is another source of secondary electrons, especially for low work function electrodes. The glow discharge is non-equilibrium plasma with the electron temperature much higher than the ion temperature. The cathode temperature does not change much, so the glow discharge is also known as a cold-cathode discharge.

Glow discharges are classified as normal or abnormal discharges. The normal discharge has a remarkable property -- that the current density at the cathode is constant. When the power to the discharge is varied, only the area over which the glow is seen varies, while the current density is constant. After the entire cathode is enveloped with the cathode glow, only then does the current density increase. This is known as the anomalous glow discharge and is accompanied by increase in the voltage required to sustain the discharge at that level. As the current density increases, it is accompanied by

a decrease in cathode drop thickness, leading to a higher electric field in the cathode drop region. The increased applied voltage manifests as large voltage drop across the cathode sheath, and as a result the energy given to the positive ions increases. The increased energy of the incoming positive ions raises the temperature of the cathode (assuming the cathode is not cooled) causing increased thermionic emission. A positive feedback can set in and the discharge can lead to the formation of an arc.

If the current is increased further an arc discharge results. Arc discharges are characterized by high currents and low voltages, as the source of electrons is thermionic emission and thermionic-field emission from this heated cathode. An arc, in contrast to a glow discharge, can be an equilibrium plasma with ions, electrons and atoms in thermal equilibrium. Arc discharges usually begin as glow discharges, which degenerate into arc discharges as a result of thermal instabilities. When the voltage is switched on, the circuit has a certain resistance. If the applied voltage is greater than the ignition potential V_t, a discharge mode immediately sets in, characterized by the intersection of the *V-I* curve and the load line.

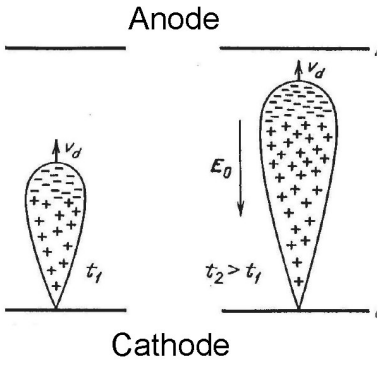

Fig. 1.2: Development of a spark discharge, showing the progression of an avalanche trail (from [Rai97].) The multiplication of electrons by impact ionization follows an exponential relationship, so for large discharge gaps a single avalanche trail can lead to a large level of ionization. The relatively slow positive ions form an advancing and conducting spark channel.

Spark and corona discharges are another form of discharges in which, the breakdown occurs in the form of a streamer. This mechanism is fundamentally different from the "Townsend mechanism" which characterizes arcs and glow discharges. Spark discharges occur when the discharge gap is large (typically > 5 cm at 1 atm.), and consist of a single transient avalanche trail instead of a steady state kind of discharge (see Fig. 1.2). In an electron avalanche, the number of electrons and ions increase exponentially with distance. If the discharge gap is large, a single avalanche can result in an appreciable level of ionization. Consequently, the path of a single avalanche can create an advancing "spark channel", which glows brightly due to the large number of highly energetic electrons. When the avalanche reaches the anode, a spark channel full of positive ions is left behind (the spark is a transient discharge, and the positive ions are assumed to be stationary for the duration of the avalanche). Additional avalanches are initiated near the spark channel from photoemission from the initial avalanche. The electrons from these are pulled into the positive ion filled spark channel. Since there is no source of electrons to sustain it, the spark discharge is a transient discharge. Lightening is a typical example of such a discharge. These discharges require large over-voltages and large discharge gaps, so are not amenable to miniaturization.

A corona discharge occurs in highly non-uniform fields around sharp conductors. Breakdown occurs even if the electrodes are far apart and the voltage between the anode and cathode is less than the ionization potential of the gas (hence it is one of the major loss mechanisms in high voltage conductors). In these discharges the local electric field near a high voltage conductor is much larger than the breakdown field strength of the gas. The region around the electrodes may be divided into a high field region, where the local

electric field is greater than the breakdown field, and a low field region. A corona discharge thus appears as a glow around the high voltage electrode. In a negative corona the sharp electrode is made the cathode, and the discharge is seen as a homogenous glow around the cathode. In this case the discharge is very much like a Townsend discharge characterized by avalanche multiplication in the high-field region, with secondary emission from positive ion bombardment and field emission from the cathode surface furnishing a constant stream of electrons. The current in the low field region is space charge limited, so coronas are high field, low current discharges. In a positive corona, the cathode does not contribute any electrons (as it is in the low field region), and the discharge has the appearance of luminous filaments around the high field region, which are thought to be streamers. The discharge is sustained by avalanche multiplication in the high field region, with secondary photoionization in gas supplying the seed electrons. (As the discharge is sensitive to photoionization in the gas, it is used in Geiger counters, where the corona is biased slightly below threshold).

Sparks and coronas occur only when the electrode gaps are large. When the inter-electrode gap is small, the DC discharge is usually an arc or a glow discharge. For the study of microdischarges, only arc and glow discharge are investigated.

1.1.1 Glow Discharges

A conventional glow discharge consists of a pattern of dark and luminous regions (Fig. 1.3). Immediately near the cathode there is a region of dark space (*Aston dark space*). Electrons are ejected from the cathode with energies of <1 eV. This is not enough for exciting an atom, and hence the region is dark. The electron gains energy in the electric field near the cathode, and as the electron energy rises to sufficient levels to

excite atoms a *cathode glow* appears. When the electron energy rises to a level such that collision cross section for the excitation falls off, the electrons cease to excite atoms, and a *cathode dark space* is formed. This is the region where ionization (and avalanche multiplication) takes place and positive space charge builds up. The field near the cathode (from the cathode to the end of the cathode dark space) is quite high due to the space charge built up, and is the main driving force behind the glow discharge. At the end of the cathode layer, the electron flux gets fairly large, and electrons generated at the end of the region have moderate energies. This leads to the formation of an intense *negative glow* region. The excited electrons gradually lose their energy, giving rise to the *Faraday dark space*. The electric field gradually rises over the Faraday dark space until the positive column is reached. In the positive column, a diffuse glow is seen, which corresponds to diffuse, low temperature plasma.

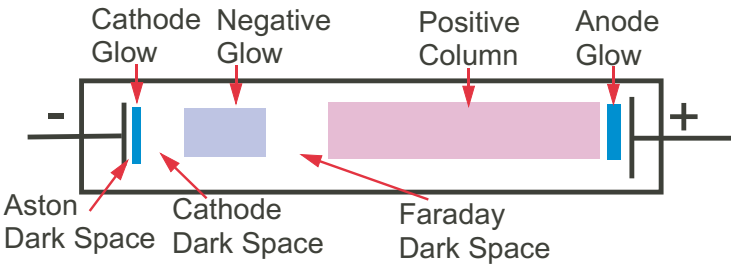

Fig 1.3: Structure of a conventional glow discharge

As the electrodes are brought closer together at constant pressure, the positive column is shortened, until it finally disappears. Then the Faraday dark space goes away and finally the negative glow also disappears when the discharge gap is lowered further. The effect of scaling on breakdown voltage is governed by the Paschen's curve, which shows a plot of breakdown voltage versus the product of pressure (p) and electrode spacing (d). The

breakdown voltage is a function of the *p.d* product and reaches a minimum value for a given value of *p.d*. The continuous curve shown in Fig. 1.4 illustrates this relationship.

In most glow discharges, the electric field is inhomogeneous and concentrated over the cathode. A minimum number of avalanche "generations" (40-60) is required for a self-sustained discharge, so there is a minimum value of *p.d*, which is optimal. If $p.L < (p.d)_{min}$ (where L is the electrode spacing) then the discharge extinguishes, and if $p.L >> (p.d)_{min}$ then the field is confined over the cathode layer, to compensate for the large gap giving a more optimal condition for breakdown [Rai97].

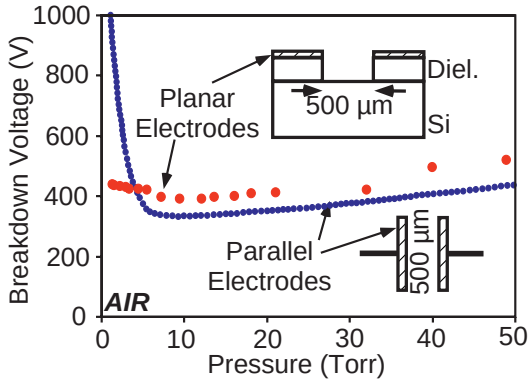

Fig. 1.4: Paschen voltage breakdown curve for parallel and planar electrodes with 500µm spacing (from [Wil04A]; reference Paschen curve from [Cob68])

1.1.2 Arc Discharge

An arc discharge is a self-sustaining discharge with a low cathode drop (of the order of the ionization potential of the gas ~ 10 eV). This is because high thermionic current is supplied by the hot cathode itself, so there is no need for considerable field amplification (like a glow discharges) for sustaining the discharge. Arcs are characterized by high current densities (10^2 -10^4 A/cm^2), which are necessary to heat the cathode to the high temperatures. When low boiling point metals are used (like copper, iron, silver) the arc is anchored on local hotspots on the cathode surface, which can reach

temperatures of 2000–4000 K. The electrode gets eroded rapidly so the arc is seen to shift rapidly. When refractory materials (like carbon or tungsten) are used, the arc is seen to be anchored at a fixed spot.

In high-pressure arcs (> 200 Torr), the electrons, ions, and atoms are in thermal equilibrium, so unlike glow discharges the gas in the arc is hot. Since the arc discharge is a dense equilibrium discharge with a high rate of ionizing and exciting collisions, it has a much more intense glow compared to a glow discharge.

Table 1.1: Summary of characteristics of various kinds of DC discharges (Current density data taken from [Rai97])

Type	***p.d* product**	**Field**	**Current Density**	**Temperature**
Non-self sustained Discharges	Low	$E \ll E_b$ (Breakdown Field)	10^{-16}–10^{-12} A/cm^2	Low
Townsend Discharge	Low	$E > E_b$	10^{-12}–10^{-8} A/cm^2	Low
Glow Discharge	Low	$E > E_b$ for initiation $E \sim E_b$ for sustain	10^{-18}–10^{-3} A/cm^2	Low
Arc Discharge	High	$E > E_b$ for initiation $E \ll E_b$ for sustain	10^{-3}–1 A/cm^2	High
Spark Discharge	High	$E >> E_b$	10^{3}–10^{4} A/cm^2	High
Corona Discharge	High	$E >> E_b$	10^{-6} A/cm^2	Low

1.2 Microdischarges

Recently, there have been many efforts in miniaturizing discharges, for use as sensors, optical sources or for micromanufacturing applications. Many of these are described in detail in a recent review paper [Kar04].

Manz and co-workers [Eij00] reported a DC plasma operating at atmosphere for the detection of organic vapors. The electrodes were spaced far apart, and the flow of air was restricted by a thin capillary, much smaller than the width of the electrodes. A gas flow of helium was used as the discharge medium. A 90 MΩ resistor was used to buffer the

discharge. Unlike [Wil04A], their microdischarge filled the whole tube, and the authors reported that the discharge was similar to a conventional glow discharge. The device had a continuous life of 4 hours and was able to detect 600 ppm of methane.

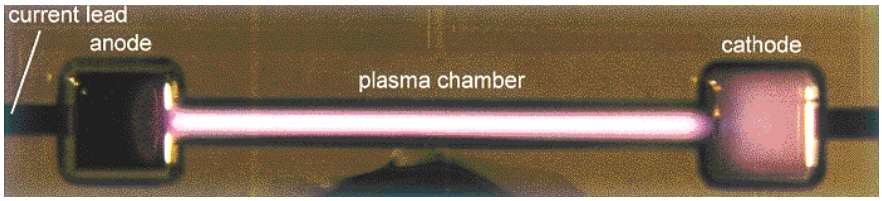

Fig. 1.5: Microplasma discharge in He reported by Eijkel and Manz [Eij 00]

Eden and coworkers [Ede02] miniaturized micro-hollow cathode discharges for use in display and chemical sensing applications. Hollow cathode discharges are DC discharges, which employ a hollow cylindrical cathode and an arbitrarily shaped anode. Hollow cathodes are similar to cold cathode discharges at low currents. However, at higher currents the space charge moves closer to the cathode and forms a virtual anode in the middle of the cathode cavity. The electric field thus develops a radial component. The electrons undergo oscillatory motion about the virtual anode (also called pendulum electrons), and thus can undergo large number of ionizing collisions. The hollow cathode effect is seen in microcavities for cavity diameters of the order of ~10μm. However, at atmospheric pressure, hollow cathode behavior is not seen. Micro-hollow cathodes operating at reduced pressures in inert ambient have been shown to be excellent light sources [Ede03].

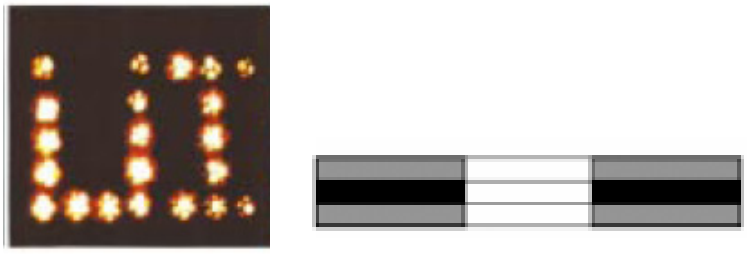

Fig 1.6: Micro-hollow cathode discharge devices developed by Eden [Ede03]. Left: top view. Right: schematic. The two metal layers are separated by a dielectric. The discharge is formed in the small holes that are etched through the structure.

Niemax [Nie03] reported low-pressure dielectric barrier discharges and used diode laser atomic absorption spectrometry for the detection of halogens in air. In a dielectric barrier discharge, power is coupled through a dielectric, electrode wear and contamination from electrodes is not an issue. In each half cycle of the voltage exceeds that required for breakdown, and narrow filaments are seen in the air gap. When voltage goes below threshold, the resulting charge is trapped in the dielectric. The current is arrested by the dielectric and the discharge does not become a glow discharge. Their device was able to detect 400 parts per trillion (ppt) of CCl_2F_2 in helium while consuming 0.5-1 W power. However, the use of absorption spectrometry necessitated low operating pressures and helium ambient. In this work a very long (1mm) region was required as absorption spectrometry was used. The long plasma region required contributed to the large amount of power consumed.

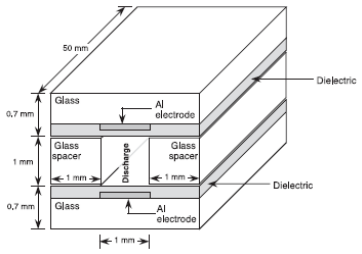

Fig. 1.7: Dielectric barrier discharge device miniaturized by Niemax [Nie03].

Yoshiki [Yos01] developed a parallel plate atmospheric pressure capacitive coupled microplasma in a quartz microchannel. The device was able to operate at atmospheric pressure but required helium ambient, and consumed 1-5 W power. Capacitively coupled RF discharges however have low level of ionization and are difficult to confine, as there is no average field in the plasma and electrons diffuse out of the glow region. They also require bulky RF generators, which are difficult to miniaturize.

Broekaert [Bro02] reported microwave-induced microplasmas which operated at atmospheric pressures. These consumed 10-40 W power, and operated in argon ambient. Hopwood [Hop05] developed a microwave split ring resonator plasma source that could operate in air. It consumed <3 W power and could operate at atmospheric pressure continuously for 24 hours without significant damage. Hopwood also developed miniaturized ICP (mICP) plasma for the detection of sulfur dioxide which had detection limits parts per billon (ppb) range [Hop00]. The device operated at low pressures (3-10 Torr) in an argon environment and used an extremely sensitive photodetector array for spectroscopic analysis.

1.3 Chemical Sensing Using Emission Spectroscopy from Discharges

In today's world of global terrorism and environmental pollution, there is increasing need for point-of-use chemical analysis. Conventional devices like chromatographs and mass-spectrometers must be complemented by fast, efficient, flexible, and portable devices. Many different kinds of miniaturized chemical sensors have been developed over the years for this purpose [Wil01]. Most of these belong to the category of thin film sensors. In these sensors, the target molecule is adsorbed on the surface of a thin film and causes some property of the thin film to change. The thin film is typically a conducting

polymer, a ceramic (like tin-oxide) or an esoteric material like a gold-thoilate nanoparticle clusters. In these devices selectivity and sensitivity is achieved by tailoring the thin film to trap a particular gas. Arrays can detect at most 5-10 compounds (Fig. 1.8), so the number of chemicals a sensor module can detect is limited. The speed of detection is limited by the kinetics of the adsorption process, and is typically a few seconds.

One of the most sensitive sensors are surface acoustic wave (SAW) sensors, which measure the change in delay or resonant frequency of a surface acoustic wave launched on the surface of a piezoelectric material like quartz[Fry99]. Chemical sensors based on thin films deposited on silicon micromachined resonators have also been developed and show similar characteristics [Bal00]. Chemiresistor sensors measure the change in resistance of a thin film, and can have limit of detection from ranging from ppb's [Zel04] to few hundred ppm [Dav04] depending on the coating. ChemFETs measure the change in work function of a thin film of metal or polymer as a function of adsorbed vapor [Jan97]. Most of the sensors described above can also be used in aqueous environments. In addition to thin film sensors, devices which measure changes in electrochemical properties of the solution, like ISFET's [Jan03], potentiometric [Bro03] and ampereometric [Bro05] sensors have also been developed. These sensors show very low detection limits (in the ppb range) but show large variation, as it is difficult to construct miniature reference electrodes.

Most of these sensors have cross-sensitivities to many different chemicals; so false positives pose a major challenge. Two different approaches have been taken to solve this problem. In one approach an array of sensors (having different coatings) is employed, instead of single sensor. It is assumed that although the sensors themselves are non-

specific, the overall signature is specific [Gar99]. This solution is limited, as it is difficult to make fabricate large arrays inexpensively. Most of the deposited films show variation in property both in one sensor over time and from sensor to sensor. Thus each system has to be calibrated (and re-calibrated) with a large number of gases to train the neural network to recognize the odor characteristic. Such calibration can be time consuming and expensive, sometimes even costlier than the sensor itself.

In another approach, a micro-gas chromatography system (μGC) is employed to separate the mixture before detection [Lu05][Mas04]. In these systems the gases are separated based on their elution time. These have been very successful in the separation of complex mixtures, even those containing very low concentrations of organic vapors. However, since the separation in μGC systems does not provide unique chemical identification, a sensor is needed to perform accurate chemical recognition and eliminate false positives that are based exclusively upon elution time. In addition μGC systems are restricted to mostly organic vapors and leave a wide range of inorganic gases outside their scope.

In spectral sensors, the atom or molecule is identified by measuring some fundamental property like molecular weight, mobility or atomic energy level. This method is more generic as it depends on the structure rather than a chemical property of a chemical species. In macroscale systems, gas chromatography is often coupled with mass spectrometry as they detect chemical species based on their charge/mass ratio, which is unique for each chemical. These devices can analyze large number (100+) of molecules and atoms. Figure 1.8 shows a comparision of spectral sensors and thin film sensors.

Inductively coupled plasma with mass spectrometric (ICP-MS) detection or atomic emission spectroscopic detection (ICP-AES) is widely used for elemental analysis in analytical chemistry, both in standalone systems and as detector in high-end liquid and gas chromatography systems. In ICP-MS the plasma is used to ionize and break down the chemicals into fragments, which are then identified by their charge/mass ratio (which can be done in various ways). This system is considered the "gold standard" by chemists as it is extremely sensitive and all chemicals have a unique signature. An ICP-AES system uses optical emission spectroscopy from the plasma to identify the chemical species. All chemical species emit unique and characteristic radiation in the plasma glow, which makes this technique generic and specific at the same time.

Argon is generally used as the carrier gas, as it does not have a strong emission of its own in the region of interest (for hydrocarbons). Argon atoms are also able to efficiently excite spectra by resonance transfer of energy, so the excitation efficiency is higher. Atomic spectra is more complex, than mass spectra as there are many lines corresponding to each chemical species, and isolating on line requires careful analysis.

ICP-MS systems have sensitivities in the range of few ppt's, while ICP-AES have been known to have sensitivities in few hundred ppb's. Mass spectra are also easier to interpret, compared to optical spectra as each species has only one charge/mass ratio but many emission lines, especially if it is a molecular gas. Although mass spectroscopy is indeed superior, for many applications cost and complexity are more important than sensitivity, and ICP-AES is the preferred choice.

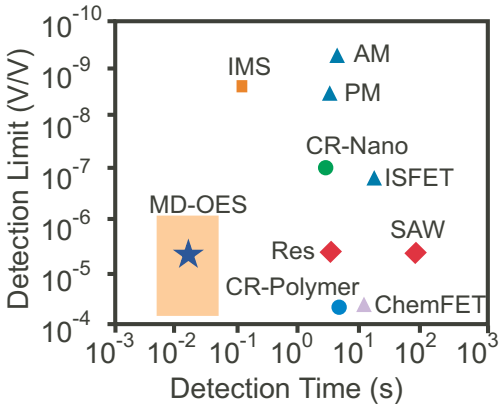

(a)

Symbol	Type	Ref
ChemFET	ChemFET	[Jan97]
Res	Silicon Cantilevers	[Bal00]
CR-Nano	Chemiresistors coated with Au-Thiolate nanoclusters	[Zel02]
CR-Polymer	Chemiresistors coated with polymer	[Dav05]
AM	Ampereometric Sensors	[Bro05]
PM	Potentiometric Sensors	[Bro03]
IMS	Ion Moblity spectrometer	[Milo1]
MD-OES	Microdischarge optical emission spectroscopy	This work

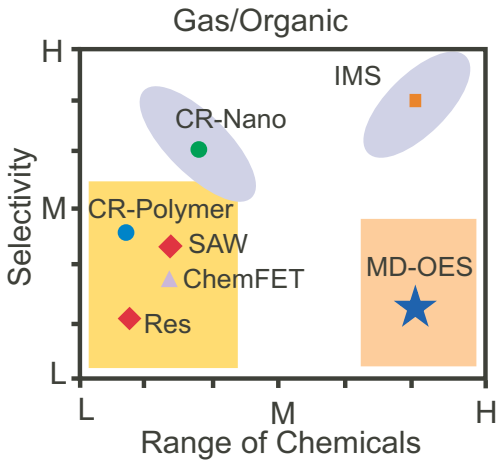

(b)

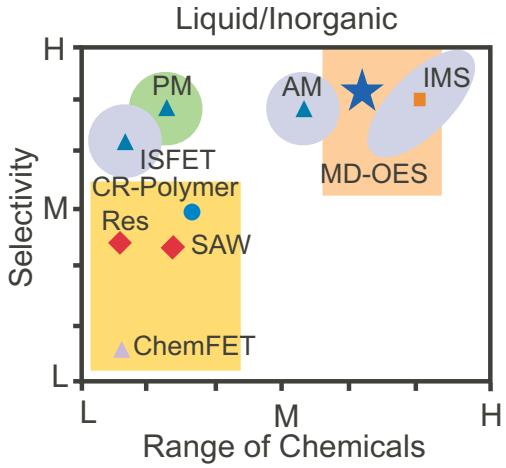

(c)

Fig. 1.8:(a) Plot of sensitivity v/s speed of detection for various kinds of chemical sensors (see table for the list of abbreviations and references). Each of the publications mentioned here represent the best results of the various classes of devices. (b) Plot of selectivity v/s the range of compounds for gases and organic compounds. L, M, H represent Low medium and high number of chemicals. In case of thin film sensors the range and selectivity is determined by the coating. In these cases complexity of the sensor readout circuitry and the fabrication process determines the number of different devices on the array. (c) Plot of selectivity vs range of compounds for sensing inorganic impurities in liquid.

There has been considerable effort in the area of MEMS-based mass spectrometry systems, but progress has been hampered because many of the phenomena do not scale favorably [Fre99]. They also require very high vacuum, which is difficult to achieve using microscale pumps. Miniature spectrometers based on quadrupole mass filters [Tay99] and ion mobility [Mil01] that can operate at atmospheric pressure have recently been reported. However, they use radioactive nickel as the ionization source, which limits their widespread application.

Optical emission spectroscopy from pulsed microdischarges is an attractive technology for chemical sensing with handheld devices. Microdischarges have high plasma density and an intense plasma glow. Since the discharge is confined to a small area, the power density is high, even at modest power levels. Figure 1.8 shows a comparison of the various chemical sensor technologies. Fig. 1.8b and Fig. 1.8c plot the selectivity versus the range of chemicals for different sensors. The labels L,M,H refer to low (1-5), medium (5-25), and large (25+) number of chemicals that can be detected by the sensor. Devices based on emission spectroscopy from microdischarges are much faster and can detect a large number of chemicals specifically without the added complexity of having multiple devices. It is the aim of this research to use these devices in handheld systems. Accordingly, all our devices are operated in an air ambient at atmosphere, so that a pump and tank of carrier gas is not required.

1.4 Microdischarges as Tunable optical sources for fluorescence

Fluorescence detection is a widely used technique in medical diagnostics and biochemical analysis. Many "fluorescent molecules" emit light with characteristic wavelengths when illuminated by certain excitation wavelengths, which are shorter (and

hence more energetic). In one diagnostic approach, a fluorescent dye is used to chemically label the analyte of interest. For DNA detection, dyes which intercalate into the double-helix provide very high sensitivity and make it possible to detect even attomoles of DNA base-pairs [zhu94]. A major reason for the high sensitivity is quantum efficiency, which is the ratio of the number of photons emitted to those absorbed in the excitation wavelengths. For example, SYBR Green I gel stain is a cyanine dye that has a quantum efficiency of 0.8 [Hau96]. When bound to dsDNA it is most efficiently excited by radiation over 491-503 nm, and has a broad emission spectrum over 510-600 nm, with a peak at 522 nm. In addition to DNA, fluorescence detection using dyes can be used to ascertain the concentration of many other compounds (like glucose, ATP, RNA, proteins, oxygen, carbon dioxide) in the cellular microenvironment.

The intrinsic fluorescence of proteins and peptides is of interest in many studies. For example, tryptophan, tyrosine or phenylalanine, which are fluorescent amino acids, and have been widely studied as tools for biochemical diagnostics. These three have absorption peaks over 250-290 nm and emission peaks over 280-350 nm, all in the deep ultra-violet (UV) region. This is also typical of other intrinsic fluorophores found in cells. The quantum efficiency of intrinsic fluorescence is relatively low. For example, tryptophan, which has the highest quantum efficiency among amino acids, has a quantum efficiency of only 0.19 when dissolved in water as a free amino acid [Lad00]. So to observe direct fluorescence in microsystems that employ these, not only do the sources need to emit in deep-UV region of the spectrum but also provide sufficient optical power, have a small footprint to be easily integratable with microsystems.

In the recent past tremendous progress has been made in microfluidics and micro total-analysis systems. These systems, however, still rely on relatively large external light sources for fluorescence detection, due to lack of good miniature light sources. Alternatives to optical detection, based on change in ion-concentration, impedance or mechanical properties have been implemented because of the problems with optical sources. Although these are very good for certain applications like monitoring pH, they lack the specificity of fluorescence techniques, do not provide spatial information and are restricted to a few chemical species only.

With respect to fluorescence detectors, the efforts have focused on solid-state sources such as light-emitting diodes (LEDs) and lasers (VCSELs) [Cho99] [Web01] [Thr02] [Fig04] [Kat04]. However, these do not have strong emission in the blue and UV region where most of the fluorescent chemicals have their excitation spectrum. There has been some success in using AlGaN heterojunction LEDs for deep UV light [Fis04][Kat04]. Although they emit in UV region, the emission lies in a very narrow region of the spectrum and it is difficult to tune its wavelength to different fluorescent molecules. In addition, these can only be made on sapphire substrates and require sophisticated fabrication processes and equipment, and hence, are not disposable. Further, integrating them with low-cost microfluidic systems can be a significant challenge.

One of the appealing features of microfabricated discharge devices is that they have promising emission characteristics in the UV region, and can easily and inexpensively be integrated with microfluidic systems. Spectroscopy on microdischarges can be used to sense trace amounts of inorganic impurities in aqueous samples [Que05]. In such devices, the microdischarge sputters the ions from the surface of the liquid cathode into its glow

region. Atomic transitions from excited ions and atoms in the microdischarge lead to emission of characteristic spectra. In this work, the microdischarge is used as a tunable optical source by using a liquid solution of predetermined composition targeted to generate specific wavelengths. The microdischarge is driven by a custom built circuit which is powered by a 3 V battery, and is suitable for portable applications.

1.5 Organization of the Thesis

This thesis encompasses the following areas: (1) Investigation of microplasma phenomena; (2) Use of pulsed arcs at atmospheric pressure for chemical sensing and use of time resolved spectroscopy for background suppression; (3) Investigation and characterization of arc-glow hybrids at atmospheric pressure and their use as chemical sensors; (4) The use of three electrode discharges for delivering a small quantity of energy into the discharge; (5) liquid cathode microdischarges for fluorescence of biomolecules; (6) a handheld system which incorporates both gas and liquid sensing devices for chemical sensing in air ambient.

Chapter 2 provides additional details of the physics behind microdischarges, and discusses some microdischarge models. Time resolved spectroscopy from pulsed arcs is covered in Chapter 3. Chapter 4 discusses the development of pulsed arc-glow microdischarges. Three-electrode powering schemes for reducing power consumption are explored in Chapter 5. Use of a liquid electrode discharge as a tunable optical source for detecting biomolecules is described in Chapter 6. Finally a handheld system is developed which can be used in the field. The details of the system and the devices are presented in chapter 7. Chapter 8 summarizes the work and suggests future directions of this research. Details of molecular and atomic spectroscopy are provided in Appendix 2.

Chapter 2 Theory and Modeling of DC Microdischarges

The application of high voltage DC is one of the simplest methods of initiating discharges. In conventional, macroscale plasma applications, DC discharges are infrequently used, since high frequency methods of initiating discharges – like RF discharges, microwave discharges, inductively coupled plasmas, and electron cyclotron plasmas permit the use of dielectric elements thus avoiding sputtering of electrode materials into the discharge. However, for use in handheld devices, DC (and pulsed DC) discharges are attractive because of system design considerations. This is because the high frequency power sources that are used these other discharges can be bulky and difficult to scale down in size, and they also impose tuning requirements. The shielding required for high-frequency power also adds to overall bulk of the system. Even though a few of these discharges themselves have been miniaturized [Kar04], they still operate from bulky non-portable power sources.

While DC glow and arc discharges have been studied for a hundred years, the understanding of the theory behind DC microdischarges poses a challenge. This is due to the fact that DC microdischarges do not follow conventional plasma statistics and involve the interplay of many complex processes, many of which are not in equilibrium. Even the simplest model which describes all the aspects of the microdischarge involves detailed Monte-Carlo simulations. In this chapter, fundamental plasma processes are

described, and these are then put together to qualitatively describe the microdischarge, and account for the various observations.

2.1 Microplasma Processes

2.1.1 Kinetic Theory

Miniaturizing DC plasmas requires a re-examination of many assumptions about classical DC plasmas. Certain plasma parameters are of particular concern or influence towards the miniaturizing of DC plasmas. The mean free path of the gas is one such fundamental limit. The distance over which electron-neutral collisions follow statistical mechanics is another benchmark, as Maxwellian distribution of electron energy is assumed for most glow discharge calculations. The mechanisms of plasma breakdown will have certain differences as the plasma column reduces in size, and the surface to volume ratio of the plasma increases. The Debye length is the dimension over which plasma is able to shield charge. Its role is critical in the formation and sustainment of electrically neutral plasmas. This section provides a review of these plasma parameters inherent in DC plasmas, which are relevant in our efforts.

2.1.1.1 Mean Free Path

The mean speed of a particle in a plasma is given by [Cha80]:

$$\bar{c} = \left(\frac{8kT}{\pi m} \right)^{1/2} \tag{2-1}$$

where $\bar{c}$ is the particle speed, m is the species mass, k is Boltzmann's constant, and T is the temperature. Therefore, a nitrogen atom at room temperature (which is close to the typical temperature in the plasma positive column) will be traveling around 515 m/s.

Implicit in the concept of a mean speed is a speed distribution function. Traditionally, for electron energy distribution in macroscopic plasmas, a Maxwell-Boltzmann distribution is assumed. This distribution is given by [Lie94]:

$$\frac{dn}{dc} = \frac{4n}{\pi^{1/2}}\left(\frac{m}{2kT}\right)^{3/2} c^2 \exp\left(-\frac{mc^2}{2kT}\right) \tag{2-2}$$

Here $\frac{dn}{dc}$ is the number *dn* of particles out of a total of *n* having speeds between *c* and *c* + *dc*.

Implicit in the assumption of a Maxwellian distribution of neutrals, ions, and electrons is a large number of interactions, and a state of thermal equilibrium. Also implicit is that driving forces from external fields do not play a considerable role in the velocity distribution of the particles. Specifically, any net drift velocity of particles will be much less than the average thermal velocity. These assumptions almost certainly do not hold for the case of microplasmas, for reasons discussed later.

The fundamental quantity that characterizes a collision is its cross section $\sigma(v_r)$ where v_r is the particle velocity. In the case of a hard sphere, the interaction cross section is given by [Cha80]:

$$\sigma(v_r) = \pi a_{12}^2 \tag{2-3}$$

Here a_{12} is the sum of the radii $a_1 + a_2$ of the impinging, and target particles, respectively. In the hard sphere model, the interaction cross section is independent of velocity. Real particles have velocity distribution, so the cross section is strongly dependent on the particle velocity, and the interacting species. Another quantity of interest is the mean free path for the impinging species [Cha80]:

$$\lambda = \frac{1}{n_g \sigma} \tag{2-4}$$

where n_g is the number of gas molecules per unit volume and σ is the cross-section for the collisions. The mean free path is the average distance traveled before collision For air at 1 atm. the calculated mean free path using the hard sphere model is close to 0.07 μm;

The collision frequency of particles is closely tied to the mean free path, and therefore, the gas density. It is given by [Cha80]:

$$\nu = n_g \sigma v \tag{2-5}$$

The collision frequency is an instrumental quantity in particle energy transfer. Collisional cross sections for electrons impinging on neutrals vary considerably with the energy of the electron. The various types of electron-neutral interactions are described in the following section

2.1.2 Collisions

Several types of particle collision occur in a discharge. Elastic scattering collisions are typically the most common, a routine scattering of an electron by a neutral, or neutral-neutral collision. All other collisions are inelastic. Inelastic collisions occur when not just kinetic energy is transferred, the main example being an ionizing collision. These collisions can result in a complete energy transfer from electron to molecule.

2.1.2.1 Elastic Collisions

When there is an elastic collision between two particles of masses m_i (an initially moving mass) and m_t (an initially stationary mass) at an angle θ to the line joining the centers, there is momentum and energy transfer. *By conservation of linear momentum:*

$$m_i v_i \cos\theta = m_i u_i + m_t u_t \tag{2-6}$$

where v_I is the initial velocity of m_i, u_i is the final velocity of m_I, and u_t is the final velocity of m_t.

By conservation of energy:

$$\frac{1}{2} m_i v_i^2 = \frac{1}{2} m_i (u_i^2 + v_i^2 \sin^2\theta) + \frac{1}{2} m_t u_t^2 \tag{2-7}$$

Solving for the two it is found that the fractional energy transfer (E_t/E_i) from mass m_I to mass m_t is given by:

$$\frac{E_t}{E_i} = \frac{4 m_i m_t}{(m_i + m_t)^2} \cos^2\theta \tag{2-8}$$

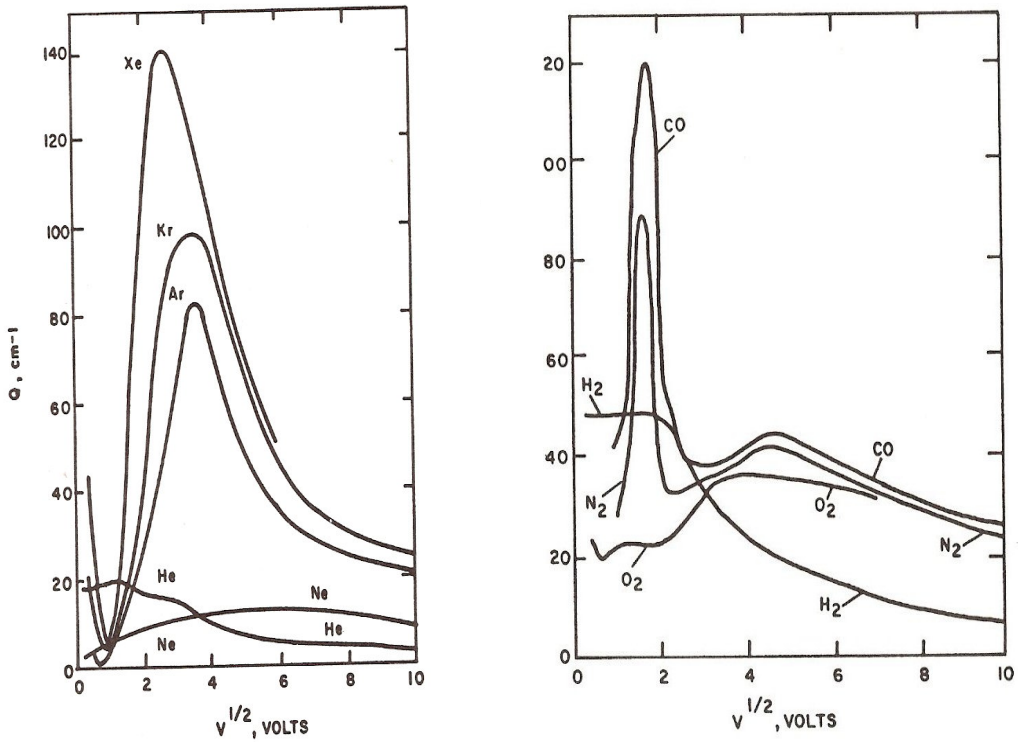

Fig. 2.1: Elastic collision cross section for some common gasses (a) Monoatomic (b) Diatomic (From [Bro59]).

The maximum energy transfer is when the cosine term is 1, corresponding to a head on collision. There is a large mass inequity between electrons and ions or molecules. An electron–N_2 elastic collision, for example, will only result in a 10^{-4} fractional energy transfer. Figure 2.1 shows the total effective cross-section Q, for rare gases and a number of simple monoatomic and diatomic molecules (from [Bro59]. It is noteworthy that the cross section is very low for electrons having energy greater than 20eV.

2.1.2.2 Inelastic Collision

In an inelastic collision, both the internal energy of the particles as well as their kinetic energy is changed. The inelastic collision can be an excitation, ionization, recombination, attachment, detachment or disassociation process.

A. Excitation

When an atom or molecule has absorbed sufficient energy for one of its electrons to pass to a higher energy level, the atom or molecule is said to be excited. The excitation process can occur be absorption of a photon through an electron or atom collision. For photoexcitation, the probability depends upon the selection rules governing the reverse process. Thus, a metastable state cannot be excited by this process. Further, the excitation only occurs if the energy of the photon and energy differential between the states is close (resonance excitation), and can lead to trapping of radiation in a discharge.

Excitation/relaxation collisions produce photons:

$$e + Ar \rightarrow e + Ar + h\nu$$

Excitation by electron impact can occur when the electron energy exceeds eV^*, the energy difference between the initial and final states of the atom/molecule. In an inelastic collision, the linear momentum and the angular momentum about the center of mass must

also be conserved. Thus the difference in angular momentum of the atom in its initial and final states must be balanced by change in angular momentum during collision. For electrons with energy equal to *eV**, the probability of excitation is small. The effective excitation cross-section, thus reaches a maximum at several times *eV** for singlet-singlet (which involve no change in angular momentum of the atom) transitions.

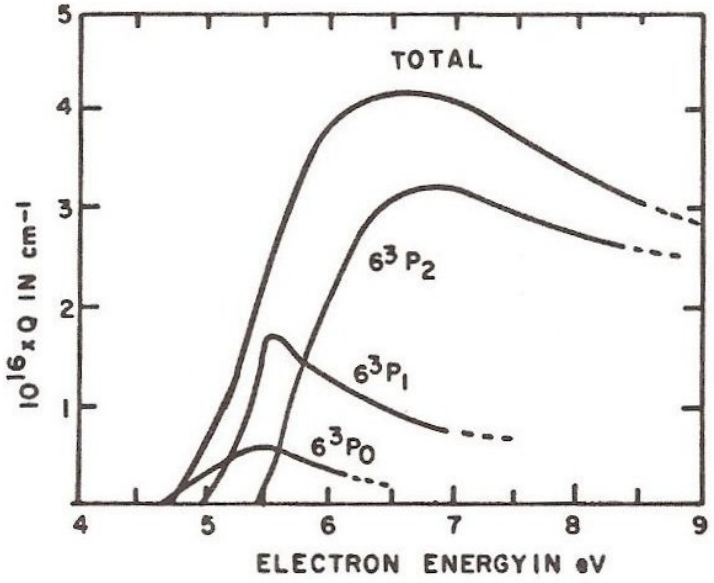

Fig. 2.2: Excitation cross section for excitation of mercury atom from initial state 7^3S_1 into $6^3P_{0,1,2}$ (The atomic term notation is N $^{2S+1}L_J$ where N is principal quantum number, S is spin, L is the orbital quantum number J is total angular momentum). States with same energy level, but different angular momentum have different excitation cross sections due to constraints imposed by momentum conservation requirements. From [Fra60].

For singlet-triplet transitions, the total spin quantum number changes from zero to 1, so one of the electrons must have its spin reversed. This can usually only occur, if one atomic electron is replaced by the impacting electron. The excitation curve thus has a maximum just over *eV**. After the maximum the curve decreases with (log E)/E) dependence for an allowed transition and 1/E for a forbidden transition. Figure 2.2 shows a typical curve for the cross-section of excitation by electron impact (from [Fra60]).

Excitation can also occur by ion or atom collisions. If the target particle (mass m_2) is assumed to be at rest and the incident particle has kinetic energy E_s the threshold energy for excitation is:

$$E_S = \frac{m_1 + m_2}{m_2} eV^* \tag{2-9}$$

B. Ionization

When an ion or atom has absorbed sufficient energy for an electron to escape to infinity, the atom or molecule is ionized. Ionization can occur by absorbtion of a photon, or through electron or ion impact.

For photoionization the photon energies lie in the UV and X-ray range of the spectrum. The cross section of photoionization rises sharply from zero at threshold, to a finite number as the photon energy is increased ($\sigma_p \sim 10^{-17}$ cm^2), and as the photon energy is increased, passes through successive steps as other electrons are ejected. At high energies, σ_p is very small.

The most important collision pertinent to sustaining a discharge is an ionizing collision, in which the primary electron removes an electron from the atom, for example:

$$e + Ar \rightarrow 2e + Ar^+$$

Ionization by electron impact occurs when energy of the impacting electron exceeds the ionization potential of an atom. The ionization cross section increases rapidly once the threshold conditions have been passed as momentum conservation conditions are easily satisfied due to the ejected electron. The liberated electron is accelerated by the electric field, creating more ionization, sustaining the discharge. Ionization by impact of another

atom or ion is similar and excitation, and the maximum effective cross section occur at kinetic energies in keV range.

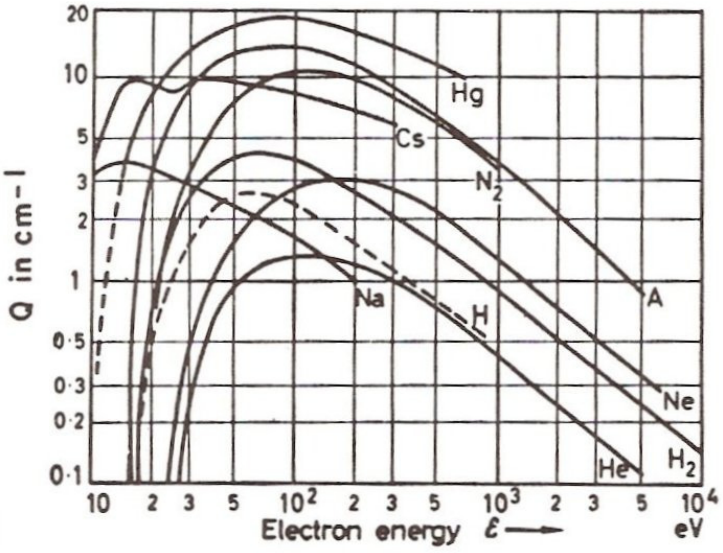

Fig.2.3: Ionization cross-section of uniform energy electrons in various gases (from [Eng65])

C. Penning Effect

Collisions of a second kind are those in which the excitation energy of one particle is transferred to another. This usually occurs only when the energy difference between the two species is small. The excess energy of the incident particle can appear as kinetic energy of the excited particle, or cause excitation or ionization of the target particle. When the collision is with a metastable state of one molecule with another ($eV_m > eV_i$) as in ionization of argon (V_i = 15.76 eV) by the metastable atom of neon Ne $^3P_2$ (V_m= 16.53 eV), the probability of ionization is very large (near unity per collision). This happens because the energy difference is small and the lifetime of the metastable state is large.

D. Disassociation

Dissociation reactions are electron impacts that break apart a molecule. There are three types of disassociation reactions: disassociation of a molecule into neutral species

(e.g., $e + O_2 \rightarrow e + 2O$), dissociative recombination($e + He_2^+ \rightarrow 2He$) and dissociative ionization ($e + CO \rightarrow e + C^+ + O^-$). The cross-section varies considerably. The cross section for dissociative ionization is of the order of 10^{-18} cm^2 and simple disassociation about 10^{-17} cm^2.

E. Charge Transfer

Charge transfer collisions generally take place between positive ions and neutral molecules. The charge transfer cross section depends upon the difference in ionization energy of the two colliding species. For a collision involving two particles of the same species (for example N_2 and N_2^+) , the charge transfer is close to gas kinetic cross section between two neutral molecules and is an order of magnitude larger than the ionization cross section by electron impact.

A charge transfer collision is given by:

$$A + B^+ \rightarrow A^+ + B$$

This collision will influence the energy distribution of etching species in the sheath of a plasma. An ion will begin to be accelerated through the sheath, will engage in a charge transfer with a neutral, and will retain its kinetic energy, becoming a fast neutral. The newly formed ion which was relatively stationary then starts to accelerate. Both neutrals and ions participate in etching of the substrate. The result is a few energetic ions become a larger quantity of less energetic etching species.

F. Electron Attachment

Collisions of electrons with certain atoms or molecules could result in their attachment forming a heavy negative ion. This reaction is common in electronegative

species like atomic hydrogen, oxygen, molecular oxygen, halogens, and large organic molecules, but uncommon in nitrogen and rare gases.

2.1.3 Electron interaction cross-section

For electrons interacting with nitrogen molecules, there are 4 principal types of collisions: elastic scattering, molecular excitation, atomic excitation, and ionizing collisions. All three of these interaction cross sections are a strong function of energy [Eng64]. The elastic collision cross section for nitrogen dominates of energies below 100 eV. The cross section varies from 2 x 10^{-16} cm^2 at energies in the range of 10^{-3} eV, to a singular peak of 2 x 10^{-15} cm^2 at energies in the range of 2 eV For energies from 2-50 eV, the energies stay within a factor of 3. For 5 Torr nitrogen, this corresponds to an elastic collision electron mean free path ranging from 57μm to 570μm. As microplasma dimensions range from 10's of microns to several mm, this will dramatically influence the electron distribution of microplasmas, making them highly non-Maxwellian. The excitation cross section for nitrogen becomes appreciable in the electron energy range of 2 x 10^{-1} eV for molecular excitations and 2 eV for atomic excitations. These cross sections have numerous peaks with a cross section on the order of from 2 x 10^{-17} cm^2. Ionization collisions start in the range of 18 eV, reaching the order of magnitude of the excitation peaks by 30 eV. An interaction cross section of 10^{-17} cm^2 corresponds to an excitation/ionization mean free path of 2.85 mm. This will provide one of the fundamental size limits on microplasma generation.

DC plasmas are formed by application of an electric field across a gas under vacuum. A charged particle in an electric field has work done on it. It will travel a distance *x* in time *t* given by:

$$x = \frac{1}{2} ft^2$$

f is the acceleration due to the electric field given by:

$$e\varepsilon = mf$$

Therefore, the work done on the charged particle by the electric field at time t will be given by:

$$W = \varepsilon ex = \frac{(\varepsilon et)^2}{2m}$$

Since $m_e << m_I$, electrons absorb much more energy from an applied electric field in time t than ions do. After some time, electrons collide with neutrals and ions, but as discussed earlier, energy transfer is very inefficient. The final result is that in equilibrium electrons have much higher kinetic energy – the typical electron energy in a plasma is 2-8 eV. Ions do not become much more energetic than the background neutrals, due to the poor energy absorption from the electric field. Neutrals will not gain much energy over room temperature. The only source of energy to neutrals is poor kinetic energy transfer from electrons. Neutral temperature will be around 1/40eV (room temperature), and ion temperature will be around 0.04 eV.

2.2 Plasma Models

2.2.1 Three Fluid Model

In the magneto-hydrodynamic model the plasma is assumed to comprise of three intermingled *nonviscous* fluids – electrons, ions and neutrals. The velocity of any one fluid is the average velocity characteristic of that fluid. The three fluids interact with

each other through electron-ion, electron-neutral and ion-neutral collisions. These collisions are modeled as frictional force in the momentum transfer equations.

2.2.1.1 Momentum Transfer Equations

The "force" on the electron fluid is comprised of three components: Pressure, Electromagnetic, and frictional force arising out of collisions. Consider a differential volume of electron fluid $d^3r=dx\,dy\,dz$. The total pressure force on the differential volume can be written as:

$$d\mathbf{F}_P = \left(-\nabla P_e\right)d^3r \tag{2-10}$$

The Electromagnetic force is given by the Lorentz equation

$$d\mathbf{F}_{el} = \left(-en_e d^3r\right)\left(\mathbf{E}+\mathbf{v}_e\times\mathbf{B}\right) \tag{2-11}$$

where $\mathbf{v_e}$ is the average velocity of electron fluid in d^3r.

The remaining force is the frictional damping force on the electron due to interactions with the ion-fluid and the neutral fluid (electron-electron interactions are ignored). The damping force is proportional to the velocity of the electron fluid and the density of the electrons. Thus

$$d\mathbf{F}_f = -(\alpha_{ie}n_i + \alpha_{ne}n_n)n_e\mathbf{v}_e d^3r \tag{2-12}$$

where n_i and n_n are the ion and neutral density respectively; α_{ie} and α_{ne} are the frictional coefficients for electron-ion and electron-neutral interactions. In general α_{ie} is a function of ion and electron velocity and α_{ne} is a function of electron and neutral velocity. By equating the sum of forces to mass of electron fluid to acceleration, we get the equation:

$$m_e n_e \frac{d\mathbf{v}_e}{dt} = -\nabla P_e - en_e\left(\mathbf{E}+\mathbf{v}_e\times\mathbf{B}\right) - \nu_{ce}m_e n_e\mathbf{v}_e \tag{2-13}$$

The quantity $[(\alpha_{ie} n_i + \alpha_{ne} n_n)/m_e]$ has the dimensions of time^{-1} and is defined as the *effective* collision frequency ν_{ce}.

The momentum transfer equations for ions and neutrals can similarly be written as:

$$m_i n_i \frac{d\mathbf{v}_i}{dt} = -\nabla P_i - Zen_i\left(\mathbf{E} + \mathbf{v}_i \times \mathbf{B}\right) - \nu_{ci} m_i n_i \mathbf{v}_i \qquad (2\text{-}14)$$

$$m_n n_n \frac{d\mathbf{v}_n}{dt} = -\nabla P_n - \nu_{cn} m_n n_n \mathbf{v}_n \qquad (2\text{-}15)$$

These three equations are coupled by their respective collision frequencies.

2.2.1.2 Continuity Equations and Equations of State

The flux of electrons coming in and out of a differential volume d^3r can be written as ***div*** $(n_e \mathbf{v_e})$. Equating this with the net change in density of electrons we get:

$$\nabla \cdot (n_e \mathbf{v}_e) + \partial n_e / \partial t = C_e \qquad (2\text{-}16)$$

$$\nabla \cdot (n_i \mathbf{v}_i) + \partial n_i / \partial t = C_+ \qquad (2\text{-}17)$$

and similarly

$$\nabla \cdot (n_n \mathbf{v}_n) + \partial n_n / \partial t = 0 \qquad (2\text{-}18)$$

C_e and C_+ are electron and ion generation rate respectively. They are generally not equal because there are a number of "fast electrons" which are not described by this model. Generally the electrons described in the model are the slow electrons which comprise the bulk of the electron fluid and have energy in the range 0.5 – 2 eV. The generation rates are obtained from models of these fast electrons. Further details are presented in [Sur90].Three additional equations are required to complete the model. These are the equations of state, and are specified by thermodynamic considerations. The equations of state can be written :

$$P_n = n_n k T_n \qquad (2\text{-}19)$$

$$P_i = n_i k T_i \tag{2-20}$$

$$P_e = n_e k T_e \tag{2-21}$$

The state equations for electrons are valid only in thermal equilibrium.

2.2.2 Boltzmann Equation

The two-fluid model is very useful in describing the behavior of plasma in an applied field, and its response to electromagnetic or optical perturbations. Nevertheless its usefulness is limited in analyzing more complex effects: like ionization and excitation of species, excitation of molecular oscillations and in analyzing the behavior of sheath plasma. For these detailed calculations an electron distribution function is required, which makes it possible to describe plasma processes in greater detail.

Each particle in the plasma is described by a point in six-dimensional phase space $f(\mathbf{r}, \mathbf{v}, t)$. The point in phase space describes the position and velocity of the particle. The plasma can thus be described by three distribution functions for ions, neutrals and electrons respectively. The Boltzmann equation describes the change in the number of particles in a unit volume in phase space. It can be written as:

$$\partial f_e/\partial t + \mathbf{u}_e \cdot \nabla f_e - \tfrac{e}{m}\left(\mathbf{E} + \mathbf{u}_e \times \mathbf{B}\right)\nabla_v f_e = \left(\partial f_e/\partial t\right)_{collision} \tag{2-22}$$

$$\partial f_i/\partial t + \mathbf{u}_i \cdot \nabla f_i - \tfrac{Ze}{m}\left(\mathbf{E} + \mathbf{u}_i \times \mathbf{B}\right)\nabla_v f_i = \left(\partial f_i/\partial t\right)_{collision} \tag{2-23}$$

$$\partial f_n/\partial t + \mathbf{u}_n \cdot \nabla f_n = \left(\partial f_n/\partial t\right)_{collision} \tag{2-24}$$

$\mathbf{u_e}$, $\mathbf{u_i}$, and $\mathbf{u_n}$ describe the instantaneous velocity (not average) of the particle in phase space. ∇_v represents the gradient in velocity space. The three Boltzmann equations are coupled through the collision term. The collision term is quite complex and consists of integrals over products of differential equations.

For weakly ionized plasma, electron-electron and electron-ion collisions can be ignored compared to electron-neutral collisions. The neutrals are considered to be at rest, as far as their interaction with electrons is concerned. This is a valid assumption since the electron velocity is much greater than neutral velocity. The collisions can be classified as elastic or inelastic.

$$\left(\partial f_e/\partial t\right)_{collision} = \left(\partial f_e/\partial t\right)_{elastic} + \left(\partial f_e/\partial t\right)_{inelastic} = I(f) + Q(f) \qquad (2\text{-}25)$$

Inelastic collisions contribute to the excitation of ions and electrons and creation of new electrons by ionization and annihilation process. They are important in determining the energy spectrum of the electrons, but being less frequent than elastic collisions have no influence on the field-electron interaction.

2.3 Microdischarge Models

Planar microdischarges are essentially negative glow discharges. The overall theory of such discharges is complex since the electrons are not in equilibrium and do not follow Maxwellian or other common distribution. A full description of the electron energy distribution function can only be obtained by Monte-Carlo simulations [Beo88]. An approximate 1-D analytic model [Raz89] provides a great deal of insight. In this model it is assumed that the electrons move along the field lines and are scattered either forward or backward.

The model only describes the energy of the "primary electrons"- which contribute to excitation and ionization process in the discharge. High energy "runaway electrons" are not described by this model. The negative glow discharges simulated with this model had an approximate electron temperature of 2-4 eV and a plasma density of $10^{11} – 10^{13}$ cm^{-2}

One of the problems with modeling microdischarges is that they lie in the intermediate range between collisional (where collisions dominate) and collisonless (where fields dominate) discharges, so only a monte-carlo model which takes into account all the processes can account fot the various observations. A 2-D Monte-Carlo model of microdischarges was developed by Kushner [Kus05]. It is well known that electrons in microdischarges do not obey Maxwell-Boltzmann or any other distributions, and so the best way to model these devices is to actually follow the path of a swarm of electrons in the given field conditions, and derive meaningful data from the resulting steady state. One may recall that a microdischarge has multiple path lengths and spatially varying non-uniform fields, so a 3-D model is what is necessary to get the complete picture. However, even a 2-D model gives valuable insights into the operation.

The model assumes that there are two types of electrons – bulk electrons and beam electrons. Beam electrons are those which are emitted from the cathode and accelerated in the sheath field. In the model electron-psuedoparticles are periodically launched from specified surface, with weightage proportional to the rate of secondary emission by ion or photon bombardment. By sampling the trajectories of the pseudo-particles, and electron energy distribution function (EED) of these beam electrons is obtained. These EED's are used as source functions for electron impact processes. Beam electrons, with energy less than a threshold (usually 4 eV) are grouped as a source function of bulk electrons.

The base case geometry is a cylindrically symmetric metal-dielectric-metal stack. Even though it is not a planar device, the geometry has the similar non-uniform fields and multiple path lengths, which are a feature of planar DC microdischarges. Peak electric fields near the cathode are extremely high (in excess of 80 kV/cm). The resulting bulk

electron temperature is 5.5 – 6.0 eV near the cathode and falling to 2-3 eV near the center of the channel. For argon plasma, the ion density is 2x 10^{13} cm^{-3} at 50 Torr and 1.8 x 10^{14} cm^{-3} at 625 Torr. It is seen that secondary emission, as a result of ion-bombardment of the cathode is the main source of initial electrons. For a *p.d* value of 7.5 Torr cm, the beam electrons cannot penetrate the gap completely, and hence most of the ionization is near the cathode. It is seen that although the device has a hollow-cathode like geometry, it does not show the hollow-cathode effect, and is similar to negative glow discharges. The extent of the glow is seen to be related to the range of beam electrons. So at higher pressure, the glow is more tightly confined near the electrodes.

2.4 Planar DC Microdischarges

DC Microdischarges operating at reduced pressures (for in-situ etching of silicon) were investigated in [Wil03A] and [Wil03B]. Unlike conventional plasmas, where the glow exists in the region between electrodes, the glow in DC microplasmas is confined to the proximity of the cathode. When planar microelectrodes are used, Paschen's curve is not applicable in the traditional sense: the breakdown voltage for fixed electrodes is relatively insensitive to pressure in the 1-20 Torr range, and remains at ~400V for ambient air (Fig. 2.4a). This is because with most microstructures, multiple path lengths are simultaneously available, which makes the discharge gap a variable, and this permits a low breakdown voltage to be sustained even as the pressure decreases below from the value that favors minimum electrode separation. Experiments done with split anodes show that although the breakdown voltage remains constant, the discharge current shows a spatial variation when pressure or power is varied.

Due to the proximity of the electrodes, the negative glow, the Faraday dark space and the positive column are not seen. Most of the voltage drop is across the space charge region around the cathode, and the glow is "glued on" to the cathode. The electrons emitted from the cathode are accelerated in this field, and as they reach energies large enough to excite atoms to higher energy states, a glow is seen. Unlike a conventional glow discharge, a separate dark region where ionization happens is not seen. In this respect the discharge is similar to a hollow cathode discharge, which also shows and intense cathode glow instead of alternating light and dark regions. A large number of "runaway electrons", which are electrons that have very high electron energies (~ 100 eV) are seen [Wil03B]. Their role in sustaining the discharge is not known.

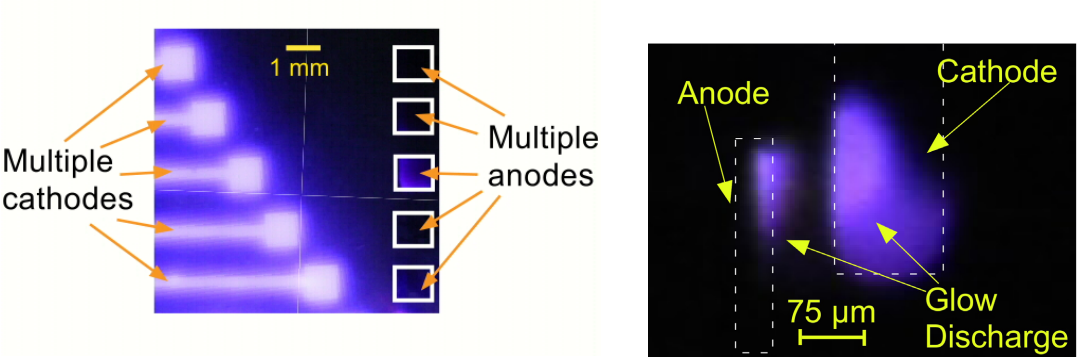

Fig.2.4: (a) Experiment illustrating plasma is confined over cathode region, confinement is a function of pressure and power density (from [Wil03A]). (b): Atmospheric pressure glow discharges (this work).

In the present work, the microdischarge devices, similar to those described above are used for chemical sensing. While Wilson's devices were DC devices operated at reduced pressures (1-30 Torr), these devices (Fig. 2.4b) are pulsed devices operated at atmospheric pressure for chemical sensing. These operating conditions introduce significant differences and new challenge. At high pressures, the discharge exhibits different characteristics. The discharge is no longer a simple glow but takes the form of

arc-glow hybrids. Heating of neutrals and ions is more prominent in high-pressures, and gas dynamics play an important part in the discharge characteristics. Power consumption at atmospheric pressure is typically higher than at low pressures, which is an important concern for battery operated systems. Hence new techniques have to be developed to make maximum use of the available energy. For small gaps (50-100 μm) the discharge is initiated as a spark discharge, which changes into a glow, an arc or an arc/glow hybrid which have characteristics intermediate between glow and arc discharges. For larger gaps, the discharge takes the form of a bright spark discharge. Further details are presented in Chapter 3 and Chapter 4.

Chapter 3 Time Resolved Spectroscopy on Pulsed Micro-Arcs

Pulsed arcs are attractive for chemical sensing applications as they are equilibrium high temperature discharges and have a very intense glow with spectral emission from UV to infrared. Pulsed micro-arcs have been used with aqueous electrodes for the detection of heavy metal impurities in water samples [Que05][Wil02], and tailored deep UV emissions for the fluorescent detection of biochemicals [Mit06][Mit03] (see Appendix). This chapter explores the use of atmospheric pulsed arcs for spectrochemical detection of organic vapors. In contrast to arcs reported in previous chapter, in these devices the electrodes were spaced far (300 – 1000 μm) apart.

In microdischarge gas sensors, a pulsed discharge is struck by the application of a high voltage pulse between two- or three-electrode microstructures. The organic vapors in the gas ambient are fractionated, and together with these fragments, they are excited to higher energy states. The excitation can arise either due to the energetics of their formation, or by collisional excitation with energetic electrons. As the excited species relax back toward equilibrium, the resulting spontaneous optical emission provides a chemical signature. (While ignition of organic vapors can be a concern, it has never been observed in our experiments, both in high and low levels of vapor concentration. This is probably due to low energy of the discharge, and the proximity of microstructures, which suppresses the temperature rise.)

Arcs usually produce temperatures on the order of 5000 K, which is high enough to excite the spectra of neutral atoms and molecules as well as many molecular lines [Cob41][Rai97]. For this reason, much of the classical work in spectroscopy was done using arc discharges. Arcs can be generated just by applying a high voltage across two electrodes, so complicated circuitry is not required, and the system is amenable to overall miniaturization. Single shot discharges are used to reduce the power consumption and increase lifetime of the device.

The emission from arc discharges consists of continuous background emission, and line spectra from atomic and molecular transitions. The reasons for continuum emission in nitrogen are difficult to model, and mathematically compensate the measured spectra. Hence, in spectrochemical analysis, the ratio of line intensity to background (relative sensitivity) is the limiting factor rather than the absolute line intensity (absolute sensitivity). Unlike absolute sensitivity, the relative sensitivity cannot be increased by traditional methods like amplification or filtering.

In this context, time resolved spectroscopy is explored as a possible method to improve relative sensitivity. The pulsed arcs are powered by short bursts of current (few μs) but the glow lasts for much longer [Mit04][Nil64]. By studying the time resolved spectra the knowledge of optimal sampling conditions can be obtained. The emission spectra during various phases of the discharge pulse are examined to determine how sensor performance can be enhanced. It is observed that characteristic line spectra are accompanied by continuum emission, which decays with a longer time constant. It is shown that the differences in their temporal characteristics can be used to enhance the line spectra by subtracting the continuum emission in real time. In this context, it is

worthwhile to note that while emission spectra are affected by potentially every background gas, for the purpose of portable chemical sensors; our primary interest is in emission lines that are representative of the target chemicals.

3.1 Device and System Design

The device shown in Fig. 3.1 utilizes two electrodes patterned on a glass substrate and spaced apart by nominally 200 μm, and up to 2 mm. In this manifestation of the device the electrodes are made from Ti to maintain consistency with past experiments [Wil03A]. The gas flows through the channel formed between the substrate and two glass spacers that are bonded to it forming a cap. The purpose of the cap is to prevent the accumulation of dust, which can otherwise degrade device performance, e.g., by surface leakage. Organic vapor molecules are broken down into smaller fragments as they pass through the microdischarge region [Bra68]. The emitted spectrum, which is characteristic of the fragments, is observed using a portable off-chip spectrometer (Ocean Optics USB2000).

The microdischarge is powered by a capacitor bank under computer control, which provides a current pulse of about 2 μs duration (Fig. 3.1a). Figure 3.2a shows idealized waveforms. A shunt switch, implemented as the MOSFET M1 (STPNB100 from ST Microelectronics) , is employed to avoid high currents in the series loop. The MOSFET is normally ON and drains the high voltage. Large resistors are used in the shunt path to keep power dissipation low.

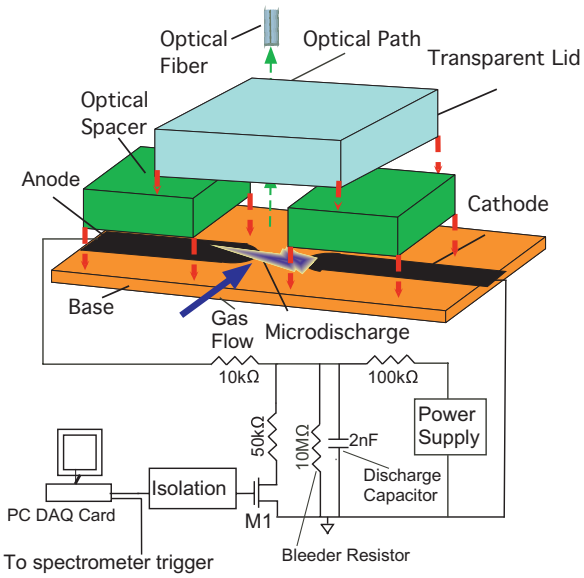

(a)

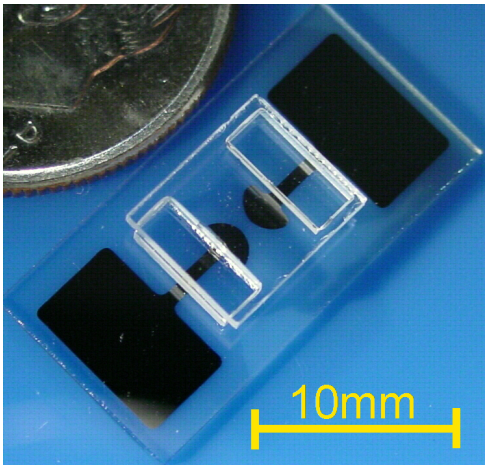

(b)

Fig. 3.1: (a) Schematic of the two-electrode sensor for afterglow spectroscopy, showing the gas flow and the optical path of the emitted light and the circuit configuration. A PC controlled shunt switch is employed since microdischarges are powered by short bursts of current making series switch inefficient. A spectrometer trigger is generated along with the μdischarge trigger for time resolved spectroscopy. (b) A picture of the test device shown against a US quarter.

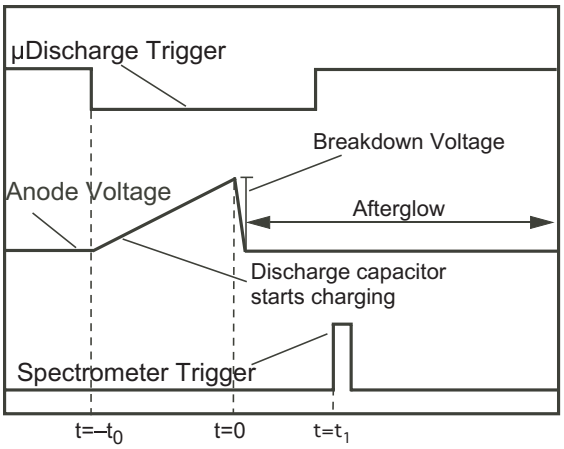

(a)

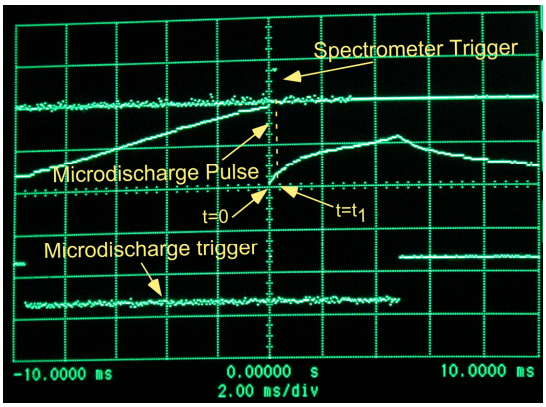

(b)

Fig. 3.2: (a) Sketch showing idealized waveforms for the two-electrode pulsed microdischarge. When the microdischarge trigger is turned on, the discharge capacitor is charged up, and when it reaches the breakdown voltage all the charge is dumped into the microdischarge. The glow period lasts for a very short time during which high-current flows. For capturing the time-resolved spectra, the spectrometer trigger is initiated at time t_1 after the discharge. (b) Captured waveform showing the discharge pulse and spectrometer trigger.

When a microdischarge is to be initiated, the microdischarge trigger signal goes low. The shunt switch turns off and the capacitor starts charging. Once the breakdown voltage is reached, the microdischarge occurs and the charge in the capacitor is drained by it in a few microseconds. This period corresponds to the primary glow period of the discharge.

(Note that a relatively long – 10 ms – charge-up time for the capacitor is deliberately used to avoid the possibility of a double discharge.) A spectrometer trigger that is generated after a programmable delay of time t_1 after the discharge turns the spectrometer on for 2.1 ms. (The minimum sampling window for the spectrometer is 2.1 ms.) By varying t_1, a time-resolved spectrum of the microdischarge can be obtained over a sequence of pulses. The trigger signals and the microdischarge signals are generated from a timer in the data acquisition card (Lab PC 1200 from National Instruments), to provide accurate jitter free operation.

In these devices, the breakdown characteristics did not vary within the small sequence of pulses used. The time required to charge up the discharge capacitor to the breakdown voltage was also repeatable enough to permit synchronization of the optical sampling to the discharge. Figure 3.2b shows the captured waveform with the discharge trigger, the anode waveform, and the spectrometer trigger. It is evident that the capacitor does begin to charge up again after the discharge pulse, but this does not lead to a double discharge as the charging is slow and the voltage is below threshold.

3.2 Measured Results

Figure 3.3a shows a baseline measurement of the two-electrode device in air for which the optical sampling duration encompasses the entire duration of the microdischarge. A long integration time (10 ms) with a spectrometer trigger at t_1= -1 ms was used to capture this spectrum. The spectrum is comprised of bands corresponding to emission from atmospheric gases, superimposed on a broadband background. The bands consist of several closely spaced lines (instead of single lines, as would exist atomic spectra) because the different energy levels in molecules have a fine structure

corresponding to many vibrational and rotational levels. An extensive system of bands of nitrogen is seen to dominate the spectral output. We identified bands from the NO γ–system, N_2^+ 1^- system, N_2 2^+, Balmer lines H_α and H_β from hydrogen [Pea62]. A reason for the broadband emission is not well understood, but is probably due to a combination of blackbody emission [Mor69], and recombination spectra from long lived metastable species of nitrogen. This makes it challenging to reliably calculate and predict these spectra, and theoretically assess their contribution to the measured data.

Further complexities arise from a number of sources. The large number of closely spaced rotational lines may not be adequately resolved by a modest spectrometer and may be manifest as continuum like emission. The high operating temperature and pressure of these plasmas potentially causes the closely spaced lines to broaden and overlap more. Doppler broadening, which is a result of random thermal motion of the emitting species, can increase dramatically at the elevated temperatures. Collision broadening, which is a result of interruption of light emission due to collisions, is also elevated in the high plasma density and elevated pressures that are found in the core of the arc. The combined impact of these complexities is to reduce the relative magnitude of targeted spectral peaks despite strong emission intensity from the discharge as a whole.

The temporal evolution of the spectrum is shown in Fig. 3.3b. The spectral emission was sampled in 2.1 ms long windows of time at varying delays from the electrical discharge. The dominant line spectra are seen to decay rapidly compared to the wider background. If the goal is to detect dominant peaks, then samples that are short in duration and taken with no delay provide a high ratio of signal-to-background spectral peak intensity when compared to longer samples (10 ms). The afterglow seems to

contribute more of the "noise" and less signal to the emission spectrum. However, some of the less dominant peaks that appear lost within the broadband radiation can also be identified with the assistance from more delayed spectra. The continuous broadband emission is systematic, and not random, its effects can be reduced by subtracting it from the overall spectra. Time resolved spectroscopy provides an advantage in this case, and the technique allows real time subtraction of the background without making it necessary to calculate or predict these spectra.

As shown in Fig. 3.3 b, the afterglow spectra for t=7 ms and later are predominantly continuous emission. The spectral emissions from t=7–9 ms and t=12–14 ms were subtracted from the t=0 spectrum in Fig. 3.3 b. (It is important to note that the spectra are not scaled before subtraction as that would multiply the random noise). Fig. 3.3c shows the resulting spectrum which has much more discernable peaks, particularly in the 500–600 nm and 650–750 nm ranges. This permits, for example, the clear identification of peaks for C_2 (Swan bands, 516.5 nm), which were otherwise not clear.

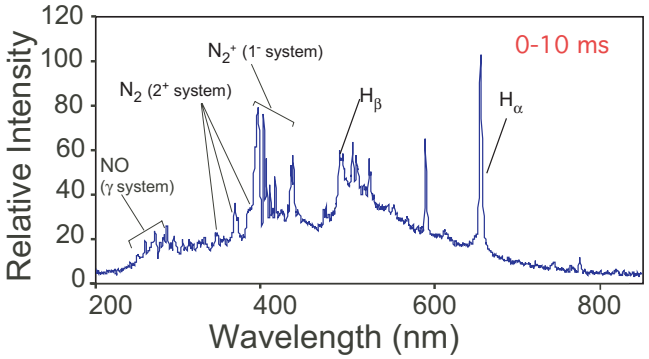

(a)

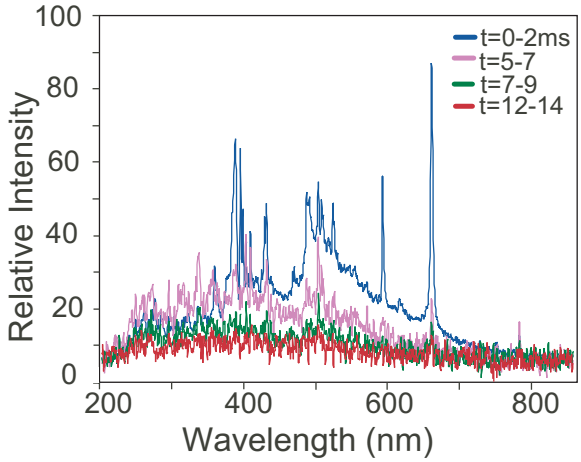

(b)

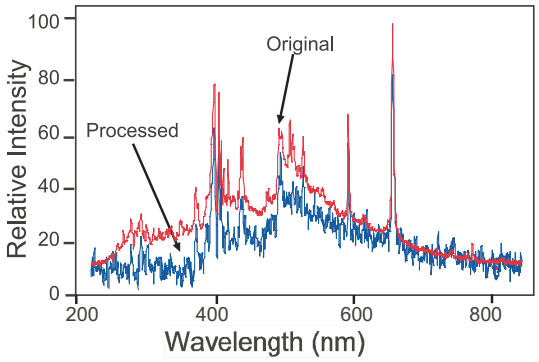

(c)

Fig. 3.3:(a) Spectrum of the micro-discharge in air. Line spectra corresponding to the nitrogen and water vapor are seen superposed on a continuous spectrum. (b) Time resolved spectra of air. The emitted light is sampled for 2.1 ms, at different points after a micro-discharge pulse. Although the intensity is on a relative scale, the readings are taken with the same setup, so a comparison of intensities can be made. (c) When the continuous emission is subtracted from the spectrum at t=0 the resolution of the lines is enhanced.

To evaluate the use of the device as an organic vapor sensor, it was placed in a chamber with a constant vapor concentration. A schematic of the setup is shown in Fig. 3.4. Before proceeding with the experiment, a vacuum pump was used to evacuate the test chamber to flush out vapors already present in the chamber. Vapor laden carrier gas (nitrogen) was flowed through and a dynamic equilibrium ensured that a constant vapor concentration was maintained inside the chamber. Changing the flow rate of the carrier gas through the bubbler (which contains the liquid) varied the vapor concentration. A commercial VOC sensor (MiniRAE 2000 from RAE Systems), was used to provide a benchmark measurement.

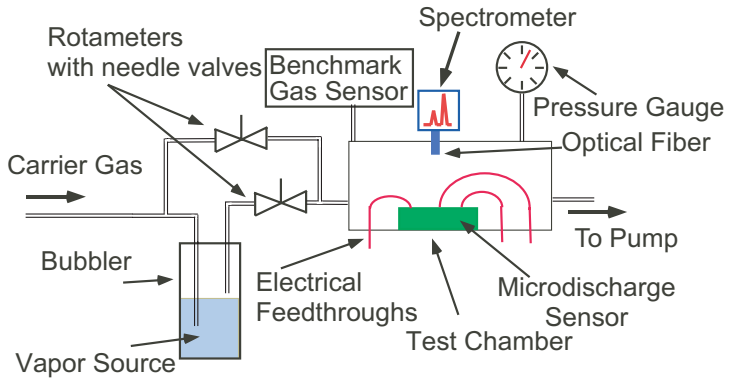

Fig. 3.4: Test set-up for sensor. Vapor concentration is varied by flow rate of carrier gas through a bubbler containing the compound of interest. A commercial vapor sensor (MiniRAE 2000 from RAE Systems) provides a benchmark measurement. The optical signal is observed through a fiber optic cable, connected to a palmtop spectrometer. For some experiments, a handheld spectrometer (USB 2000 from Ocean-Optics) is used instead of the spectrometer shown in the figure.

Figure 3.5a shows the spectrum in the presence of isopropyl alcohol (IPA) vapor, taken synchronously with the discharge and a sample time of 2.1 ms. Trace organic vapor detection has two problems: first, the presence of 300 ppm of atmospheric carbon-dioxide interferes with the spectral emission, and second, for positive identification of molecular

species, the whole band (and not just one line) must be identified. With the extensive emission from nitrogen in air, identifying weak bands due to organic vapors is a huge challenge. In this experiment, the IPA concentration was independently measured at 100 ppm. Band spectra corresponding to C_2 (516.5 nm) are very significantly stronger in the presence of IPA than in air alone, but the carbon dioxide that is naturally present in air provides a lower bound for the detection limit of such a device. It should be noted that the characteristic spectra from the carbon fragments that are generated, depends to some extent on the nature of the discharge. (For example, in section III.B we note that the three electrode arrangement, which supplies less energy to the discharge, permits molecular fragments such as CH and CN, that are not present in air, to be more readily distinguished from the background.) Figure 3.5b shows the CH line at 314 nm observed in a two-electrode discharge. At a concentration of 600 ppm, the emission can be clearly distinguished. It is apparent that without the use of a carrier gas or a preconcentrator, the limit of detection is ~100 ppm.

While the method of detecting fragments allows a large number of organic compounds to be detected, the present technique does not distinguish between two chemical species having the same base constituents and are also fractionated in an identical manner by the discharge [Kin00]. (This topic will be explored in our future efforts). However, in many cases non-hydrocarbon functional groups and organometallic compounds can be distinguished [Mar00]. The authors have also been able to distinguish different amino acids based on the relative intensities of nitrogen and hydrogen lines. Compound specific information may be obtained by examining larger fragments by the use of infrared spectroscopy.

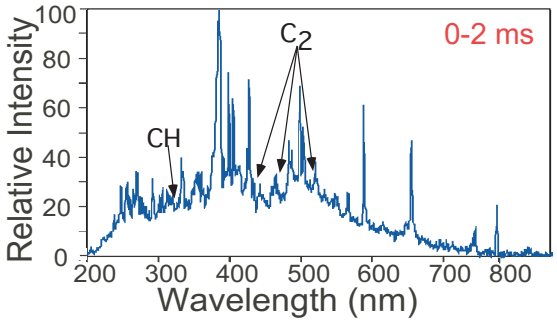

(a)

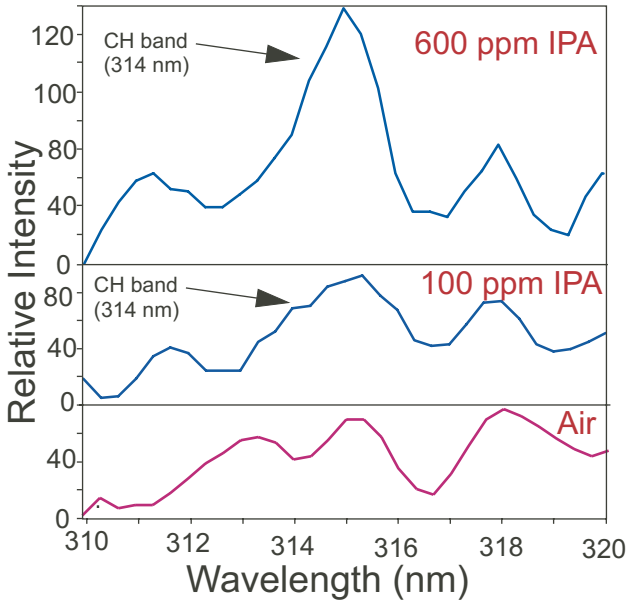

(b)

Fig. 3.5: (a) Spectra of the micro-discharge in air with 100 ppm IPA taken at t=0, and a sample time of 2.1 ms with a handheld spectrometer (USB 2000 from ocean optics). Spectra from various carbon fragments can be discerned

3.3 Conclusions

Emission spectroscopy from micro-arc discharges was used for chemical anslysis of organic vapors. It was found that the emission had a lot of background emission from

nitrogen and other gases in air, and wideband emission which made idenfitication of line spectra difficult.

The temporal characteristics of the spectra can be used to circumvent the problems caused by extensive emission from nitrogen, broadening of lines, and continuum emission. This provides an opportunity to sample species in an air ambient. In particular, it is shown that the broadband emission, which decays slowly, can be separately captured and subtracted from an early snapshot of the spectrum to enhance the resolution of some of the weaker lines. This approach is used to detect 100 ppm of IPA in air ambient.

Chapter 4 Micro Arcs, Glow Discharges and Hybrids

Chemical sensors based on microdischarges – both arcs and glow discharges – provide rapid and simultaneous detection of vapors by using their characteristic emission spectra in the plasma glow. Microglow discharges studied previously for in-situ deposition and etching applications [Wil04A] had a discharge gap of few hundred microns and existed only at reduced pressures (<30 Torr). At 1 atm. the microdischarge took the form of an arc, which is quite different. Unlike the microglow discharges which are driven by steady currents, micro-arc discharges have high transient current. These typically result in optical emission over a wide spectral range covering both UV and infrared portions of the spectrum. In contrast, microglow discharges have a narrow spectral distribution, usually concentrated in the UV-blue region, due to the strongly non-equilibrium nature of the discharge. Microglow discharges are also unstable at high pressures and degenerate into arcs if special measures like cooling are not employed. In an effort to generate microplasmas operating at atmosphere the scaling of discharge gap was explored. Research done previously, with low pressure planar microglow discharges had revealed that do not obey conventional scaling laws and the preferred breakdown path is a strong function of pressure and power levels. However, despite the fact that microplasmas do not strictly follow Paschen's curve (which governs scaling of conventional glow discharges), it is seen that at lower values of *p.d* glow discharges are

the preferred method of breakdown. Indeed it is seen that at electrode gaps of <75 μm, it is possible for microplasmas to exist even at atmospheric pressures. However the character of the discharge can vary from pure glow discharge, to a pure arc or hybrid micro-arc glow discharge, which shows characteristics of both. This chapter explores the nature and applications of these microdischarges.

4.1 Design and Fabrication

The device (Fig.4.1) consists of planar copper microelectrodes fabricated on a glass (Pyrex™ #7740) substrate. The anode-cathode gap spacing is 75 μm. The cathode is designed to have a large area (300 μm x 300 μm) as microdischarges are driven mainly by secondary emission from the cathode. Some designs had a tip at the anode to provide a consistent breakdown path for the arc. Devices without the tip at the anode (and same discharge gap) were also fabricated and showed identical results.

The control circuit used in this effort is also illustrated in Fig. 4.1. The microdischarge is created by discharging a capacitor that has been previously charged to a high voltage (450 V - 900 V). When the switch is turned on the capacitor starts charging and as soon as it reaches breakdown voltage, it discharges. A computer-controlled switch is used to control the time for which the discharge is on. A current limiting resistor is used in the ground return path to regulate the discharge. The form of the discharge depends strongly on the limiting resistor.

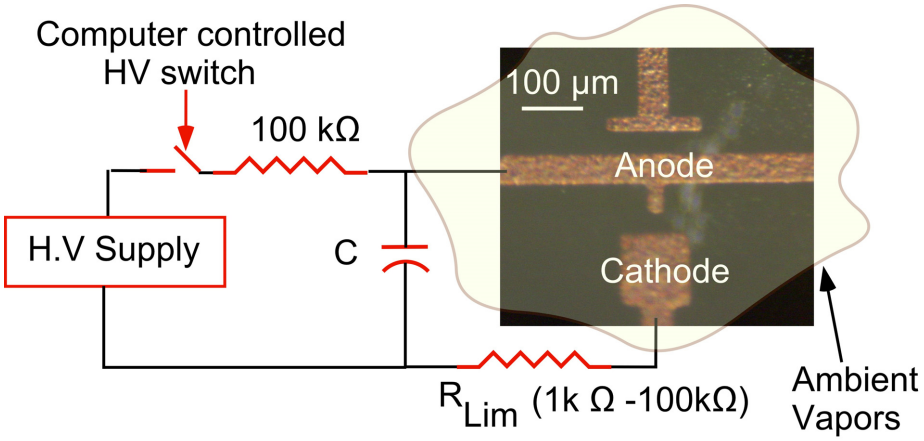

Fig. 4.1: Picture of the device and a simplified schematic of the circuit. The third electrode is not used. The anode-cathode gap is 75 µm.

The device fabrication begins by sputtering a Ti/Cu (50 nm/100 nm) seed layer on the glass wafer. Then a 50 µm thick layer of photoresist (Clariant AZ 9260) is spun on and patterned to define the mold for electroplating. A layer of copper, 40 µm thick, is then electroplated to define the electrodes. The photoresist is removed, and the base layers etched away to form the device. Thick electroplated copper is used to increase the device lifetime, as some sputtering of the cathode is inevitable in the microplasma.

4.2 Arc-Glow Behavior

When a large current limiting resistor is used, the discharge takes a form similar to a glow. These kinds of discharges are referred to as "cold discharges" and are characterized by high-energy (temperature) electrons and low energy (temperature) neutrals (gas molecules) existing in thermal non-equilibrium [Rai97]. For microscale geometries, the glow is confined to a space over the cathode surface. Most of the applied voltage drops across a small space charge region close to the cathode, resulting in a localized region with high electric field.

Electrons are emitted from the cathode surface with low energies (<1 eV) [Gil77]. This is not sufficient for ionization of the gas medium, so the space next to the cathode is dark. The electrons gain energy as they are accelerated by the electric field between the electrodes, and as the electron energy rises to levels large enough to excite atoms, a *cathode glow region* appears. When the electron energy rises to a level such that collision cross section for the excitation falls off, the electrons cease to excite atoms, and a *cathode dark space* is formed. This is the region where ionization (and avalanche multiplication) takes place and positive space charge builds up. The field near the cathode (from the cathode to the end of the cathode dark space) is extremely high, and is the main driving force behind the glow discharge. At the end of the cathode layer, the electron flux gets fairly large, and electrons generated at the end of the region have moderate energies. This leads to the formation of an intense *negative glow* region. For small inter-electrode gaps, and atmospheric pressure conditions, the negative glow and cathode glow overlap (these regions have finite thickness due to the spread in electron energy), and only one glow region is seen. In planar discharges the optical characterization typically involves observations from above, so the spatial variation in the glow is not observed and the glows appear as one.

In addition to the electrons, which participate in the breakdown process, there are also many "beam electrons" [Wil03]. These electrons, which do not undergo many collisions, have extremely high energy. Beam electrons are formed, because the capture cross-section of collisions between electrons and ions or neutrals is a function of the electron energy. For high-energy electrons, this cross section is low, as the interaction time between the electrons and the atom or molecule is small. Thus some of the electrons,

which do not undergo collisions in low energy state, are accelerated to very high energy. These beam electrons thus do not contribute to the breakdown process, and make the discharge less power efficient.

For a discharge to be self-sustaining, it needs a constant supply of electrons from the electrodes. In case of micro-glow discharges, these are supplied by secondary emission from the cathode surface. Secondary emission occurs when positively charged ions, accelerated through the space charge region, hit the cathode surface and release electrons. Secondary emission is favored in conditions where the collision frequency of the ions is low, like in low-pressure discharges. Photoemission is another important source for initial electrons. In this process, the UV photons from the discharge cause electrons to be emitted from the cathode surface by photoelectric emission. Electrode processes thus play an important role in these DC and pulsed microdischarges, and the discharge is very sensitive to changes in the work function and surface quality of the electrode material. For example, under conditions that are otherwise identical, changing the electrode material can change the discharge from a glow to an arc. The third source of electrons in microdischarges is thermionic emission (or field assisted thermionic emission). In micro-glow discharges, the main source of electrode heating is positive ion bombardment of the cathode. This heating causes a temporal variation in discharge characteristics in between pulses, and makes pulsed discharges very different from DC discharges.

The second mode of breakdown is the arc discharge. In an arc, the electric field is not as high as cold cathode discharges. Arcs can be vapor arcs or thermionic arcs, which themselves can be of several kinds [And91]. The arcs encountered in this research are thermionic spot mode arcs at high pressure as defined in [And91]. The main source of

electrons in an arc is thermionic emission from the cathode. Thermionic emission is a much more efficient process compared to secondary emission and photo-emission so only a few generations of avalanche multiplication are enough for the discharge to be self-sustaining. This is why arc discharges can be sustained at low voltages. For two terminal devices, arcs usually start as a glow discharge that then changes into an arc. Thus the initiation voltage for a two-terminal arc is high, but the sustain voltage is low. The currents, however, are high compared to a glow discharge, as the current density is required to heat the electrode to the temperatures required for thermionic emission are fairly high. The emission usually starts from a local hotspot on the cathode surface, causing the micro-arc discharge to appear as a narrow filament. Arc discharges exist in thermal equilibrium and have high plasma density. Because of this, the spectral distribution of an arc is very wide, and spans the range from UV to infrared wavelengths. Micro-arc discharges require much less current compared to conventional arc discharges. This is because arcs are driven primarily by thermionic emission, and it is easier to heat microelectrodes to high temperatures using less current. The volume of the air that is ionized in a micro-arc discharge is also much lower as a result of scaling, which makes it easier to generate arc-discharges with small inter-electrode gaps. They are usually generated by discharging a small capacitor across an air gap. The small air gap enables the use of smaller capacitors (or smaller amounts of charge), which allows good control of the properties of the discharges by using a limiting resistor. Control of the properties of the discharge is important, as uncontrolled discharges can lead to rapid deterioration of the electrode surfaces.

In hybrid microdischarges both arc and glow discharges are present together. In conventional discharges, arcs and glow discharges appear separately on account of different mechanisms. However, in small geometry microdischarges, both can exist simultaneously. This is because microdischarges are driven mainly by electrode processes. The field in the intermediate region is low in both micro-glow and micro-arc discharges. This allows two different electrode processes to take place simultaneously – space charge region formation near the cathode, and localized hotspots on the cathode from which arc-discharges nucleate. In a conventional discharge the glow rapidly degenerates into an arc discharge, and the intermediate phase where both are present is very short and difficult to control [Raz97]. In a microdischarge, however, owing to the dynamics of the discharge process and the small amount of charge delivered to the discharge, it is possible to realize such a stable intermediate.

To evaluate the electrical characteristics of the gas discharge microchip, an oscilloscope was used to examine the cathode and anode (through a 10 MΩ : 100 kΩ divider) waveforms. The anode waveform indicates the breakdown voltage, and the cathode waveform indicates the discharge current (drop across the limiting resistor). The discharge capacitor was 10 pF and the limiting resistor was varied from 1kΩ to 1M kΩ.

Figure 4.2 shows the current and voltage waveforms of a typical atmospheric microdischarge for an applied voltage of 630 V. An overvoltage is applied for repeatability and other reasons outlined in section IV. The initial breakdown occurs at a voltage of 630 V, but subsequently the breakdown voltage decreases to 400 V. The current waveform is comprised of two parts- a steady component, and a transient component which rides on the steady component. The steady component corresponds to

a glow-like discharge present over the cathode, while the transient component corresponds to an arc-like discharge present in between the electrodes. An oscillation corresponding to the arc-like component is seen in the voltage waveform as well. The surge in current is likely due to the formation of cathode spots (lasting a few μs) that are formed on the cathode surface [Kek72]. (Further justification for this is seen in optical and spectral data, shown in Fig. 4.3, Fig. 4.4 and Fig. 4.5) The current in this state is approximately given by the equation [Kek72]:

$$nev_d \exp\left(\int_0^d \alpha\, dx\right) + C\frac{dV}{dt} = \frac{V_0 - V}{Z}$$

where n is the electron density, v_d is the drift velocity, α is the Townsend ionization co-efficnent, Z is the effective impedance and $V_0 - V$ is the voltage drop across the series impedance. The arc current corresponds to the discharging of the capacitor (C), while the glow discharge component represents the term on the left.

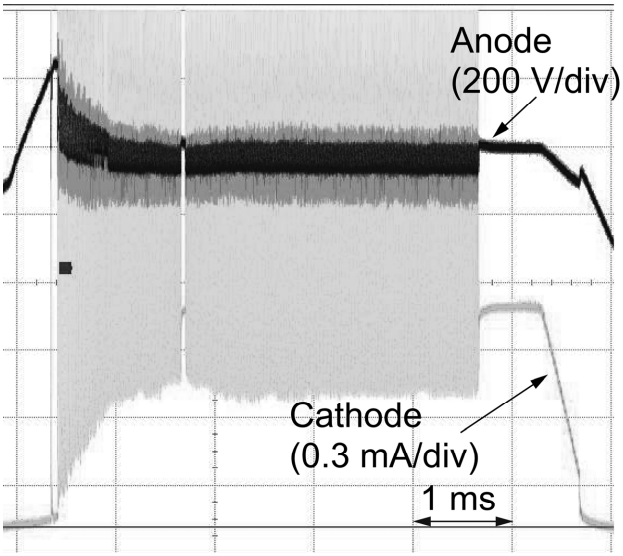

Fig. 4.2: Typical discharge voltage and current waveforms for an arc-glow discharge hybrid discharge.

Figure 4.3a shows a photograph of a micro-glow discharge at atmosphere. A bright glow is seen in the region above the cathode and near the anode, with dark space in between. The images of the transient discharge are captured by a video camera at 25 frames per second. The discharge is characterized by a steady current throughout the duration of the discharge. Figure 4.3b shows the current waveforms for such a glow discharge, measured by the voltage drop across the 100 kΩ current limiting resistor to ground. A current spike is seen at the beginning of the discharge, corresponding to a weak arc-like component. Spectral characterization is performed by observing the discharge with a handheld Ocean Optics™ spectrometer. Figure 4.3c shows the spectra for the glow-like discharge described above. The discharge shows a strong emission in the UV-blue region, but very little emission in other regions of the spectrum. The blue color is primarily due to emission from N_2 second positive ($C\ ^3\prod - B\ ^3\prod$ — 337. 1 nm, 357.5 nm, 375.1 nm, 380.4 nm) and N_2^+ first negative ($B\ ^2\sum^+_u - X^2\sum^+_g$ — 391.4 nm) systems. Sensitivity at deep-UV wavelengths (300 nm and lower) is limited due to losses in the fiber optic cable.

When a small limiting resistor is used, the discharge is arc-like. This allows for large transient currents necessary for rapid heating of the plasma. Figure 4.4a shows a picture of the discharge glow for an arc-like microdischarge. The bright glow is present in the gap between the electrodes rather than over the electrodes and is much brighter compared to a glow discharge. Figure 4.4b shows the current waveform when using a 2.2 kΩ current limiting resistor. The average current is 4.2 mA. The discharge is a succession of tiny discharges powered by high current spikes. The capacitor repeatedly charges up to the breakdown voltage required for plasma formation, and dumps all the charge stored in

surges of current. The surge in current is due to the formation of cathode spots (lasting a few μs) that are formed on the cathode surface [Kek72]. There is a steady glow like component, which is much weaker. These discharges are different from pure arc discharges, which occur when smaller resistance (<1 kΩ) and/or higher capacitance is used, and are characterized by much higher currents and no steady (glow) component. Figure 4.4c shows the spectrum for the above discharge. Strong lines in the green-red region of the spectrum, which were not present in the spectrum of the glow discharge, become apparent now, but many of the lines present in the UV-blue region of the spectrum are absent. The spectrum shows prominent emission from copper (324. 7 nm, 327.33 nm, 510.84 nm, 515.8 nm and 522.07 nm).

The surge in current is due to the formation of cathode spots (lasting a few μs) that are formed on the cathode surface [Kek72]. As shown in Fig. 4.4a, there is a green emission from the cathode hotspot that is not present in the glow discharge (Fig. 4.3b). The copper lines in the emission spectra of the arc discharge (Fig. 4.4c) also point to emission from a cathode hotspot.

With an intermediate current limiting resistor, the discharge shows both arc-like and glow-like components. Figure 4.5a shows a picture of a typical discharge. A glow discharge over the electrodes and an arc-like discharge in the gap region, corresponding to the arc/glow portions of the discharge respectively can be seen. When seen optically the discharges are simultaneous, but the waveforms suggest that the arc-like discharges might occur as instabilities in the glow discharge. Figure 4.5b shows the current waveforms for the discharge with the limiting resistor set to 33 kΩ. The current waveform shows both a steady (glow) and an erratic (arc) component. Figure 4.5c shows

the spectrum in air when a hybrid discharge was initiated when using a 33 kΩ limiting resistor. This spectrum contains both long and short wavelength lines corresponding to both arc-like and glow-like components. The emission spectrum shows lines from both copper from the electrode hotspots and nitrogen in air.

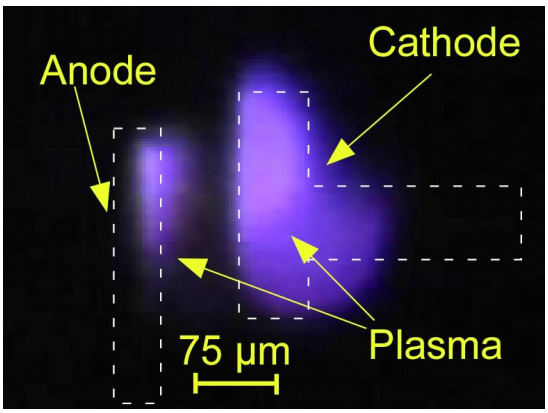

(a)

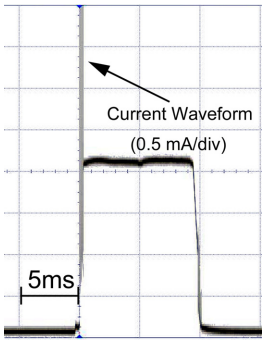

(b)

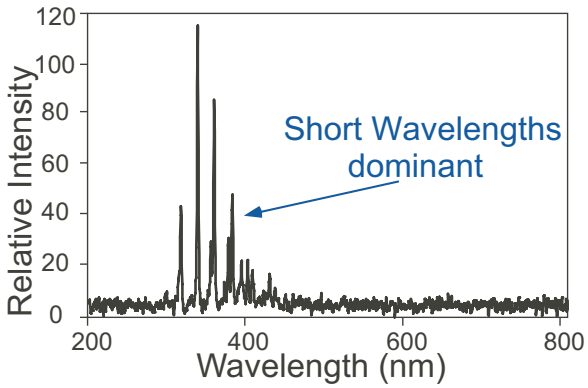

(c)

Fig 4.3 (a): Example of a glow-like discharge. The glow is confined to the cathode and near the anode. (b): Oscilloscope waveforms show a steady current (c): Emission spectrum of the glow-like discharge in air.

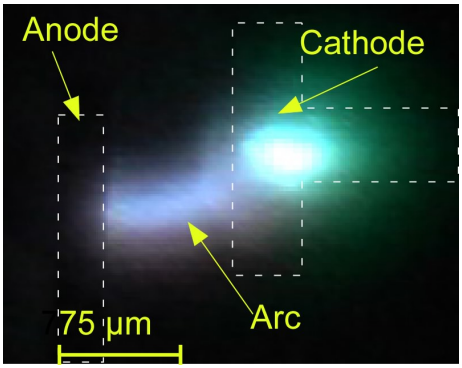

(a)

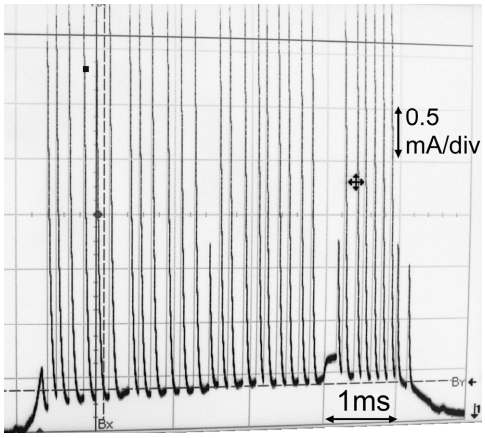

(b)

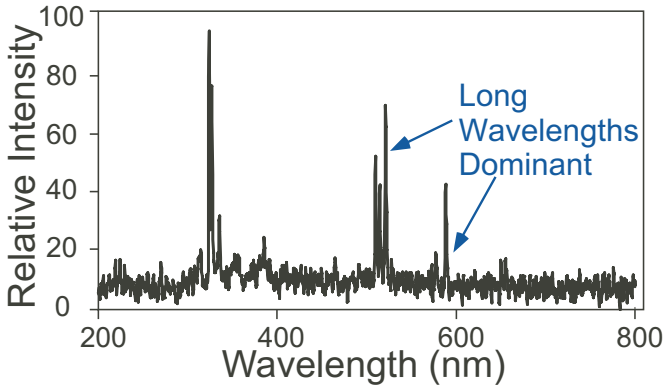

(c)

Fig 4.4 (a): Example of an arc-like discharge (b): Current waveform shows discharge is powered by transient bursts of current (c): Emision spectrum of an "arc-like" discharge. The spectrum is dominated by emission from copper (324. 7 nm, 327.33 nm, 510.84 nm, 515.8 nm and 522.07 nm)

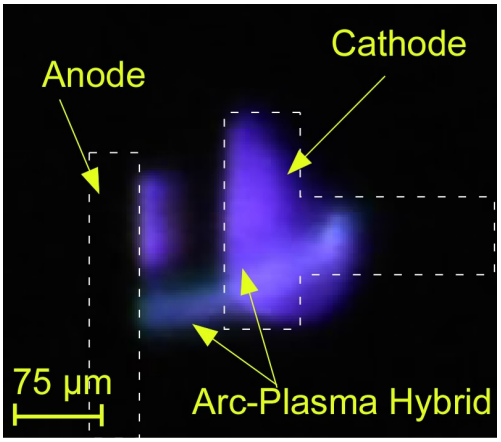

(a)

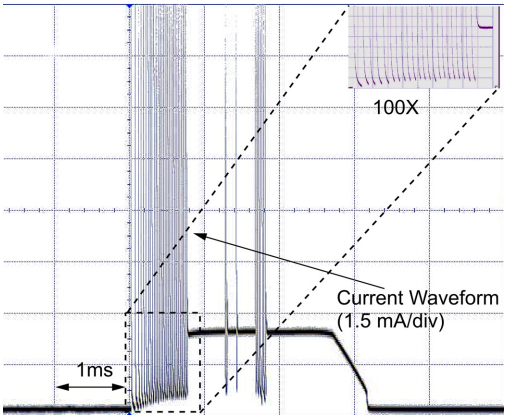

(b)

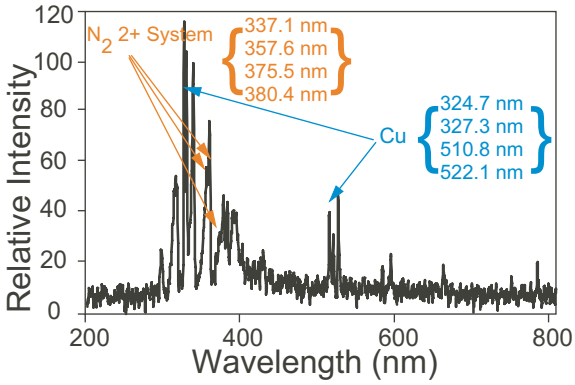

(c)

Fig 4.5 (a): Example of an arc-glow discharge hybrid, showing both components. (b): The current waveform shows both transient and steady component corresponding to the two types of discharges, (c): Emission spectrum is a mix of both glow and arc-like spectra, having emission both in the UV-blue and green region. The spectrum is dominated by emission from copper (324. 7 nm, 327.33 nm, 510.84 nm, 515.8 nm and 522.07 nm)

Pulsed discharges are not just short-duration DC discharges. They differ from DC discharge in significant ways. In a pulsed discharge, the interval between pulses affects the nature of discharge considerably. DC discharges tend to be arc-like, even for resistances as high as 200 kΩ. In pulsed discharges, if the interval between pulses is short (typically 2s or lower), significant variations are observed from one pulse to the next. For example, there can be a cyclical variation in breakdown voltage and the discharge alternates between being arc-like and glow-like. This is because each pulse is affected by the pulse preceding it in a significant way. This variation may be attributed to electrode and gas heating effects, which persist after the current, has been turned off. These tend to lead the glow-like discharge to degenerate into arc-like discharges. In arc discharges electrode degradation occurs at the electrode hotspot, so arcs revert back to glow discharges in the next pulse. Instead of the device settling in a stable equilibrium discharge, a cyclical variation is seen. When the interval between pulses is large (>5s), the effect of the previous pulse is not as important, and the discharge tends to be more stable.

4.3 Measurements

The electrical characterization of the discharge was performed by varying the applied voltage and limiting resistor. The I-V curve for the glow component (Fig. 4.6) is obtained by measuring the current through the discharge with different biases and limiting resistor values. No breakdown takes place for voltages less than 460V. Larger voltages show increasing current, with a differential resistance of 80 kΩ. The external circuit is represented by the load line on the I-V curve. The system settles to a point at the intersection of the load line and the device I-V curve, so a particular state can be achieved by controlling either the overvoltage or the resistor. This I-V curve is valid only

for resistance values between 1 kΩ and 1M. Below 1kΩ resistance the discharge is dominated completely by the arc component.

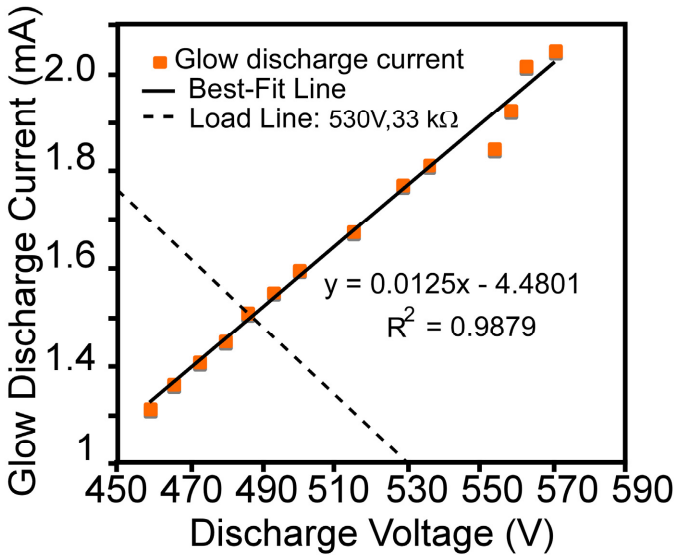

Fig. 4.6: I-V curve for the glow discharge component of the discharge

The arc-component of the discharge is not a strong function of applied voltage. Arcs are generally driven by current rather than voltage, and these discharge are no exception. The arc-like discharge is powered from the energy stored in the capacitor. Even if no capacitor is used the parasitic capacitance of the device (~ 2 pF) supplies the energy (the initiation of breakdown is erractic when not using parasitics, so a small capacitor is used in operation). The capacitor oscillates between the glow discharge breakdown voltage and the arc-breakdown voltage. The power delivered by the capacitor is given by $P_c = \frac{CV_{bkdn}\Delta V}{\tau}$, where τ is the time constant, V_{bkdn} is the breakdown voltage, and ΔV is the amplitude of the voltage oscillations.

The time constant of the discharge is related to the time constant of the discharge resistor. Fig. 4.7 shows a plot of the measured time-constants for the arc-like discharge

for various limiting resistors. The time constants were obtained by fitting the current waveform to a decaying exponential. It is seen that the time constant is linearly related to the limiting resistor.

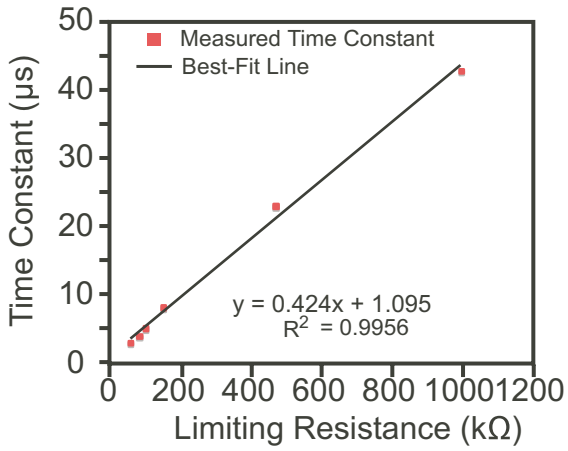

Fig. 4.7: Time constant of the arc-like component as a function of limiting resistance

The effect of inductance is evaluated by placing an inductor between the limiting resistor and ground, and measuring the time constant for various inductor values. No significant change was observed in time constant when the inductance was changed from zero to 2 µH. The time constant is not related to inductance of the arc in this case, contrary to traditional arc models where arc inductance plays a major role in the duration of the discharge [Rob88]. The addition of even a small inductor lead to a ringing in the arc waveform, with a high frequency ac superposed on the decaying exponential. This did not have an effect on the powering of the arc.

The time constant is related to the capacitance in a complex way. On increasing the capacitance from 15 pF to 25 pF, the time constant changed from 6.53 µs to 8.61 µs. However increasing the capacitance to 50 pF led to discharge instability and the

discharge was no longer an arc-glow hybrid, but an intermittent arc discharge. The hybrid discharge thus operates only in a narrow range of capacitance values and higher values of capacitance are likely to lead to non-linear effects that result in a runaway process.

The current component of the arc discharge depends upon the value of the limiting resistor. Fig. 4.8 shows a plot of the arc current versus the conductance of the limiting resistor. The fit shows a linear relationship between the arc current and conductance of the limiting resistor. It is thus seen that the limiting resistor can be used to control the current of the arc-like discharge. It is noteworthy that the arc-current does not depend upon the overvoltage. For the case of using a 1 MΩ resistor, the increase in applied voltage from 630 V to 700 V did not lead to a change in arc current. This result is important because as shown earlier, the glow discharge component strongly depends upon the overvoltage. Thus by using a proper combination of limiting resistor the arc and glow components of the hybrid discharge can be controlled.

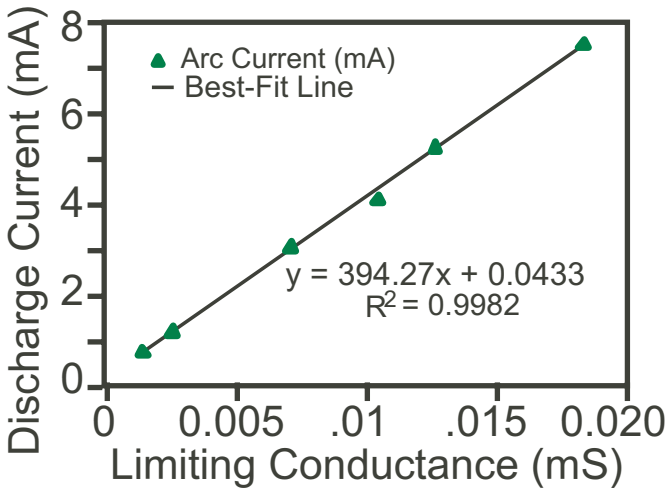

Fig. 4.8: Discharge current for the arc-like component as a function of limiting resistance.

While the power of individual pulses in the arc-like discharge can be controlled by using circuit elements, the number of arc-like pulses is difficult to control. The number is lower for higher resistances, but there is still significant variation between pulses. This is probably because the effect itself is as a result of some instability in the discharge process. It is clearly seen that the discharge is predominantly glow like at lower pressures (~450 Torr), which suggests that it is probably related to heating by electron-neutral collisions. The electrode material also has a significant impact on the nature of the discharge. When using iridium instead of copper a predominantly arc-like discharge was seen.

To evaluate the hybrid micro arc-glow device as a vapor sensor, the devices were placed in a chamber into which acetone vapor samples were introduced (Fig. 3.4). Air was used as a carrier gas and the pressure inside the chamber was maintained at 810 torr. A vacuum pump was used to evacuate the chamber from impurities before the experiment, but was not used during the experiment. A commercial vapor sensor (MiniRAE 2000) was used as a benchmark. The device was operated in hybrid mode with the limiting resistor set to 22 kΩ. A hybrid discharge was chosen as it had the strongest emission in the wavelength range of interest (350 nm-450 nm). One-shot detection was performed, with pulse duration of 45 ms.

Figure 4.9a shows a portion a typical microdischarge spectrum (300 nm-400 nm) taken in 17 ppm ambient of acetone. In the absence of pre-concentration of sample vapors, this is a significant challenge for a microsensor, especially when using portable optics. The spectrum shows a line at 388.6 nm that corresponds to CN fragments produced from acetone in the air microdischarge [Pea62]. This line is absent from the

control spectra taken in air (Fig. 4.9b), and at high concentrations it dwarfs all the other lines. Note that the spectra are normalized to the strongest line. In the spectrum for 4000 ppm acetone, shown in Fig. 4.9c, the nitrogen lines seem diminished, not because the nitrogen emission is diminished, but because the carbon line is very intense due to the high vapor concentration.

A calibration curve for acetone (Fig. 4.10a) can be obtained by measuring the 388.6 nm line intensity for different concentrations of acetone. The background signal on which the line is superposed is accounted for by subtracting the average of line intensities at two inflection points (390.3 nm and 387.28 nm) from the line intensity at 388.6 nm. This is normalized to the 391.4 nm nitrogen line to compensate for the optical power of the discharge. Since the lines are close together, variation in electron energy distribution function between different discharges are not likely to affect their ratios. The relative line strength is not expected to increase linearly with acetone concentration because cross-sections for excitation by electron impact are likely to be different for the two molecules. The calculation, shown graphically in Fig. 4.10b, is represented by the formula:

$$Line\_Strength\left(388.6nm\right)=\frac{I(388.6)-\left(\frac{I(390.3)+I(387.28)}{2}\right)}{I(391.4)}$$

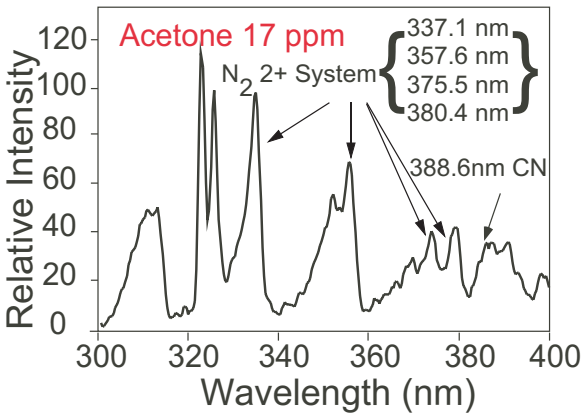

(a)

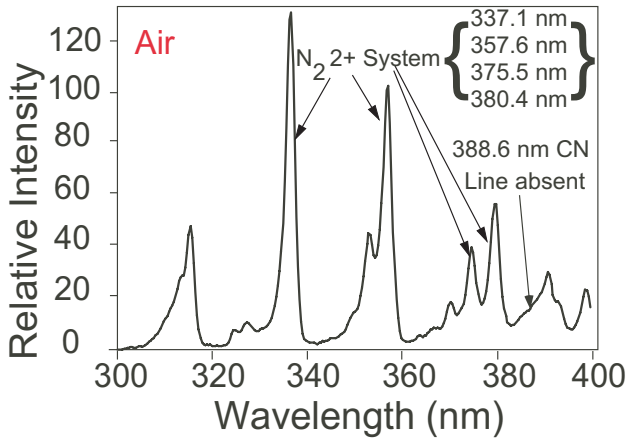

(b)

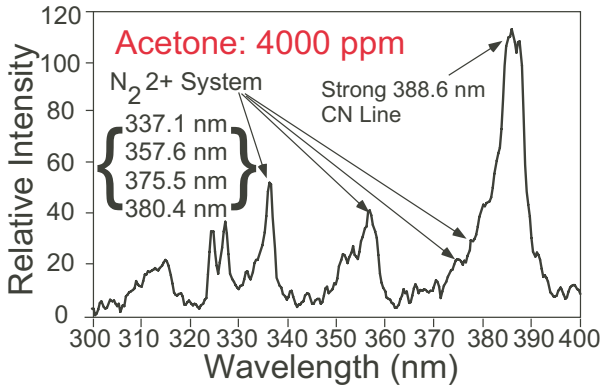

(c)

Fig. 4.9: Spectra from the gas discharge microchip (without pre-concentration). (a): In 17 ppm acetone showing the presence of 388.6 nm emission from carbon containing fragments. (b): Control experiment in air. The 388.6 nm line is absent.(c): The relative intensity of the 388.6 nm is much more with higher acetone concentration.

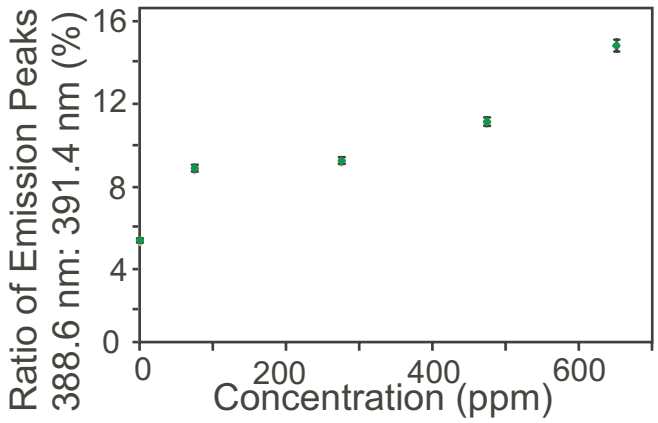

(a)

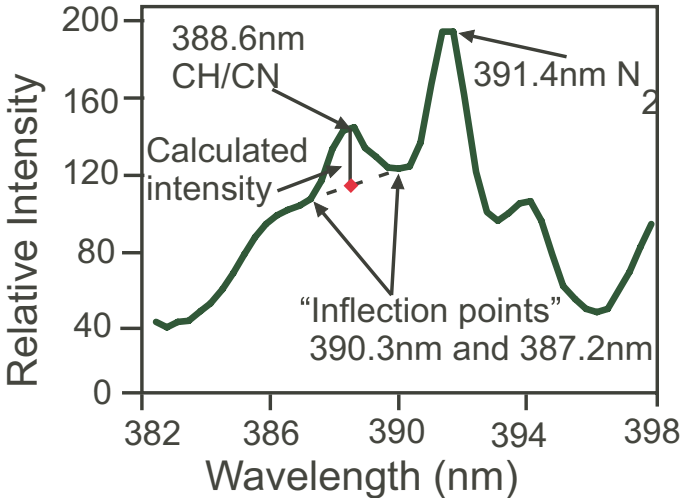

(b)

Fig. 4.10 (a): Calibration curve showing variation in the normalized CN (388.6 nm) line intensity as a function of acetone concentration. The line strength is normalized to 391.47 nm nitrogen line to account for variation in optical intensity of the discharge. The data at 0 ppm represents the control signal in air. (b): Calculation of the line intensity. The 388.6 nm line is superposed on a background signal. The background compensated for by subtracting the average of line intensities at two inflection points (390.3 nm and 387.28 nm) from the line intensity at 388.6 nm.

4.4 Conclusions

This work demonstrates that by using an appropriate discharge gap, and drive circuitry, it is possible to control the electrical and optical characteristics of the atmospheric microdischarge. Pulsed microscale discharges at atmospheric pressure can occur as glow discharges, arc discharges or as a combination of the two in the form of arc-glow hybrids. The presence of a stable intermediate between arcs and glows is a feature of microdischarges. Micro-arcs have a wide spectral distribution in emission, while microglow discharges have strong but narrow band emission mainly in the UV-blue region, when using air as the carrier gas. The micro-arc is driven by bursts of current while a steady but small current drives the microglow discharge. The glow discharge current can be controlled by the limiting resistor and the overvoltage, while the arc component is can be controlled by the limiting resistor. Using these it is possible to adjust the spectral output to desired levels.

The application of these discharges to chemical sensing is demonstrated by generating a calibration curve for sensor output for concentrations acetone concentrations ranging from 50 ppm-1000 ppm. The 388.6 nm CN line is used as a benchmark and 394.1 nm emission from N_2^+ is used as a normalization. It is shown that the device can distinguish 17 ppm of acetone in air ambient in a 65 ms detection time, without using any pre-concentration.

Chapter 5 Three-Electrode Discharges

In two-electrode discharges the same electrode is used for initiating and "heating" the microplasma. Initiating a discharge requires high voltages to provide the high field necessary for breakdown. Heating the discharge (to make the discharge glow brighter) requires pumping energy into the discharge and in the simplest case this is done by pushing current through it. When the same electrode is used as both high voltage and current electrodes, it is difficult to control the power to the discharge independently of voltage and this leads to excessive power consumption and heating. If on the other hand one set of electrodes is used for initiating the discharge, causing the gas to become conducting, and another set of electrodes, at a lower voltage is used to provide energy to the discharge by pushing current through it, power transfer is a lot more efficient [Gol94]. So by using a combination of a weak discharge and a non self-sustaining discharge a much more efficient method of powering is obtained. Also, since the heating of the discharge does not depend upon electrode processes, such a discharge can also have a reduced wear rate, while still maintaining a significant level of ionization. These three-electrode discharges are the topic of this chapter.

5.1 Device Structure and Fabrication

With the intention of limiting the energy in the discharge, the flashFET (Fig. 5.1) has two important structural differences from the two electrode scheme: (i) it uses a

strategically located high-impedance electrode with a fixed bias; ii) one of the two low impedance electrodes is capacitively powered to limit the discharge energy. In analogy with a field-effect transistor (FET) the high impedance electrode is labeled the gate, the capacitively driven electrode is anodically biased and is labeled the drain, and the third electrode is cathodically biased and labeled the source (Fig. 5.1) Since the microplasma glow is confined to the cathode, the source area is larger relative to the other electrodes to permit a large glow area. Increasing the electrode area also helps to prevent hotspots and overheating of the electrodes, for a given power level. The drain is next to the source, with a typical spacing of 200 μm, and the gate is further away, spaced 450 μm from the source.

In this manifestation of the device the copper electrodes are used with the expectation that its low electrical and thermal resistivity results in reduced energy loss in the conductor. Electroplated copper is also a standard IC process layer and its selection underscores the promise of this structure for integration. With high voltage pulsed discharges, some electrode wear is inevitable, so the thick electroplated films extend the lifetime of the device. Excluding the contact pads, the device occupies a footprint of 1 mm^2. The device is optionally covered with a glass dust cap that permits free exchange of vapor with the sample space. Channels are grooved into the cap to permit free diffusion of the ambient gas into the discharge area. Glass capillaries may be inserted into the channels to allow operation with a gas flow. However this option was not utilized in the measurements described in thiswork . Prior to installment in the measurement system, the devices are rinsed in acetic acid to remove any accumulated native oxide. After installation the discharges themselves sputter clean the electrodes.

The gate electrode is maintained at a high voltage to facilitate the initiation of the discharge with a relatively low voltage pulses (≤100 V) between the source and drain. A 20 MΩ resistor and an inductor are connected in series to the gate electrode to reduce the gate current and eliminate it as a significant current path during the discharge. It will be shown that this keeps the energy consumed per discharge in the μJoule range. The control of the pulse timing and energy is crucial, as it is generally observed that high level of fragmentation occurs only in the initial (pre-peak) portion of a pulsed discharge [Kin 00]. By selectively delivering power to only this initial portion of the discharge, efficiency can be enhanced without sacrificing sensitivity. The location of the drain close to the source ensures that the discharge current favors the drain over the gate or any other element. The drain is connected to a series capacitor. This permits the charge on it to build up to a value approaching the gate bias, which is below the breakdown voltage. The charging current is an extremely small leakage current (0.22-0.5 nA) from the gate electrode and through the reverse leakage resistance R_p of the diode.

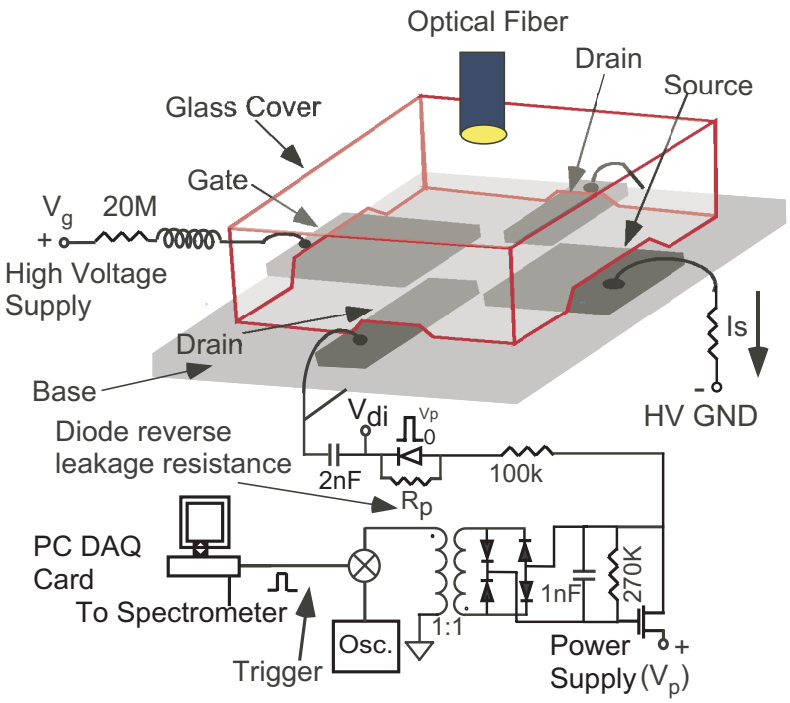

Fig. 5.1: Schematic of the micromachined flashFET, showing the electrode configuration, the glass cover and the discharge circuit. The gate is held at a high voltage, but the current is restrained by a 20 MΩ resistor and choke. A low voltage (~100 V) pulse applied to V_{di} is used to trigger the microdischarge.

During testing, it is essential that no instrumentation probe (e.g. an oscilloscope) be connected to the drain. Even if a high impedance (20 MΩ) probe is connected, the drain gets pulled to ground due to the extremely large gate impedance. Then, because the drain is physically close to the gate, (which is held at an elevated voltage) unintended discharges can be initiated between the gate and drain. In the absence of a probe the drain charges to the floating potential as described above. When a discharge is required, a relatively small pulse (≤100 V) from the control circuit boosts the drain above the threshold, initiating the microdischarge to the source. The current in the microdischarge decays as the capacitor is discharged.

The fabrication process for the flashFET (Fig. 5.2) starts with a blanket Ti/Cu (100 Å/500 Å) base layer sputtered on a glass substrate. The photoresist (Clariant AZ 9260) is patterned to define a 50 μm thick mold for the plating. A layer of copper, 40 μm thick, is then electroplated through the mold to define the electrodes. The photoresist and the base layers are then etched away to leave the flashFET structure intact. The cap wafer is made by forming a cavity (2 mm x 2 mm) into #7740 Pyrex^{TM} glass wafers of ≈750 μm thickness. Channels (250 μm wide) leading from the perimeter of the device into this cavity are also etched in the same step. The cavity and the channels are formed by an HF/HNO_3 wet etch. A layer of Cr/Au (500 Å/5000 Å thick) covered with photoresist is used as an etch mask. An alternative to the wet etch is to simply groove the glass wafer with a saw. This can provide channel depths up to 300 μm facilitating a coupling to gas chromatography capillaries. Finally the device and the cap wafer are diced the cap is bonded to the device.

The cap can be clear but an optical diffuser cap is favored for ease of alignment to the optical fiber. The diffuser cap is made by dispensing a 0.2g/ml dispersion of glass microparticles (3-10 μm diameter) on the clear cap coated with UV curable epoxy. After curing, the cap is bonded to the device by UV-curable epoxy. The device can also be packaged at wafer level by bonding the glass wafers and dicing top and bottom wafer separately.

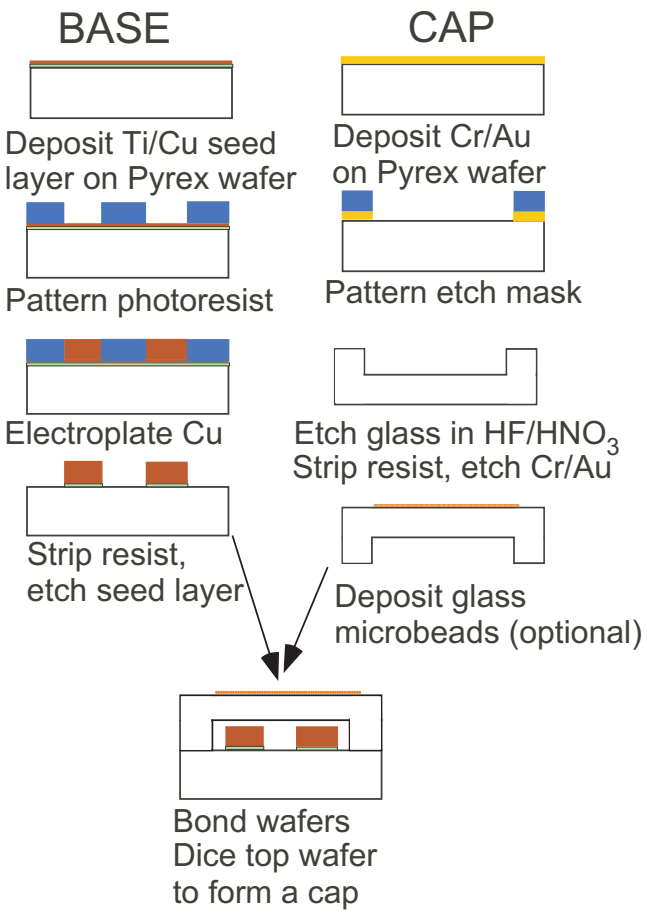

Fig. 5.2 : Fabrication process for the flashFET. Left: The base wafer. A 500 Å/1000 Å layer of Ti/Cu is deposited by sputtering. Photoresist (Clariant AZ 9260), 50 µm thick, is patterned to serve as a mould for electroplating. A layer of copper, 40 µm thick, is electroplated and the photoresist and the seed metal are etched away. Right: The top cap is formed by isotropically etching a cavity in glass. The cap and the base layer are bonded together

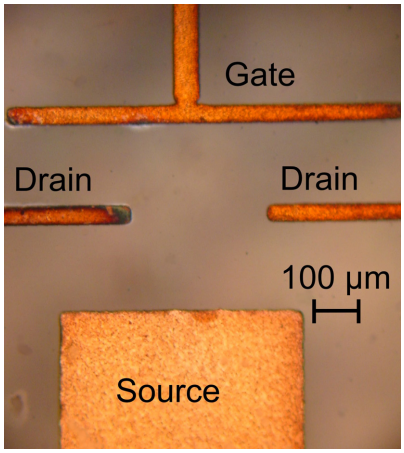

(a)

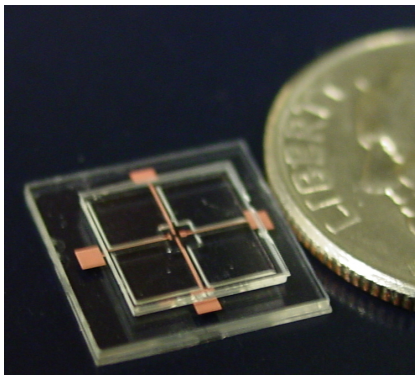

(b)

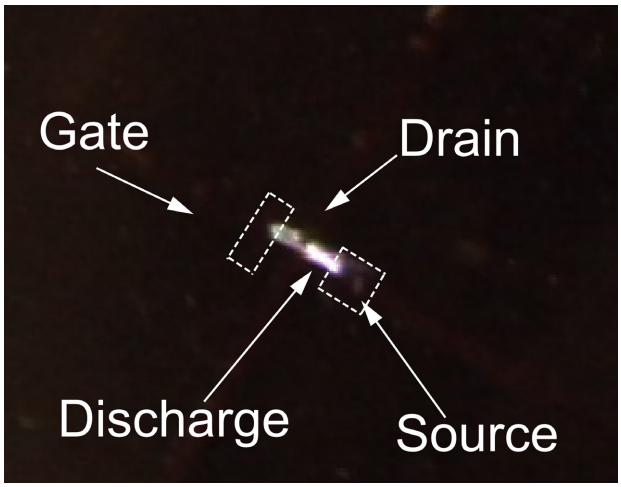

(c)

Fig. 5.3:(a) Optical micrograph of the flashFET without the cap showing the various electrodes. (b) Photograph of the packaged flashFET against a US dime. (c) Picture of a typical flashFET discharge.

5.2 Experiments and Results

Figure 5.3a shows a picture of the active area of the microfabricated three-electrode (flashFET) device (without the glass cap.) This particular design employs a split drain. Devices with a single drain line running end to end have also been tested and show

identical results. The final packaged device, shown in Fig. 5.3b, occupies an area of 1 cm x 1 cm.

A typical flash (Fig. 5.3c) is seen as a narrow glowing filament between the source and drain. The image was captured by a video camera running at 25 frames per second attached to a microscope. Unlike a two-electrode discharge the glow is located in between the electrodes. The exact spot of breakdown however is not consistent and varies from pulse to pulse, and is one of the reasons why optical alignment is difficult. A faint glow is also seen between the drain and gate, although this is not a very consistent feature.

Figure 5.4a represents the idealized waveforms for the power measurement experiments. It shows the microdischarge trigger (top), pulse voltage and discharge current. The pulse voltage corresponds to the voltage V_{di} shown in Fig. 5.1, for three-electrode microdischarges or the anode voltage for two-electrode microdischarges. The duration of the discharge corresponds to the time that the current flows (t_i), which is much smaller than the voltage pulse duration for three-electrode discharges.

In order to compare the power consumption using copper electrodes for both the two- and three-electrode configurations, a separate set of experiments were done at the reduced pressure of 140 Torr. (Note that for atmospheric pressure operation, we would normally not use copper at these electrode spacings, for the two-electrode configuration because it leads to excessive sputtering.)

Figure 5.4b shows the oscilloscope waveforms for a two-electrode pulsed microdischarge between the drain and the source, taken in air at 140 Torr pressure. At the top is the trigger signal; in the center is the voltage waveform at the drain, observed

through a 100:1 voltage divider; at the bottom is the current through the source, measured by the voltage across a 10 kΩ resistor connected in series with the source. At these pressures the discharge takes the form of plasma, with the glow confined to the cathode [Wil03]. As shown in the figure, the breakdown voltage was 515 V. The peak current was 3.5 mA and the energy dissipated in one cycle was 0.47 mJ. Note that the capacitor did not discharge all the way and the voltage was maintained at a slightly lower sustain voltage throughout the duration of the trigger.

Figure 5.4c shows the oscilloscope trace for a flashFET microdischarge at the same pressure as in Fig. 5.4b, for comparison, with the gate voltage, V_g, held at 800 V. In the figure the center waveform is the current signal, and the waveform at the bottom is the voltage signal V_{di}. The drain cannot be probed directly for reasons explained in section 5.1.

The energy consumed was calculated by summing the output of both power supplies for V_g and V_{di} over the duration of the cycle. The flashFET consumes 2.5 μJ/cycle at 140 Torr, which is a 1000x reduction over the two-electrode configuration. The device still forms a plasma glow over the cathode, but unlike the two-electrode microdischarge, lasts for a short duration (~200 μs). This factor alone helps reduce the power consumed by 50x. Between the source and drain, a much lower voltage (100 V) is needed to trigger the discharge with a three-electrode configuration. Unlike the two electrode discharge, V_{di} drops to zero within 0.4 ms, which implies that in the case of a flashFET discharge, the capacitor discharges completely. Also it is notable that although the voltage waveform shows a second dip, the current waveform does not show a current peak, so a very small amount of power is delivered with the second (spurious) discharge pulse.

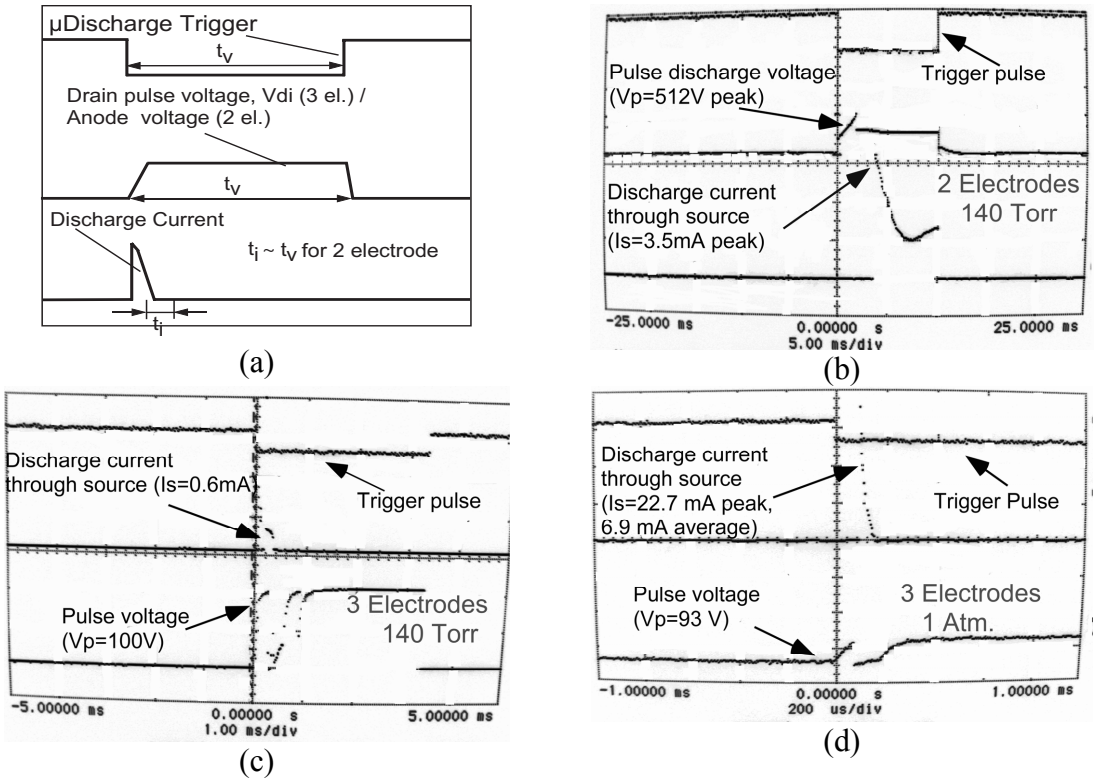

Fig. 5.4:(a) Idealized waveforms for the microdischarges, showing the trigger signal, drain pulse voltage (Vdi –see fig. 5.1) or Anode voltage for two electrode microdischarges, and discharge current waveform. (b) Waveforms showing the formation of a two-electrode pulsed microdischarge in air at 140 Torr. (c) Waveforms showing the flashFET microdischarge at 140 Torr with V_g=800 V. The power per cycle is calculated by summing the output of the two power supplies. This discharge consumes 2.5 µJ/cycle. (d) Waveforms showing the flashFET microdischarge at atmosphere, with V_g= 1000 V. The device consumed 22.5 µJ/cycle.

Figure 5.4d describes the flashFET microdischarge at 1 atm., the desired use condition. The gate was held at 1000 V. The trigger pulse applied to the drain was 93 V, and the peak current was 22.7 mA, and average current was 6.9 mA. Note that the timescale on the trace is smaller than in Fig. 5.4b and Fig. 5.4c, as the microdischarge at atmospheric pressure has a shorter duration (although the current peaks are larger). In this case, the energy consumed was 22.5 µJ/cycle. This is 100x smaller than a two-

electrode microplasma at 140 Torr. Also note that there is no second dip in voltage in this case, in contrast to the one at 140 Torr.

Table 5.1: Comparison of the electrical characteristics of two and three electrode discharges. Note that for normal operation at 1 atmosphere, the two-electrode configuration used Ti electrodes; Cu electrodes were used in all other cases. G-S and D-S respectively denote the gate-to-source and drain-to-source spacing.

Config.	Discharge Gap, Elect. Material	Current Mag.	Current Duration (t_i)	Pulse Voltage	Energy/ Pulse	Sample Spectra
Normal Operation at 1 atm.						
Two El.	300 μm; **Ti electrodes**	9.5 A	2 μs	520V	9.8 mJ	Fig. 6, 8
Three El.	G-S: 450 μm; D-S: 200 μm; **Cu electrodes**	22.7 mA peak; 6.9 mA avg.	70 μs	93 V trigger; 1000 V gate	22.5 μJ	Fig. 11, 12
Comparison of Cu electrodes in two- and three-electrode configurations at 140 Torr						
Two-El.	200 μm, **Cu electrodes**	3.5 mA peak 1.4 mA avg.	6.5 ms	512 V	0.467 mJ	
Three El.	G-S: 450 μm; D-S: 200 μm; **Cu electrodes**	0.6 mA	200 μs	100 V trigger; 800 V gate	2.5 μJ	

Figure 5.5a shows the spectrum of the microdischarge in air with an acetone concentration of 320 ppm at atmospheric pressure. The spectrum is similar to the two-electrode spectra in that it has line spectra superposed on a wider background. Lines corresponding to carbon fragments can be clearly seen. Figure 5.5b shows the spectrum of air with no acetone vapors. The carbon lines are absent, indicating that the lines were indeed due to the presence of acetone vapors.

Response characterization is performed using a half–meter monochromator spectrometer (SPEX 500M, from Jobin Yvon Inc.) that provided even higher spectral resolution, but lower spectral range. The slit width is set to 100 μm at both the entrance and the exit. The grating has a groove density of 1200 lines/mm, and the grating resolution is 0.02 nm. The resolution of the system is limited by the slit width to 0.16 nm (calculated). The positioning system has an accuracy of 0.05 nm.

Good optical coupling is crucial because the optical source has low intensity source at small power levels, and the characterization involves examination of a weak line in the discharge. It is particularly important while performing low concentration measurements. The alignment must address two challenges: The discharge appears as a tiny (3-10 micron wide) filament across the electrodes and lasts for extremely short duration, and the exact spot for the breakdown can vary slightly from pulse to pulse. These problems are easily overcome by using an optical diffuser cap to spread the light over a larger area. A 50X UV objective (from Mitutoyo Instruments) was used to magnify the spot. The monochromator had a fiber input, terminated with a collimating lens. A beam splitter assembly was used to provide the illumination while aligning. During operation, the light source was turned off, and the side output was used to visually inspect the discharge.

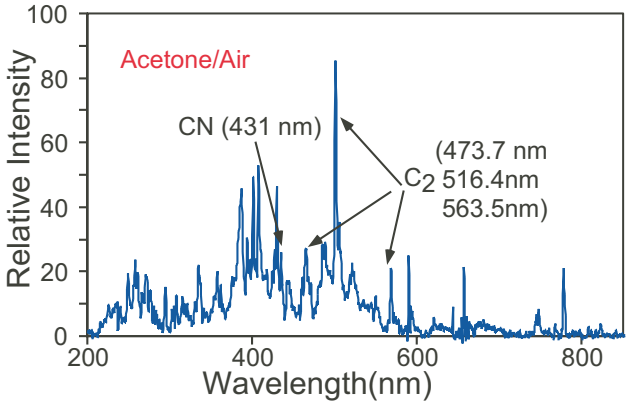

(a)

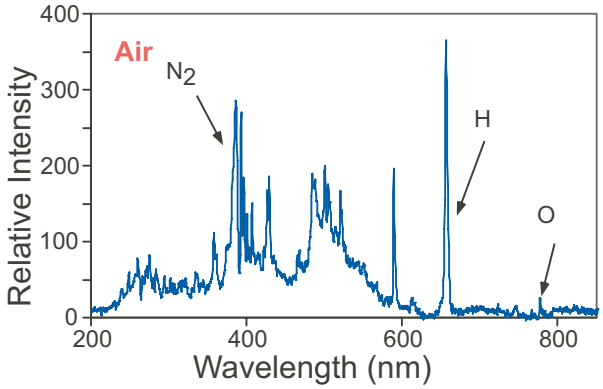

(b)

Fig. 5.5:(a) Spectra of the microdischarge in 320 ppm acetone with air (at atmos.) as the carrier gas. Lines corresponding to fragments of carbon compounds are clearly evident. (b): Control spectra of the flashFET discharge in air at 1 atm. Lines corresponding to nitrogen and water vapor dominate, but no carbon lines are present.

The output of the monochromator was coupled to a photomultiplier biased at 900 V. The output of the photomultiplier was coupled to a low noise amplifier (SRS570 from Stanford Research Systems). The amplifier was operated with a gain of 10 mA/V, and a 12 dB low pass filter at 500 Hz. The output of the amplifier was connected to a digital

multimeter (HP34401A), which was read out over a GPIB connection. Fig. 5.6 shows a schematic of the test setup.

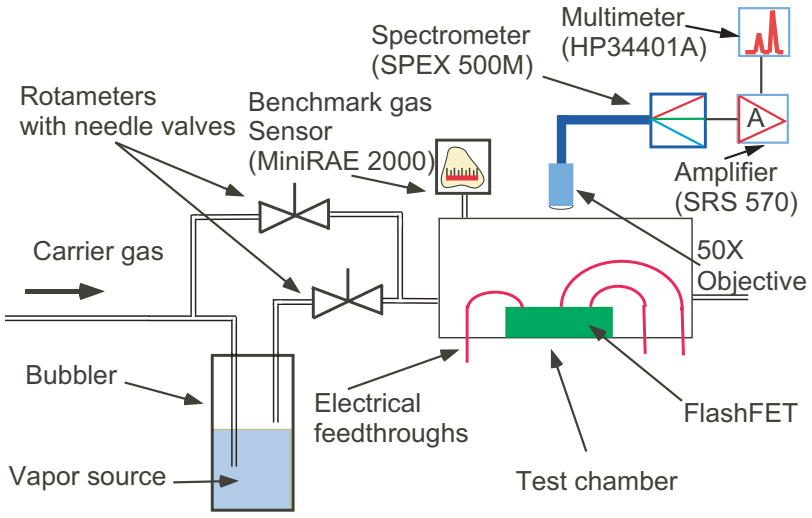

Fig. 5.6: Test set-up for sensor. Vapor concentration is varied by flow rate of carrier gas through a bubbler containing the compound of interest. A commercial vapor sensor (MiniRAE 2000 from RAE Systems) provides a benchmark measurement. The optical signal is observed through a fiber optic cable, connected to a palmtop spectrometer. For some experiments, a handheld spectrometer (USB 2000 from ocean optics) is used instead of the spectrometer shown in the figure.

To perform the experiment, the monochromator was positioned to the desired wavelength using the monochromator readout. A reference scan was performed in helium to calibrate the monochromator. He I (388.86 nm) line was profiled. Fig. 5.7a shows the measurement, which shows good agreement with published data [Nis][Mar60].

Before measurement, spectral scan was performed around the targeted spectral line to position the monochromator. Since the discharge pulse lasts only a few milliseconds, it was not possible to operate the monochromator in scanning mode. The nitrogen emission line at 391.4 nm was used to test the optical alignment. The emission from the carbon fragments in the discharge was analyzed by characterizing the line emission at 388.1 nm.

This can correspond to emission from CH fragments, CN fragments or both [Pea62]. The use of a high resolution spectrometer and reduced broadening allow the characterization of the strong CN emission in flashFET discharges (compared to two-electrode microdischarges).

The acetone concentration was varied from 50 ppm to 1000 ppm. The emission line is seen as a pulse in the measurement. This helps to correct for dark signal in the measurement itself. Figure 5.7b, shows a typical measurement pulse for 388.1 nm emission with 100 ppm of acetone.

Figure 5.7c shows the calibration curve for the measurement. All the data for a particular concentration is gathered over a short span of time. The pulse amplitude is averaged over six discharge pulses to accommodate any possible variation in discharge energy. When using a multichannel CCD detector, the spectra are normalized to the nitrogen emission that is measured simultaneously. Since simultaneous measurement is not possible in the current configuration, the line strength is normalized to nitrogen emission lines (391.4 nm), which are measured immediately after measuring the CN emission. The normalization accounts for long-term drift in properties of the device. At a concentration of 50 ppm, the ratio of emission peaks is 4%. The ratio of emission peaks for the null measurement is 1%. The standard deviation of the measurement is less that 10%, which supports the assumption that the variation of intensity in between pulses taken in succession is small

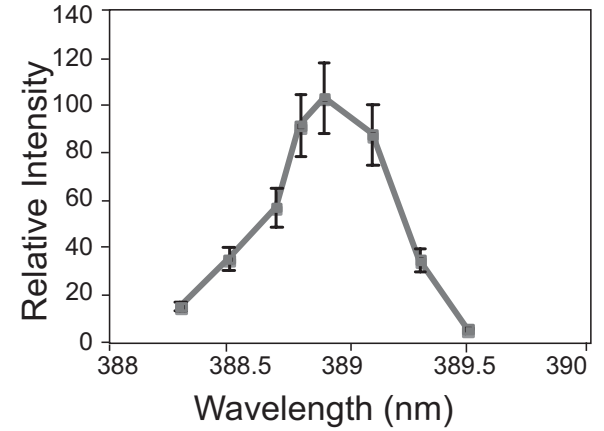

(a)

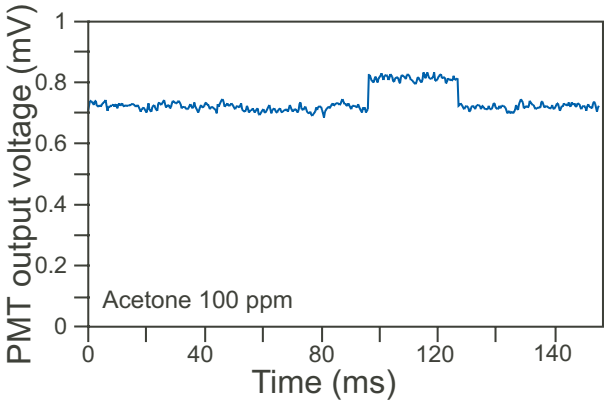

(b)

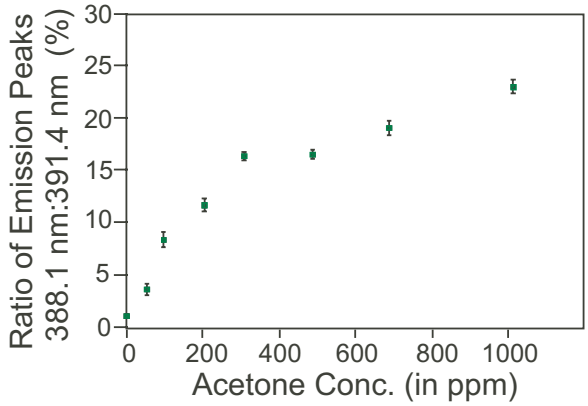

(c)

Fig. 5.7a The photomultiplier output for 388.1 nm emission from acetone fragments, at an acetone concentraton of 100 ppm. The average pulse amplitude is 0.866 mV. (b) Calibration curve, characterizing emission from the carbon fragments. The ratio of emission peaks of acetone fragments and nitrogen is plotted for a range of acetone vapor concentrations. The ratio of line intensities at 50 ppm is 3.9%. The maximum error is less than 10%. (c) Spectrum for He (388.86 nm) line to verify the spectrometer calibration.

To evaluate the longevity of the device, the device was subjected to a train of 36 μJ pulses at 1 atmosphere. The interval between pulses was 10 s. The device was inspected and cleaned with acetic acid every 50 pulses to remove any copper-oxide formed over the electrodes. (The device was sensitive to the electrode material, and the formation of copper oxide changes the secondary emission coefficient of the cathode). The device performance was steady over 550 pulses, which represents about 1.5 hours of use. The titanium underlayer was exposed at the electrode perimeter after 850 pulses, but the device continued to operate. Further investigation of the longevity of such devices may be warranted if application emerge in which their prolonged use is necessary.

5.3 Conclusions

The challenge of controlling the discharge energy for a handheld instrument is addressed by employing pulsed discharges and using a three-electrode configuration. It is seen that the three-electrode configuration reduces the power consumption by a factor of 100x to a mere 22.7 μJ/cycle. It is also seen that the optical signal has less background signal compared to pure arc discharges. A calibration curve for the sensor response was generated, and data taken with a monochromator spectrometer showed a signal/noise ratio of 4 at 50 ppm acetone concentration.

Chapter 6 Tunable Microdischarge Optical Source for Fluorescence Detection of Biomolecules[1]

Fluorescence detection is a widely used technique in medical diagnostics and biochemical analysis. Many "fluorescent molecules" emit light with characteristic wavelengths when illuminated by certain excitation wavelengths, which are shorter (and hence more energetic). In one diagnostic approach, a fluorescent dye is used to chemically label the analyte of interest. For DNA detection, dyes which intercalate into the double-helix provide very high sensitivity and make it possible to detect even attomoles of DNA base-pairs [Zhu94]. A major reason for the high sensitivity is quantum efficiency, which is the ratio of the number of photons emitted to those absorbed in the excitation wavelengths. For example, SYBR Green I gel stain is a cyanine dye that has a quantum efficiency of 0.8 [Hau96]. When bound to dsDNA it is most efficiently excited by radiation over 491-503 nm, and has a broad emission spectrum over 510-600 nm, with a peak at 522 nm. In addition to DNA, fluorescence detection using dyes can be used to ascertain the concentration of many other compounds (like glucose, ATP, RNA, proteins, oxygen, carbon dioxide) in the cellular microenvironment.

[1] The optical system in this work was designed by Dr. Long Que. The liquid microdischarge chip was designed by Dr. Chester Wilson.

While dyes offer many attractive features, their use is not always favored or even possible. Most dyes suffer photobleaching [Ros91] after many exposures and can be toxic to the cell. Hence, in many of these cases where biological activity still needs to be monitored the intrinsic fluorescence of biological molecules is used. For example NADH, which is a product in the cell metabolic cycle, can be used to monitor the metabolism of a cell [Lak92]. In addition, many proteins are fluorescent even without the presence of a dye, and changes in this intrinsic or direct fluorescence can be indicative of structural transformations [Lad00][Fas76] The intrinsic fluorescence of such proteins and peptides is due to the presence of tryptophan, tyrosine or phenylalanine, which are fluorescent amino acids. In contrast to the excitation and emission wavelengths for the SYBR green dye, which are in the visible portion of the spectrum, these three have absorption peaks over 250-290 nm and emission peaks over 280-350 nm, all in the deep ultra-violet (UV) region. The intrinsic fluorescence of tryptophan, in particular, has been widely used in studying proteins, due to its strong dependence on protein structure and dynamics. However, the quantum efficiencies of these amino acids are relatively low. For example, tryptophan, which tends to dominate in fluorescence over the other two, has a quantum efficiency of only 0.19 when dissolved in water as a free amino acid [Che72]. So to observe direct fluorescence, not only do the sources need to emit in deep-UV region of the spectrum but also provide sufficient optical power, have a small footprint to be easily integratable with microsystems.

In the recent past tremendous progress has been made in microfluidics and micro total-analysis systems. These systems, however, still rely on relatively large external light sources for fluorescence detection, due to lack of good miniature light sources.

Alternatives to optical detection, based on change in ion-concentration, impedance or mechanical properties have been implemented because of the problems with optical sources. Although these are very good for certain applications like monitoring pH, they lack the specificity of fluorescence techniques, do not provide spatial information and are restricted to a few chemical species only.

With respect to fluorescence detectors, the efforts have focused on solid-state sources such as light-emitting diodes (LEDs) and lasers (VCSELs) [Cho99] [Web01] [War99] [Thr02] [Fis04] [Kat04]. However these do not have strong emission in the blue and UV region where most of the fluorescent chemicals have their excitation spectrum. There has been some success in using AlGaN heterojunction LEDs for deep UV light [Fis04][Kat04]. Although they emit in UV region, the emission lies in a very narrow region of the spectrum and it is difficult to tune its wavelength to different fluorescent molecules. In addition, these can only be made on sapphire substrates and require sophisticated fabrication processes and equipment, and hence, are not disposable. Further, integrating them with low-cost microfluidic systems can be a significant challenge.

In this context, microdischarges are minute electrical discharges, typically generated by electrical breakdown of air across a small gap between two metal electrodes. While this term has also been used to describe small plasmas, in this work the discharges are like arcs. Although microdischarges do share some characteristics with larger scale discharges, they also have some distinguishing characteristics in the underlying physics and properties [Wil03A]. One of the appealing features is that they have promising emission characteristics in the UV region [Wil03A] [Wil03B], and can easily and

inexpensively be integrated with microfluidic systems. It has previously been reported that spectroscopy on microdischarges can be used to sense trace amounts of inorganic impurities in aqueous samples [Jen01] [Que05] [Wil02]. In such devices, the microdischarge sputters the ions from the surface of the liquid cathode into its glow region. Atomic transitions from excited ions and atoms in the microdischarge lead to emission of characteristic spectra. In this work, the microdischarge is used as a tunable optical source by using a liquid solution of predetermined composition (instead of an unknown sample), targeted to generate specific wavelengths. The microdischarge is driven by a custom built circuit which is powered by a 3 V battery, and hence suitable for portable applications. The device operates in ambient atmosphere and does not use inert gases.

6.1 Device Structure and Fabrication

A schematic of the microdischarge device is shown in Fig. 6.1. The electrical microdischarge is ignited across an air gap between a metal anode and a liquid reservoir containing a saturated salt solution, which serves as the cathode. The metal ions in the cathode are sputtered into the glow region of the discharge and emit characteristic glow. Fluid heating and vaporization are minimal under the use conditions, so [Wil03A], so thermal isolation is not required. The saturated solution is carefully chosen to cause emission in the required wavelength range.

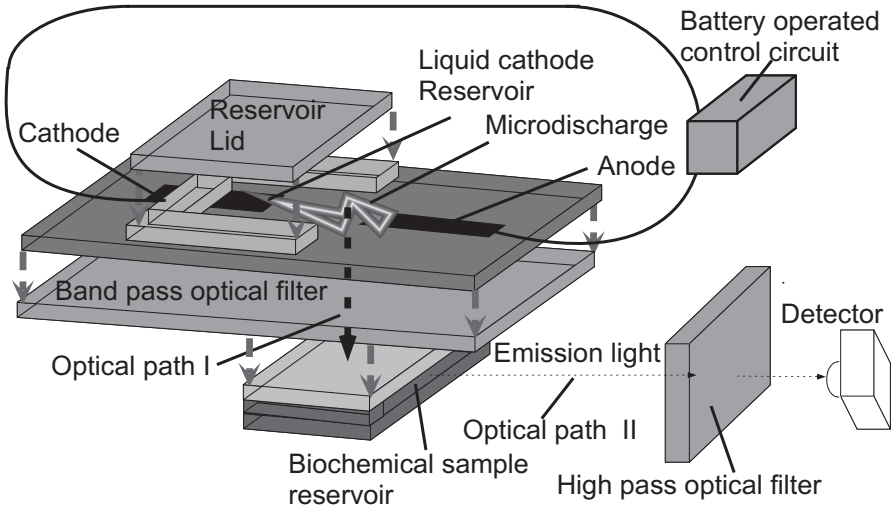

Fig. 6.1: Exploded schematic of the liquid electrode discharge spectral emission chip (LEdSpEC), which is a stacked microchip, and the associated control circuit and detector arrangement. Short arrows indicate the stacking order for the microchip whereas long arrows indicate the two orthogonal optical paths, as noted. The chip is held vertically during operation.

Unwanted wavelengths are rejected by an optical filter that separates the microdischarge from the fluorescent sample. A dichroic color filter is chosen as the integrated band pass filter due to its low sensitivity to the light incident angle and its superior lifetime and reliability over other types of filters (e.g., interference filter). The sample is located in a reservoir or channel as part of a micro-total analysis system. The filtered emission from the discharge pulse follows optical path I (Fig. 6.1), and stimulates fluorescence in the sample reservoir, which is detected along optical path II. These paths are orthogonal to minimize the signal feed-through from the arc to the detector, which is an Ocean Optics USB 2000™ spectrometer that connects to the USB port of a computer.

The stacked device was fabricated by bonding the individual glass layers using UV-curable epoxy (Lens Bond, type SK-9 optical cement from Summers optical, PA, USA) which has the same index of refraction as glass. All the glass layers were 506 μm thick,

#7740 Pyrex™ glass which has transmittance >80% for 300-700 nm wavelengths. A 4 mm wide strip of MetGlas™ foil (Magnetic Alloy 2826MB from Metglas Inc.) was used as the anode for its superior wear-resistant properties. The cathode cavity was 4 mm x 5 mm x 0.5 mm in size, and the discharge gap was 0.4 mm. The cathode contact was also a MetGlas foil placed 3 mm deep inside the cathode cavity. The optical filter was a commercial dichroic filter made on a 2.5 mm thick quartz substrate. The biochemical reservoir was 4 mm x 2.5 mm x 0.5 mm, and was bonded to the filter at the other end. The biochemical reservoir was aligned with its center in line with the discharge gap to maximize the amount of light coupling from the discharge to the biochemical reservoir. The biochemical reservoir can be much smaller and can be a part of an overall microfluidic system. Microfluidic and other kinds of lenses can also be incorporated into the light path to focus the light from the microdischarge to a point. The cathode cavity can also be part of a more complex microfluidic system having many reservoirs filled with different chemicals, connected to the cathode cavity with channels and incorporating pumps and valves to control the flow. Such a system allows real time tuning of the light output during operation. Although non-lithographic techniques have been used in its current manifestation, the device can also be made using thin film electrodes and lithographic techniques (as demonstrated in [Wil02]).

A photograph of the final fabricated device is shown in Fig. 6.2. The overall footprint of the device is approximately 10 mm x 20 mm, with the reservoirs covering half the area. The assembly is held horizontally during operation, with the detector placed vertically over the sample.

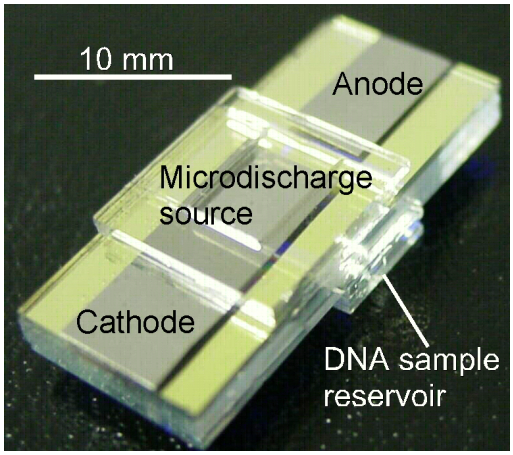

(a)

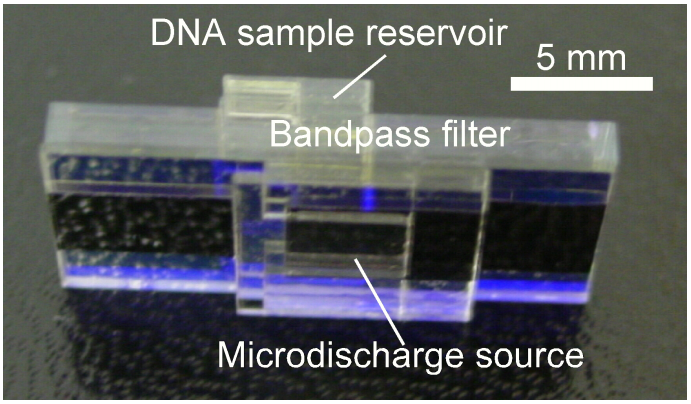

(b)

Fig. 6.2: Photographs of the fabricated chip. The device measures 10 mm x 20 mm.

The microdischarge is powered by a pulsed high voltage waveform generated from a rechargeable battery using the circuit shown in Fig. 6.3a. This particular design is based on the ringing choke converter topology [Lig55], and consists of a transistor-transformer oscillator with secondary windings on the transformer, which can boost the voltage to upto 1000 V. When the switch S1 is closed, a small base current begins to flow into the transistor. The rising collector current leads to increasing base current due to positive feedback from the transformer. This drives the transistor into saturation. In

saturation, the rate of change of current decreases, and the voltage induced in the feedback winding decreases. The base current decreases and transistor turns off. Due to the sudden decrease of collector current, a large voltage drop occurs across the primary winding, and consequently on the secondary winding. This high voltage a.c. waveform is rectified and used to charge up the discharge capacitor.

6.2 Experimental Results

For validating the circuit operation, the output voltage at various test points was observed using an oscilloscope. Figure 6.3b is an oscilloscope image of the output waveform, showing the repetitive nature of the voltage driving the microdischarge. The capacitor charges up to the breakdown voltage and discharges rapidly through the ionized media. As the output voltage drops the discharge vanishes. The capacitor charges up and the breakdown occurs again. This cycle repeats leading to a pulsed microdischarge. The breakdown voltage varies between 250-280 V. The pulse period varies between 20-30 ms due to the variation in breakdown voltage. The measured high voltage signal at the testpoint is shown in Fig. 6.3c. This signal is in accordance with the self oscillation of the circuit as described in the design section. The period of the oscillating voltage at the node marked as testpoint, is 43 μs. This signal is rectified and smoothed to charge up the discharge capacitor. The period of the pulse discharge circuit (Fig. 6.3b) depends mostly on breakdown voltage. The slope of the waveform charging the capacitor is consistent from once cycle to the next, but the breakdown voltage varies, leading to a variation in pulse period.

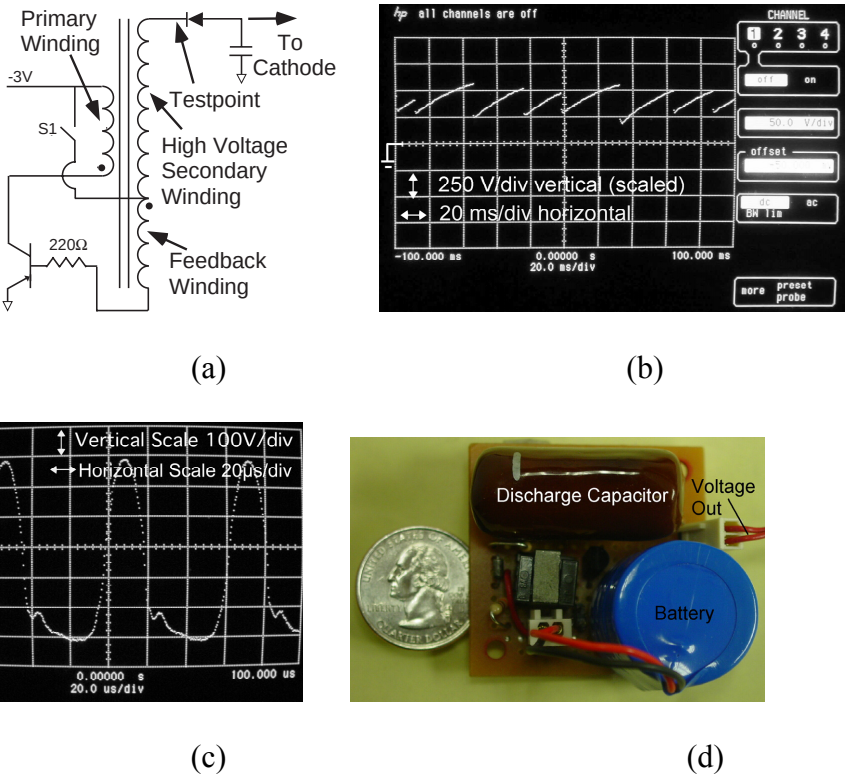

Fig. 6.3: Battery operated circuit used to create the discharge (a) Schematic of the circuit (b) Oscilloscope trace of output (cathode) waveform. The breakdown voltage varied from 240-280 V. The time period of the pulse was 20-30 ms depending on the breakdown voltage. (c) Measured waveform at the testpoint. The waveform has a frequency of 43 µs and an amplitude of 300 V. The center line represents ground in both (b) and (c). (d) Photograph of the circuit shown against a U.S. quarter.

For validating the device operation two sets of experiments were performed. In the first, a calf thymus DNA sample was labeled by SYBR green dye (Molecular Probes, Inc.), for which the absorption peaks over 491-503 nm and emission peaks over 510-600 nm. The liquid cathode used was 20% W/V $BaCl_2$. The emission spectrum of Ba provides peaks at 454 and 493nm, corresponding to 25% and 97% efficiency for this dye, respectively [Hau96].

Many intrinsic fluorophores are difficult to excite as they have low quantum efficiency, and require excitation in the deep-UV region. Tryptophan, which is a

naturally occurring amino acid, is used to evaluate the device performance in the deep-UV region. It has an absorption peak over 250-290 nm and an emission peak over 280-350 nm, with a quantum efficiency of 20%. A saturated solution of lead (II) Nitrate ($Pb(N0_3)_2$) is used as the cathode. A UV-grade filter with a fused silica substrate (#300-W-1D from Acton Research Corp, Acton, MA) is used between the optical source and the sample chamber. It has peak transmission wavelength of 293.0 nm, and its full width half maximum (FWHM) is 90.1 nm, with a peak transmittance of 47.8%.

The spectra of the microdischarge for the barium chloride doped cathode are shown in Fig. 6.4a. The 454 nm and 493 nm lines characteristic to Ba are clearly seen. In the unfiltered spectrum, a number of lines characteristic to nitrogen and other atmospheric gases are also observed. The unwanted wavelengths were eliminated by the bandpass filter (350 – 500 nm). Figure 6.4b, shows the filtered spectrum. The two primary Ba lines pass through the filter, exciting the dye labeled DNA, inducing fluorescence. This fluorescence is additionally filtered by a high pass (>500 nm) optical filter, to reduce noise, before being imaged. The measured fluorescence image of the DNA excited by the battery-driven, on-chip source is shown in Fig. 6.5a. The reference image, in the absence of dye, (Fig. 6.5b) shows no illumination. Fig 6.5c shows the image of the fluorescent DNA dye using a commercial 100 W mercury UV arc lamp (Osram HBO W/2) source for excitation. It is noteworthy that the measured fluorescence using the pulsed microdischarge optical source has the same quality as the commercial UV-light source.

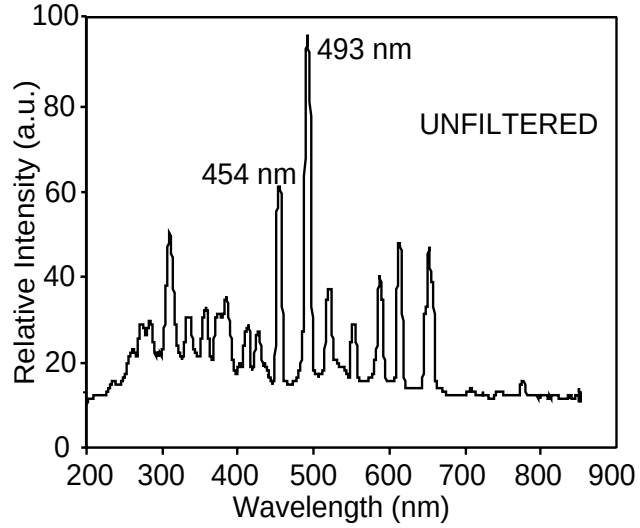

(a)

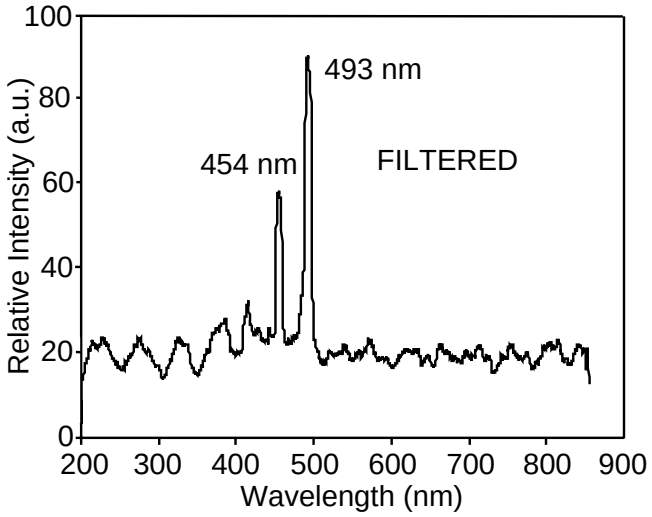

(b)

Fig. 6.4: Spectrum of the microdischarge source: (a) With 20% $BaCl_2$ solution as cathode, showing the 454 nm and 493 nm barium lines. (b) Spectrum of light after the on-chip optical filter, with all unwanted lines suppressed.

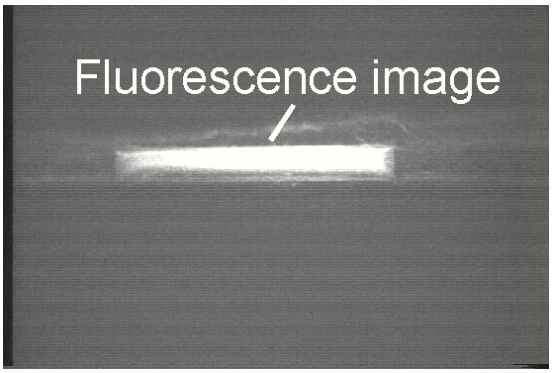

(a)

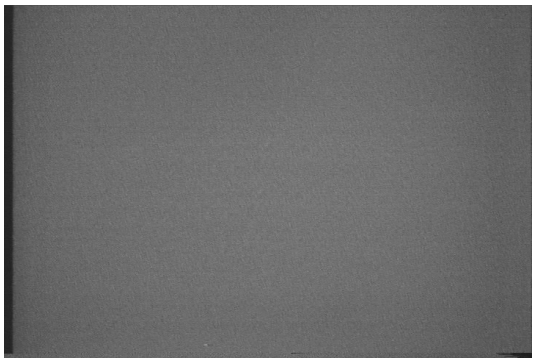

(b)

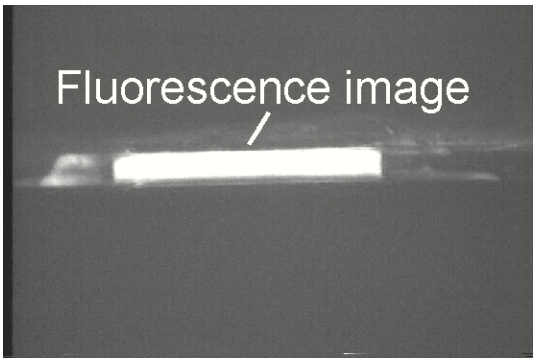

(c)

Fig. 6.5(a): Photograph of the fluorescence image of SYBR green tagged DNA, using the microdischarge source as the excitation. (b) Reference image with water instead of tagged DNA, showing no fluorescence. (c) Photograph of fluorescence image of SYBR green tagged DNA using a commercial UV lamp source (100 W mercury arc lamp).

In the second series of validation experiments L-tryptophan was used as the sample to be detected. Unlike the SYBR green tagged DNA, tryptophan has a very weak intrinsic fluorescence and requires deep UV light for excitation. This makes it particularly hard to excite, especially in microsystems. Since the working wavelengths are in UV, a spectrometer is used instead of a microscope as a detector. The filtered spectral emission obtained by a micro-discharge to the saturated $Pb(NO_3)_2$ solution used to excite the fluorescent sample is shown in Fig. 6.6a. There is a substantial peak near 280 nm, which is characteristic of Pb, and closely matches the excitation peak for tryptophan. Despite the optical filtering, there are a number of other peaks with high relative strength, particularly in the 300-350 nm emission range of tryptophan, which can interfere with the fluorescence signal. (The filter has a transmittance of 10% even at 400 nm, which lets many of these lines through). This problem was overcome by using special techniques as outlined below.

The fluorescence sample was prepared by dissolving commercially available tryptophan in DI water at room temperature till a saturated solution was obtained. In all the measurements presented, the background radiation in the room was measured immediately before each experiment.

The absorption of the UV light was studied by placing the optical fiber on the same axis as the incident light source (i.e. along optical path I). Figure 6.6b shows the light spectrum after it passes through a 2.5 mm deep sample of tryptophan solution. We can see that tryptophan absorbs the lines in the 250-300 nm range, as reported in literature. To verify this result, a control experiment was done by placing water instead of tryptophan in the sample chamber. The lines in the 250-300 nm range pass through the

water and can be clearly seen in the transmitted spectrum. This confirms that the tryptophan sample absorbs the light in the 250-300nm range from the microdischarge source.

The fluorescence spectrum was observed by placing the fiber along optical path II, transverse to the excitation path to remove the interfering background radiation. Figure 6.7a shows the observed output from a tryptophan sample, with evidence of the characteristic broad peak between 300 nm and 450 nm. A control experiment with water in place of tryptophan provides the spectrum shown in Fig. 6.7b, with no evidence of the characteristic broad peak of tryptophan. The peaks near 368 and 405 nm are from spikes of high relative intensity in the lead nitrate spectrum which are not sufficiently attenuated by the filter and are coupled from optical path I to II. The curves in Figures 6.7a and 6.7b were both obtained by integrating the spectrum for 10 s.

A simple calibration method in which the spectrum of the water sample is subtracted from that obtained with the tryptophan sample can be used to make the fluorescence emission clearer. However, before doing this, the data in Figs. 6.7a and 6.7b are scaled so that the base-to-peak amplitude at 405 nm is of equal magnitude in the two spectra. It is noteworthy that this calibration at 405 nm also removes all the other lines from the signal feed-through. Averaging over $\pm$15 wavelengths using triangular weighted averaging is used to reduce the random noise in the spectra.

Figure 6.7c shows the observed tryptophan spectrum after the signal processing, superimposed with the reference tryptophan spectrum (from [Che72]). The characteristic broad peak of tryptophan fluorescence is clear. This establishes that the microdischarge UV source can be used to excite the UV fluorescence.

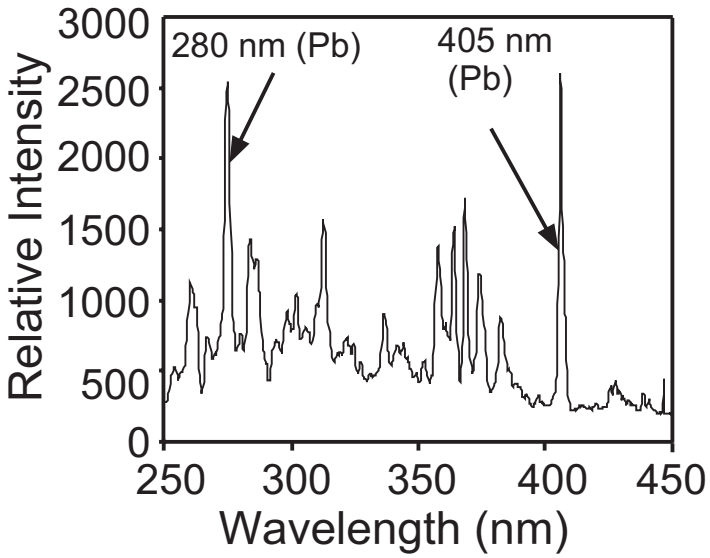

(a)

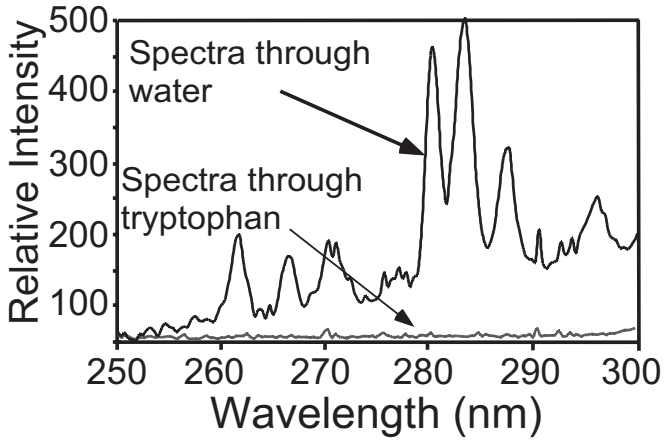

(b)

Fig. 6.6(a): Filtered spectrum of the microdischarge source, with saturated (5g/10ml) $Pb(NO_3)_2$ solution as cathode, showing strong 280 nm Pb lines. This emission is used to excite the fluorescence of the tryptophan sample (b) Light transmitted through tryptophan shows that the peaks near 280 nm have been absorbed. These wavelengths are transmitted through the control sample of water.

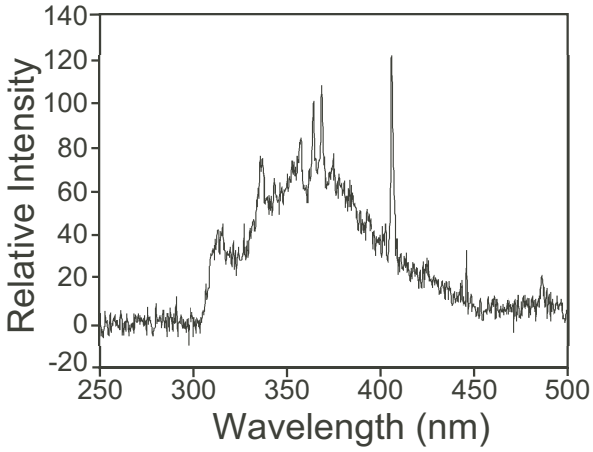

(a)

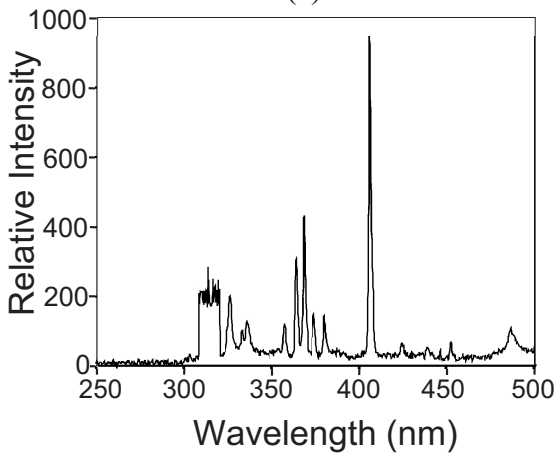

(b)

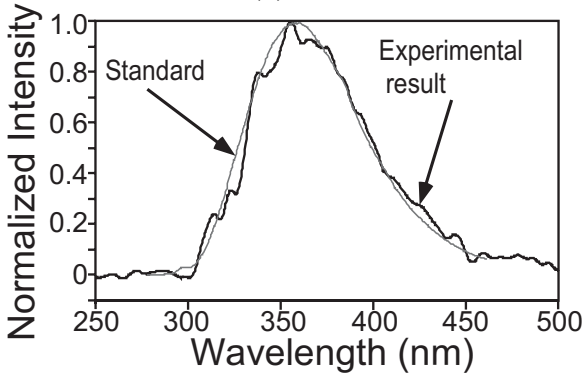

(c)

Fig. 6.7(a): Optical emission measured along optical path II (as shown in Fig. 6.1) indicating the existence of the direct fluorescence of tryptophan by the broad peak between 325 nm and 425 nm (b): Spectrum measured with a DI water control sample in a manner analogous to Fig. 6.7a, shows the absence of the broad peak between 325 nm and 425 nm. (c) The net output from the tryptophan sample, obtained by subtracting the curve of Fig.6.7a from that of Fig. 6.7b scaled to the 405 nm peak of the spectrum in Fig. 6.7a. A 30-point triangular averaging was performed to reduce the noise. The reference emission curve of tryptophan from the National Bureau of Standards [Che72] is superimposed.

6.3 Conclusion

This effort successfully demonstrated that a microfluidic chip with an integrated microdischarge source can be used to locally generate fluorescence in biochemicals. The discharges are generated in ambient air, between a metal anode and a liquid cathode, both of which are on-chip. Fluorescence of SYBR dyed calf thymus DNA is found to clearly occur, using $BaCl_2$ solution as the cathode. As the signal quality of this fluorescence is found comparable to that of a commercial system, this device can be used for a variety of biomedical diagnostic applications**.** The characteristic fluorescence of tryptophan in a solution of water is observed using a lead nitrate solution as the source of 280 nm radiation used for the optical excitation of the sample. This clearly establishes the effectiveness of a microdischarge source in the deep-UV region. Since the spectral characteristics of the optical source are dependent on the spectra of metal ions in the liquid cathode, this device can be easily tuned to a variety of biological fluorescences, both extrinsic and intrinsic.

One can envision a microfluidic system in which the sample reservoir for the biochemical is part of a larger microfluidic system. Further, the reservoir for the liquid cathode can also be part of a separate fluidic system, by which the contents of the cathode can be dynamically controlled or tuned.

Chapter 7 Handheld Microdischarge Spectroscopy System

Microdischarge-based sensors are spectral sensors that detect chemicals based on their atomic structure rather than their chemical properties. Discharge spectroscopy in the form of inductively coupled plasma atomic emission spectroscopy (ICPAES) is one of the most sensitive techniques used in laboratories by chemists [Spa00] and is commonly used with GC systems. Many groups (including ours) have miniaturized microplasmas to chip scale for chemical sensing and other applications [Eva03].

One of the very attractive features of chemical sensing by emission spectroscopy is that it works for liquid and gas phase species. In previous work we have demonstrated low power microdischarge gas/vapor sensors, and liquid electrode devices for the detection of trace elements in water samples [Que05][Wil02]. In this work, we bring these ideas together in the form of a handheld system, for the analysis of chemicals using pulsed microdischarges[2]. The system employs disposable gas and liquid discharge microchips (GDM and LDM, respectively) with a common interface. The LDM uses the same basic principle of using a liquid cathode as described in [Wil02] and [Que05], using a porous cathode, instead of a microfluidic channel for sample delivery. This design

[2] Portions of this work have been presented in [MitB06]. The circuit was developed by Brandon Levey. Chip holder and optics design and systems integration was done by T.-C. (Richard) Fung.

permits controlled uptake of small volumes of the liquid sample and can be used to detect very low concentrations of metallic impurities in water samples. Both chips use atmospheric pressure pulsed microdischarges and avoid the use of a pre-concentrator to eliminate pumping demands.

7.1 Design

7.1.1 System Design

The handheld system (Fig. 7.1) includes a sensor chip-holder, a pager-sized spectrometer (USB 2000 from Ocean Optics), a PDA (HP IPAQ HX 2000 Pocket PC), and a battery operated control circuit and power management unit. The sensor chip-holder can accommodate both liquid and gas microdischarge chips, which can be easily swapped in and out. This is implemented by mounting the chips on a PCB and making contact to it by spring loaded contacts in the customized chip holder unit, which is made from Noryl™ plastic (G.E. Plastics). The sensor chip holder also has a strategically placed collimating lens (Ocean Optics, UV-74, with a diameter of 5 mm, a focal length of 10 mm, and fused silica construction for 200-2000 nm wavelength) for coupling the microdischarge emission to an optical fiber (which connects to a spectrum eter). This arrangement provides easy optical alignment and maximum light transfer to the optical fiber.

A custom circuit provides the necessary pulses for the discharge and the data acquisition so that the spectroscopic data is captured and transferred to the wireless-enabled handheld computer (PDA) at each discharge event. The control circuit is designed to achieve accurate timing of low and high voltage pulses for creating the discharge and synchronizing the optical sampling with controlled delay and duration. The system is powered by two rechargeable 3.6 V Li-ion batteries. These batteries were

selected for their long lifetime and ability to provide high current. The unregulated voltage from the battery is sent to two regulators, so that circuit supply voltage remains constant for battery voltages ranging from 6.5-8.4 V. A 5 V linear regulator (LP 8345 from National Semiconductors), powers the complex programmable logic device (CPLD) and the spectrometer. A linear regulator was chosen (even though it is not power efficient), because the spectrometer requires a low-noise power supply for accurate data acquisition. A second DC-DC converter (MAX1771 from Maxim) generates a 12V output, with up to 500 mA current, that will be provided to yet another DC-DC converter (described later) for generating the higher voltages required for initiating discharge. The 12V output can be changed by adjusting a potentiometer. Since the high-voltage section requires significant current, and power supply noise is not significant, this approach provides overall power efficiency.

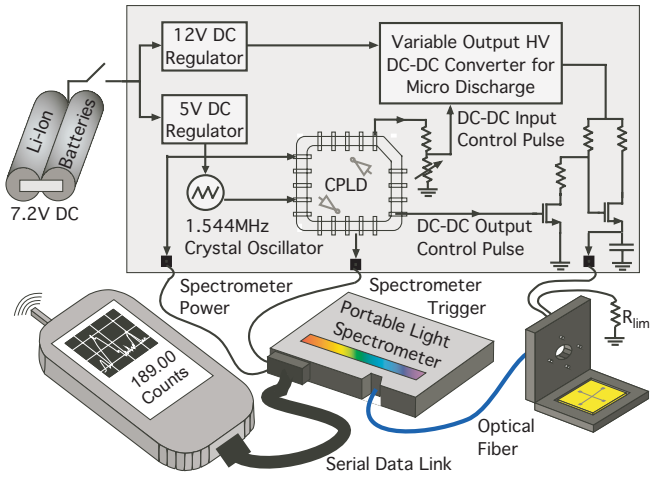

Fig. 7.1: Schematic of the handheld system. The chip is placed in the chip holder and the discharge is struck using the control circuit. The spectrometer captures the optical signal and transfers the data to a wireless enabled PDA on a serial link. Inset: The controller circuit.

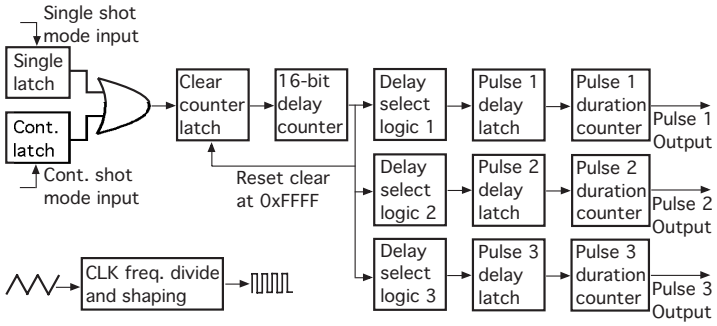

Fig. 7.2: Simplified schematic of the digital control circuit. The clock divider-shaper provides the software controlled clock. The 16-bit delay counter is initialized at start. Each output pulse has its own delay select logic, which determines when the next stage is triggered. Once triggered the pulse goes high for a set duration of clock cycles determined by the program.

A 1.544 MHz crystal oscillator provides the reference clock for the digital circuit. The actual clock is stepped down in frequency from the reference clock by using ripple counters. This is done to allow software control of the operating frequency, and hence the minimum and maximum pulse timings.

Dedicated hardware control of the discharge and sampling trigger pulses is necessary because accurate triggering requires low jitter in the pulses. Programmability is essential as the timing requirements can vary depending upon the application. The use of a CPLD (Atmel ATF1508AS) for digital logic provides both. The system is designed to have three output pulses, which can start at and last for separately programmed clock cycles. While independent, they use the same clock for synchronization. The start time of each pulse is hard-programmed into the CPLD but the pulse durations can be modified using a series of DIP-switches outside the CPLD. The CPLD is operated at a frequency of 24.125 KHz, which corresponds to a pulse accuracy of 45.451 μs.

The digital logic for the CPLD (Fig. 7.2) is comprised of three stages: the first stage controls the initiation of the pulse set, the second stage controls the pulse delays,

and the third stage controls the pulse durations. The first stage allows for two modes of operation: a single shot mode where a single set of microdischarge pulses are generated and a continuous mode where the device operates at a programmed rate. In the event that both modes are activated by the user, the continuous mode is given precedence.

The second stage of the digital logic consists of a 16-bit ripple carry counter. This counter is designed to output all logical zeros using an active low signal to indicate a "clear". Once the single or continuous mode is chosen, the counter begins to count from 0x0000 to 0xFFFF. Different logic conditions are chosen to control the individual delay of each pulse. For example, the programmer can choose to have one pulse start when the counter output is 0x0001, another at 0x0020, and another at 0x0300 (1, 32, and 768 clock cycles from the start respectively); three completely independent times. Once the counter reaches 0xFFFF a signal is sent back to the first stage to communicate that one full output cycle had been completed. In single shot mode the counter resets to an output of 0x0000 and if it was in continuous shot mode it resets and begin counting again from 0x0000 to 0xFFFF with the same delays as before.

The third stage of the digital logic consists of three identical sections containing a 14-bit ripple carry counter and pulse control circuitry. At the input of this stage is a 16-input AND gate outputs a logical 1 for one clock cycle when the programmed delay is completed, and triggers the pulse output. On receiving the trigger, the 14-bit ripple carry counter begins counting from 0x0000 to the programmed pulse duration. This programming can be provided internal hardware or external DIP-switches. (Either active-low or active-high signaling can be selected.)

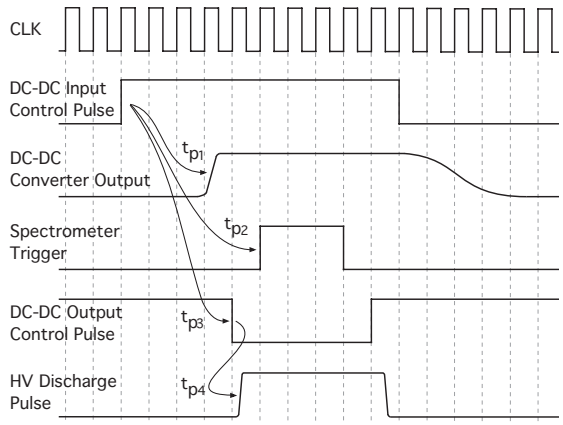

(a)

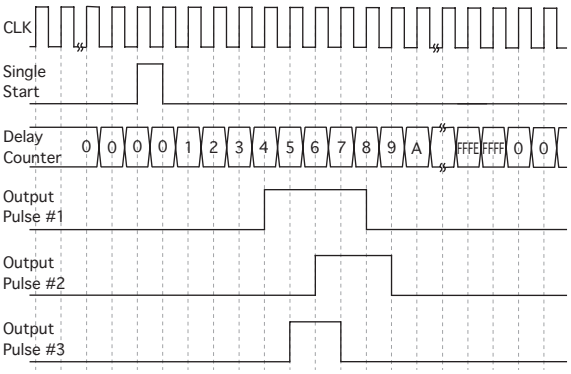

(b)

Fig. 7.3(a): The operating cycle of the system. The discharge pulse is controlled control signals to the input and output of the DC-DC converter. The timing is accurate to 50 μs. (b) Timing diagram showing the internal signals. Once the signal for a single-shot microdischarge is received, the delay counter starts counting. The output pulses have separate delays and durations but work from the same initial signal.

Figure 7.3a shows the overall timing scheme for the system, whereas Fig. 7.3b shows the timing details for the digital logic. In stages 1 and 3, all latching occurs on a rising clock edge while the counter in stage 2 is latched at a falling clock edge. This is needed since internal gate delays can cause latching to occur between stages when valid signals are not ready at the output. By latching on alternating clock edges it essentially gives the

signal an extra half period, around 23 μs, to become valid. (The internal gate delays of the CPLD are 50 ns, so this is not an issue.)

In order to prevent the inadvertent triggering of a pulse from power-up conditions, an RC combination is used to provide a 5 ms ramp to a reset input in the CPLD.

The outputs from the CPLD are used to trigger the high-voltage section of the circuitry and the spectrometer. The high-voltage DC-DC converter (HVP2P from Pico Electronics) which powers the microdischarge, generates 250-2000 V from the 12 V input previously described. The output voltage is controlled by a proportional input, which has a linearity error of <1 %. For example, 2.5 V at this input corresponds to an output voltage of 1000 V, whereas a 5 V input corresponds to an output voltage of 2000 V. The output voltage is designed fall to 0 V when the programmable input falls below 0.25 V. To trigger the output pulse, the 5 V trigger signal from the CPLD is sent through a voltage divider and then into the programmable input. In this design the input would be at 0 V for a period of time, then the trigger pulse would move this input to a designed voltage for the desired output voltage, and then back to 0 V.

The output of the DC-DC converter can be optionally controlled by a shunt-series switch. Since the DC-DC converter has a finite rise and fall time, applications in which faster transitions are required would benefit from this approach. The signal from the high-voltage converter is fed into a high speed MOSFET-controlled switching circuit that uses 2 transistors as shown in (Fig. 7.1). These MOSFETs (STP3NB100 from ST Microelectronics) allowed for a maximum V_{DS} of 1000 V with a V_{GS} of only 5 V, and have an "on" resistance of <6 Ω. A 0 V output control pulse on the gate of the shunt transistor permits the discharge electrode to receive power, whereas a 5 V gate bias on

the same line activates the shunt to ground. The timing for this was illustrated in Fig. 7.3a.

This system permitted the control of the spectrometer and high voltage outputs individually to an accuracy of <50 μs, with pulse durations from 50 μs to just under 1 second. It is notable that the accuracy and the maximum pulse periods are both determined by the clock speed, and the use of a software-controlled clock allows one to trade-off one for the other. An accuracy of 10 ns in timing is possible just by programming the CPLD accordingly. However, in such a case the maximum pulse duration can only be 0.5 ms due to the interdependent nature of these two variables.

7.1.2 Microdischarge Devices

The GDM (Fig. 7.4a) employs a two-electrode hybrid arc-plasma microdischarge struck between two copper electrodes. The highly energetic electrons in the plasma cause the organic vapors to disintegrate into smaller fragments, including many mono and diatomic fragments, which have characteristic emission in the UV-visible wavelengths.

In the LDM (Fig. 7.4b) a microdischarge is struck between a metal anode and a porous glass cathode. The porous cathode is wetted by the conductive aqueous sample, which is added through a side port in the chip. When plasma is struck between the metal impurities in the wet electrode are sputtered into the discharge and undergo atomic transitions in the plasma, which have characteristic line spectra in the plasma glow. The porous cathode allows for controlled uptake of the liquid sample, which eliminates splashing of the liquid, which increases device reliability at smaller anode-cathode (A-K) gaps. The smaller A-K gaps also enable the use of atmospheric pressure microplasmas rather than arcs. It is notable that microplasmas are driven, to a large extent, by secondary emission from the

cathode so the use of the cathode as a means of sample delivery results in a very sensitive device. While the concept of discharge-based detection of inorganic impurities in water was described in [Wil02], that effort used a liquid microchannel for the cathode rather than a porous cathode. The porous cathode provides the benefit of wicking the aqueous sample for delivery from a side port to the discharge region, and as discussed in section 7.3, it offers some other advantages as well.

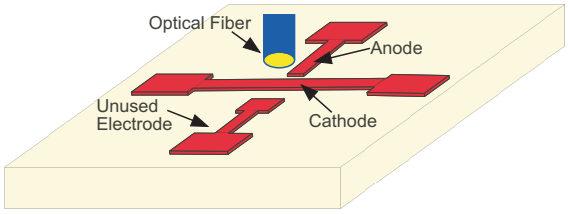

(a)

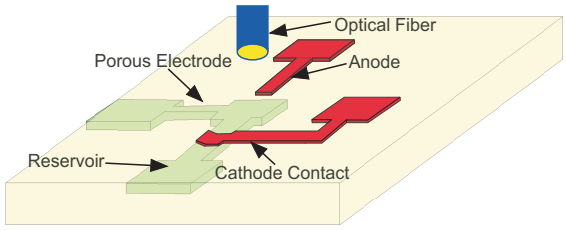

(b)

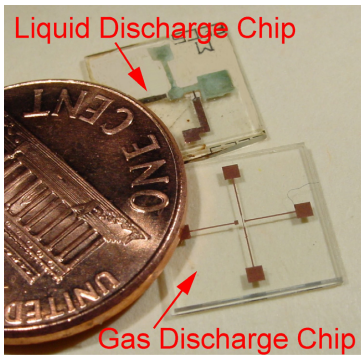

(c)

Fig. 7.4 (a): Schematic of the gas microdischarge chip. (b) The liquid microdischarge chip. (c) Photograph of the liquid and gas microdischarge chips shown against a US penny.

7.2 Fabrication

Both the GDM and the LDM use electroplated copper electrodes on a glass substrate. For the GDM, a blanket Ti/Cu (50 nm/100 nm) sputtered deposition acts as the base layer. A layer of photoresist (Clariant, AZ9260) is used to define a 50 µm thick mold for the plating. A layer of copper, 25 µm thick, is then electroplated through the mold to define the electrodes. The photoresist and the base layers are then etched away to leave the electrode structure intact.

The LDM fabrication (Fig. 7.5) begins with a glass-etch to define a recess for the porous cathode. A layer of Cr/Au (50 nm/500 nm) is used as the etch mask. Then the copper electrodes are electroplated, as in a GDM, to form the anode and cathode contact respectively. Finally the porous cathode is fabricated by filling channels with glass frit slurry in acetone (0.2 g/ml), followed by sintering in a furnace at 460ºC for 20 mins. A layer of oxide is formed over the electroplated copper during sintering. The oxide layer is removed by etching it in acetic acid at 45 ºC for 30 minutes.

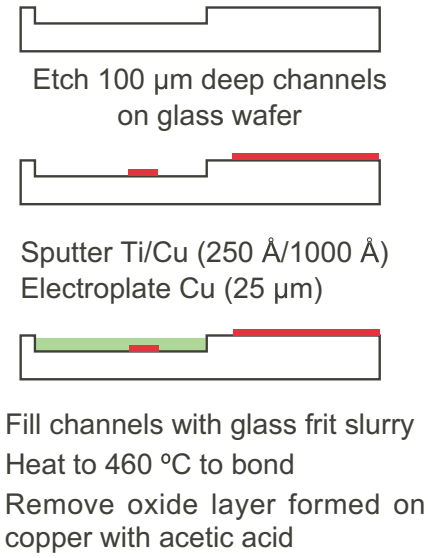

Fig. 7.5: Process for the fabrication of the liquid microdischarge chip. The fabrication for the gas discharge microchip involves only step 2.

7.3 Experimental Results

The handheld system and its components are shown in Fig. 7.6. The overall dimensions of the system are approximately 19x13x5 cm^3, but there is substantial room for further miniaturization. The handheld spectrometer, with a range of 200-850 nm in wavelength is approximately 9x6x3 cm^3, and the chip holder is 4x4x2 cm^3. Figure 7.4c shows a picture of the fabricated LDM and GDM chips against a US dime. The active area of the LDM is 1x1mm^2 with an A-K gap of 50 μm. The GDM has an active area of 500x500 μm^2 and an A-K gap of 50 μm.

A standard pulse of amplitude 850 V and duration 4 ms was used for all testing. A 10 KΩ resistor is ballast resistor was connected to ground to regulate the discharge.

For evaluating the LDM, a standard containing 2 ppm Cr in an aqueous solution that also had 5% HNO_3 was used. This was a 2 μl: 10 ml mixture of 10000 ppm plasma standard Cr in 5% HNO_3 (Specpure^{TM}) and 5% HNO_3. A 1 μL sample was loaded through the side port, which was wicked to the discharge site through the porous electrode material. The sample was loaded only once to avoid pre-concentration effects. Figure 7.7 shows the captured spectrum, having emission from the 425 nm Cr line which is missing from the control sample of 5% HNO_3. The sensitivity of the chip can be further increased by using pre-concentration. In such a mode the sample is loaded and let dry. If done repeatedly the metal salt accumulates in the cathode and hence gives a stronger signal. Another consequence of pre-concentration is that the pH gradually increases due to acid accumulation. It is well known that the microdischarge device shows better performance at lower pH [Wil02], so this helps getting better sensitivity without using a highly acidic sample.

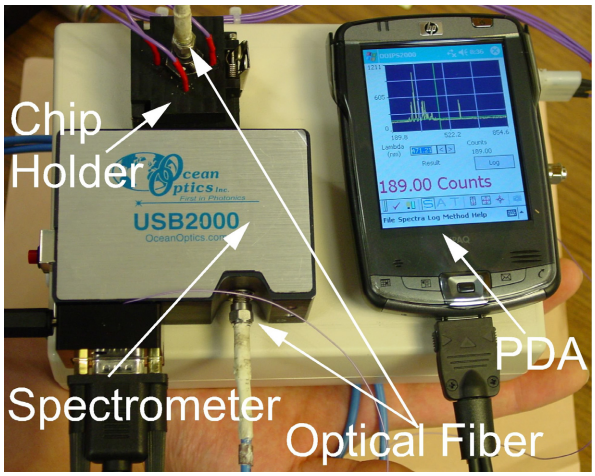

(a)

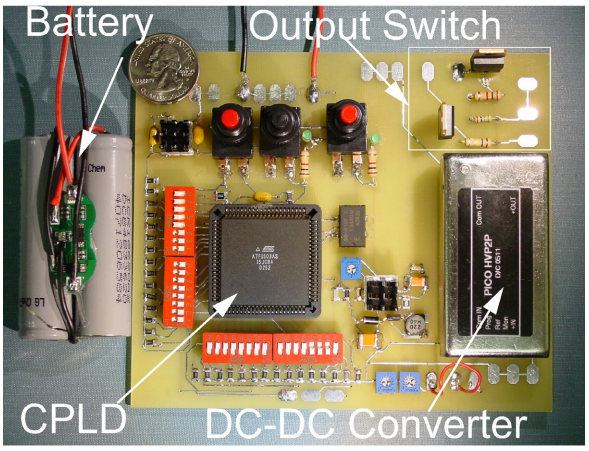

(b)

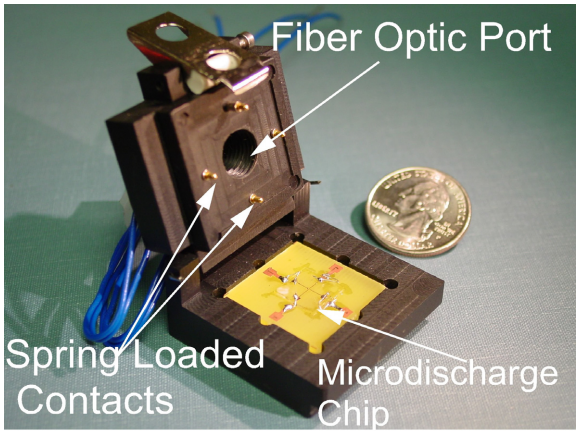

(c)

Fig.7.6 (a): Photograph of the handheld system showing the controller, the chip holder and the PDA. (b) Photograph of the controller circuit. (c) Photograph of the chip holder shown against a US quarter. Contact to the terminals is made mechanically by a spring loaded, gold plated pin. A lens is placed in the middle, aligned with the active area.

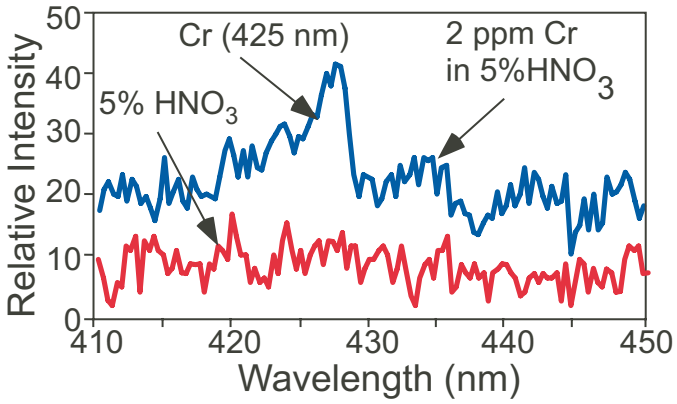

Fig. 7.7: Spectra from the liquid spectroscopy microchip (obtained without pre-concentration). A 425 nm line due to chromium (top) is clearly seen. The control sample (bottom) shows no emission at that wavelength.

The measurements suggest that the sensitivity of the LDM is slightly higher compared to devices employing a liquid cathode [Wil02], which could detect about 10 ppm of Cr. The use of a porous cathode is also attractive because it eliminates the motion of the liquid and the potential for spill-over at the cathode site (which improves reliability) and improves the consistency of data across pulses by a much better controlled injection of the liquid sample into the discharge glow. The spectrum also shows a strong 325 nm line emission (not shown in figure) from the copper in the anode material and glass frit (as copper oxide additive).

For evaluation of the GDM, the chip holder was placed in a controlled vapor environment (along with a commercial reference sensor) where the concentration of acetone was maintained at 13 ppm. Figure 7.8 shows the spectra in acetone and air ambient. The 386 nm line is present in acetone but absent in air.

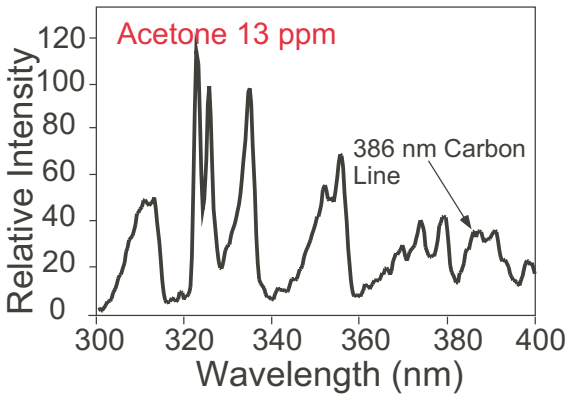

(a)

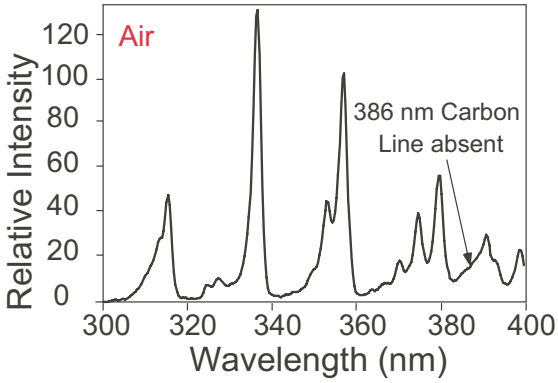

(b)

Fig. 7.8: Spectra from the gas discharge microchip (without pre-concentration). (a) In 13 ppm acetone showing the presence of 386 nm carbon line. (b) Control experiment in air. The 386 nm line is absent.

7.4 Conclusion

Sensors based on microdischarge spectroscopy are promising because they can detect a wide range of chemicals almost instantaneously. This work demonstrates the possibility of a handheld microdischarge based chemical analysis system for sensing in gaseous and liquid environments. The system employs swappable gas and liquid microdischarge chips and a chip holder that interfaces to both providing a low impedance

contact and automatic optical alignment to the discharge. The microdischarges operate at atmosphere in air ambient, eliminating the need for a pump or special gases for the analysis. The gas discharge microchip can detect 13 ppm of acetone vapor in air ambient. The liquid discharge microchip demonstrates the first use of a wet porous cathode. The porous cathode introduces controlled amount of sample by wicking in liquid through the pores, while still providing a low impedance to the cathode contact. This eliminates splashing of the liquid, and increases device reliability and sensitivity over discharges, which employ a liquid electrode. Using this chip and the handheld system the detection of 2 ppm of Cr was demonstrated.

Chapter 8 Conclusions and Future Work

As a consequence of this work, there are a number of conclusions that can be drawn regarding the characteristics and utility of DC-powered microdischarges from planar electrodes.

At atmospheric pressures, these discharges operate in three different regimes. Spark discharges occur when electrode gaps are greater than 200 μm and the cathode is made of high work function material like titanium. These discharges are very bright and are characterized by large intensity of continuum wideband radiation. It was also found that they have an afterglow lasting for 10-12 ms in which the line spectra is seen to decay faster than the continuum emission. It was shown that afterglow spectroscopy can be used to capture the continuum spectra separately and subtract the continuum emission in real time. It was shown that for electrode gaps between 50μm – 100μm, and appropriate values of circuit elements, microscale discharges at atmospheric pressure can occur as glow discharges, arc discharges or as a combination of the two in the form of arc-glow hybrids. The presence of a stable intermediate between arcs and glows is a feature of microdischarges. Micro-arcs have a wide spectral distribution in emission, while microglow discharges have strong but narrow band emission mainly in the UV-blue region, when using air as the carrier gas. The micro-arc is driven by bursts of current while a steady but small current drives the microglow discharge. The glow discharge

current can be controlled by the limiting resistor and the overvoltage, while the arc component is can be controlled by the limiting resistor. Using these it is possible to adjust the spectral output to desired levels. The reason for the intermittent pulsing was attributed to cathode spot formation. The reasons for the formation of these are not well understood and should be the subjected of continuing investigation. The use of a flowing gas can be used to stabilize the discharge. The relationship between gas flow and plasma density and electron temperature needs to be investigated, so flow can be used as a parameter in tuning these discharges.

The application of these discharges to chemical sensing was demonstrated by the measured response curve for sensor output for concentrations acetone concentrations ranging from 50 ppm – 1000 ppm.. The 388.6 nm CN line was used as a benchmark and 394.1 nm emission from N_2^+ is used as a normalization. It was shown that the device can distinguish 17 ppm of acetone in air ambient in a 65 ms detection time, without using any pre-concentration.

The challenge of controlling the discharge energy for a handheld instrument was addressed by employing pulsed discharges and using a three-electrode configuration. It was seen that the three electrode configuration reduces the power consumption by a factor of 100x to a mere 22.7 μJ/cycle. It is also seen that the optical signal has less background signal compared to pure arc discharges. A calibration curve for the sensor response was generated, and data taken with a monochromator spectrometer showed the signal/noise ratio of 4 at 50 ppm acetone concentration.

It was demonstrated that a microfluidic chip with an integrated microdischarge source can be used to locally generate fluorescence in biochemicals. Since the spectral

characteristics of the optical source are dependent on the spectra of metal ions in the liquid cathode, this device can be easily tuned to a variety of biological fluorescences, both extrinsic and intrinsic. This feature is not available in solid-state optical sources. The discharges are generated in ambient air, between a metal anode and a liquid cathode, both of which are on-chip. Fluorescence of SYBR dyed calf thymus DNA is found to clearly occur, using $BaCl_2$ solution as the cathode. This device concept, can be used for a variety of biomedical diagnostic applications**.** The characteristic fluorescence of tryptophan in a solution of water is observed using a lead nitrate solution as the source of 280 nm radiation used for the optical excitation of the sample. This clearly establishes the effectiveness of a microdischarge source in the deep-UV region.

A handheld system for chemical sensing using two electrode discharges was demonstrated. The system employs swappable gas and liquid microdischarge chips and a chip holder that interfaces to both providing a low impedance contact and automatic optical alignment to the discharge. The microdischarges operate at atmosphere in air ambient, eliminating the need for a pump or special gases for the analysis. The gas discharge microchip can detect 17 ppm of acetone vapor in air ambient. The liquid discharge microchip demonstrates the first use of a wet porous cathode. The porous cathode introduces controlled amount of sample by wicking in liquid through the pores, while still providing a low impedance to the cathode contact. This eliminates splashing of the liquid, and increases device reliability and sensitivity over discharges, which employ a liquid electrode. Using this chip and the handheld system the detection of 2 ppm of Cr was demonstrated.

While several challenges in the use of microdischarge sensors for handheld systems for chemical agent detection have been addressed in this thesis, challenges still remain. The interference by nitrogen is one of the biggest issues. It has to be addressed by a number of techniques. Preliminary work done by Scott Wright [Wri07] has demonstrated that micro-sputter ion pumps can be used to getter nitrogen in a sealed cavity. In this approach, the device is packaged in an inert ambient, and a small quantity of gas is sampled in. The nitrogen and oxygen signals are suppressed by the sputter ion pump and the device is more sensitive. Other approaches like population modulation spectroscopy need to be integrated. In this technique, a modulating AC voltage is superposed on the breakdown pulse. The optical emission corresponding to species created during the discharge (as compared to those in the ambient like nitrogen) is modulated at twice the frequency of the applied AC [Dav95]. This can be used to get a cleaner signal in a noisy spectral environment.

The chemistry of the microdischarge devices needs to be studied further. How different chemicals are fractionated in the discharge and their relationship with the discharge energy needs to be explored by coupling the microdischarge device to a mass spectrometer.

Appendix A Atomic and Molecular Spectroscopy

A detailed understanding is required to interpret the spectra. Emission spectra from atoms and molecules contain a lot of overlap, especially when using a low resolution spectrometer. Because of this it is, it is up to the experimenter to ascertain which emissions are likely to dominate and interpret the spectra accordingly. This chapter provides a review of the physics of the atomic and molecular emission, the conventions of spectroscopy and a description selection rules and other laws governing the intensity of emission lines. The notation and development follows the text outlined in [Joh99]. For a deeper description, the reader is referred to [Joh99] and [Her50].

A.1 Atomic Spectra

A spectral line is a curve showing intensity distribution as a function of wavelength or frequency. A spectral line corresponds to the energy difference between two atomic or molecular states. In thr 1880's Rydberg derived a formula for spectral series, showing that they could be written as difference of two 'terms'. This concept was refined by Ritz and is usally stated as *Ritz combination principle:* "Every spectral line represents the energy difference between two energy levels in an atomic or molecular system, and from the knowledge of spectral lines, the relative energy levels of a system can be derived."

Since only energy differences are measured, the zero can be placed anywhere. In atomic theory, the energy of the system is defined as zero when the electron is at infinite distance from the nucleus. The bound states have negative energy. The numerical value of energy on this scale is known as the term value. Experimentally, however, energy levels are measured through energy of spectral lines, which in usual cases involve transitions to or from the ground states. Ths ionization is hardly observed in spectroscopy. The energy level structure is thus derived relative to the ground state, not the ionized state.

A.1.1 Atomic Theory

The idea that an atom or molecule or atom exists in discrete states (stationary states) having a definite energy was first suggested by Neils Bohr. However, models based on quantum mechanics are much more accurate and a brief review is presented here. The simplest atomic system is the One-electron atom system (H, He^{+}, Li^{2+}).

A.1.1.1 One-electron systems

The origin of the system is chosen to be the nucleus. The motion relative to the center of mass is accounted by replacing the mass m_e by the reduced mass $\mu = m_e M/(m_e + M)$; where M is the mass of the nucleus and m_e is the mass of the electron. The wavefunction is given by the solution of the Schrödinger equation :

$$-\frac{\hbar^2}{2\mu}\nabla^2\psi + V\psi = E\psi \qquad \text{(A-26)}$$

and inserting the coulomb potential with origin at nucleus we get:

$$-\frac{\hbar^2}{2\mu}\nabla^2\psi - \frac{Ze^2}{4\pi\varepsilon_o r}\psi = E\psi \qquad \text{(A-27)}$$

Due to the spherical symmetry of the potential a spherical co-ordinate system is chosen. Since the potential depends only upon *r*, the equation wavefunction can be separated into radial and angular components-

$$\Psi(r,\theta,\phi) = R(r)Y(\theta,\phi) = R(r)\Theta(\theta)\Phi(\phi) \tag{A-28}$$

Inserting this into Schrödinger equation we get three equations:

$$-\frac{r}{R(r)}\frac{d^2}{dr^2}\left[rR(r)\right] + l(l+1) = \frac{2\mu r^2}{\hbar^2}\left[E - V(r)\right] \tag{A-29}$$

$$\left[\frac{1}{\sin\theta}\frac{d}{d\theta}\left(\sin\theta\frac{\partial}{\partial\theta}\right) + \frac{m^2}{\sin^2\theta}\right]\Theta(\theta) = l(l+1)\Theta(\theta) \tag{A-30}$$

and

$$\frac{d^2\Phi(\phi)}{d\phi^2} = -m^2\Phi(\phi). \tag{A-31}$$

The solution to the radial equation gives a radial eigenfunction $R(r)$ depending upon principal quantum number *n* and azumithal quantum number *l*. The energy eigenvalues depend only on the principal quantum number and are given by:

$$E_n = -\frac{1}{2}\frac{e^4\mu}{\left(4\pi\varepsilon_0\hbar\right)^2}\frac{Z^2}{n^2} = -R_M\frac{Z^2}{n^2} \tag{A-32}$$

where R_M is the Rydberg constant for a system with reduced mass μ. The quantum number *n* can only have positive integer values from 1 to infinity.

The solutions to the angular part of the function are known as spherical harmonics. The solution to the equation A-6, contain the function exp i$m\phi$, which is single valued (i.e. $\Phi(\phi)=\Phi(\phi+2\pi)$) only if the quantum number $m = 0,\pm1\pm2,\ldots$. Similarly the equation A-5, containing the function $\Theta(\theta)$ requires that the number *l* be quantized (*l*= 0,1,2,…(*n*-1)) and $l \geq |m|$. The quantity *l(l+1)* in the left hand side of the equation A-5 is actually the operator representing the square of the angular momentum operator $\boldsymbol{l^2}$, so the solution

implies that the angular momentum can only have discrete values. Similarly, we find that the projection of angular momentum in any direction can only take the values $m\hbar$.

Since the projection of angular momentum on the z axis can only have finite values, this implies that the angular momentum vector can only have $2l+1$ different directions, but never parallel to the z-axis. So the l_z component of $\boldsymbol{l}$ is fixed while l_x and l_y are said to precess about the z-axis in keeping with the Heisenberg uncertainty principle.

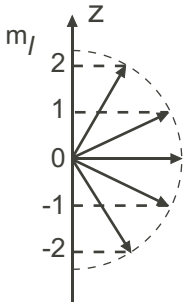

Fig. A.1 The quantization of the z axis projection of the angular momentum, results in quantization of the direction of the angular momentum.

The electron also has an intrinsic angular momentum, which is called spin. The spin angular momentum has a value $\hbar\sqrt{s(s+1)}$ where s can only have the value 1/2. The component s_z is $m_s\hbar$ where $m_s = \pm 1/2$ for electrons.

Thus a total of four quantum numbers; principal quantum number n, azumithal quantum number l, magnetic quantum number m, and spin quantum number s, are required to describe any state, and the energy values are $(2n^2)$-fold degenerate.

A.1.1.2 Two Electron Atoms

For two electrons systems, the center of gravity approximation cannot be made, and so it is assumed that the origin is at nucleus itself. The Schrödinger equation in the case of two electron systems is:

$$\left(-\frac{\hbar^2}{2m}\nabla_1^2-\frac{\hbar^2}{2m}\nabla_2^2-\frac{Ze^2}{4\pi\varepsilon_0 r_1}-\frac{Ze^2}{4\pi\varepsilon_0 r_2}+\frac{e^2}{4\pi\varepsilon_0 r_{12}}\right)\psi(\mathbf{r}_1,\mathbf{r}_2)=E\psi(\mathbf{r}_1,\mathbf{r}_2) \quad \text{(A-33)}$$

The last term is the potential energy arising from the repulsion between two electrons at the distance $(r_{12}=|r_1-r_2|)$. This equation cannot be solved exactly. As a first approximation, the interaction between electrons is neglected. The remaining equation can thus be separated into two equations, for each electron. These equations are identical to the hydrogen atom discussed previously. The wave function is written as the product of these two-electron wave functions.

$$\psi_{a,b}(\mathbf{r}_1,\mathbf{r}_2)=\psi_a(\mathbf{r}_1)\cdot\psi_b(\mathbf{r}_2) \quad \text{(A-34)}$$

where *a* and *b* represent the quantum numbers (excluding spin) of each electron.

A.1.1.3 Pauli Principle and Antisymmetric Wave Functions

As the electrons are indistinguishable – the two wave functions $\psi_{a,b}(1,2)\equiv\psi_a(1)\cdot\psi_b(2)$ and $\psi_{b,a}(1,2)\equiv\psi_b(1)\cdot\psi_a(2)$ represent the same state with same energy eigenvalue. The probability interpretation requires that $|\psi_{a,b}(1,2)|^2=|\psi_{b,a}(1,2)|^2$, so that either $\psi_{a,b}(1,2)=\psi_{b,a}(1,2)$ or $\psi_{a,b}(1,2)=-\psi_{b,a}(1,2)$, but in general, neither of there are true. For example, the product of s function at r_1 and p function at r_2 is not the same as p function at r_1 and s function at r_2. As any linear combinations of solutions to Schrödinger equation are solutions also, so functions that do satisfy this requirement can be constructed.

$$\psi^+=\frac{1}{\sqrt{2}}\left[\psi_{a,b}(1,2)+\psi_{b,a}(1,2)\right],$$

$$\psi^-=\frac{1}{\sqrt{2}}\left[\psi_{a,b}(1,2)-\psi_{b,a}(1,2)\right]. \quad \text{(A-35)}$$

The first function is said to be space symmetric and the second function is said to be space antisymmetric. The total wave function will also include the contribution of spin and can be written as –

$$\Psi(1,2) = \psi(1,2) \cdot \chi(1,2) \qquad \text{(A-36)}$$

where $\psi(1,2)$ is a function of space only while $\chi(1,2)$ is a function of spin. Like the space function total wave functions can be symmetric or anti-symmetric. In both cases the requirement of probability interpretation is satisfied. However, electrons are Fermi particles, and are described by anti-symmetric total wave functions. This is also indicated by the Pauli-exclusion principle, which states that no two electrons can have all four quantum numbers that are the same. An anti-symmetric wave function always satisfies this rule as the requirement $\Psi_{a,b}(1,2) = -\Psi_{b,a}(1,2)$, and $a \equiv b$ imply $\Psi \equiv 0$, i.e. the state does not exist when all quantum numbers are same.

The total function is anti-symmetric if the space function is symmetric and the spin function is anti-symmetric, or vice-versa. Let α represent m_s=+1/2, "spin up" state and β represent m_s=-1/2 "spin down" state. For two electrons four possible combinations exist -

$$\chi_1(1,2) = \alpha(1)\alpha(2), \qquad M_S=1$$

$$\chi_2(1,2) = \alpha(1)\beta(2), \qquad M_S=0$$

$$\chi_3(1,2) = \beta(1)\alpha(2), \qquad M_S=0$$

$$\chi_4(1,2) = \beta(1)\beta(2). \qquad M_S=-1 \qquad \text{(A-37)}$$

Of these, χ_1 and χ_4 are symmetric, while χ_2 and χ_3 do not have defined symmetric or anti-symmetric properties, but symmetric and anti-symmetric functions can be constructed out of them as

$$\chi_{23}^{+} = \frac{1}{\sqrt{2}}\left[\alpha(1)\beta(2) + \beta(1)\alpha(2)\right]$$

$$\chi_{23}^{-} = \frac{1}{\sqrt{2}}\left[\alpha(1)\beta(2) - \beta(1)\alpha(2)\right] \qquad \text{(A-38)}$$

Thus, there are 3 symmetric spin states with M_S=+1, 0 and -1 and one antisymmetric spin state with M_S=0. Since m_s is the projection of the individual spins, M_S is the projection of the spin of the total spin angular momentum vector defined by $\mathbf{S}=\mathbf{s_1}+\mathbf{s_2}$. The associated quantum number S ($|\mathbf{S}| = \hbar\sqrt{S(S+1)}$) can take two possible values S=0 and S=1. Thus, the three symmetric spin states correspond to three projections of the total spin S=1, while the single antisymmetric state χ_{23}^{-} with M_S=0 must have S=0. The two possible (antisymmetric) states for the two electrons are

$\psi^{+}.\ \chi^{-}$: singlet state with S=0, M_S=0,

$\psi^{-}.\ \chi^{+}$: Triplet state with S=1, M_S=+1,0,-1

In the ground state of He and He-like ions, both electrons have n=1, thus l=0 and m_l=0. According to pauli's principle, one of the electrons must have m_s=+1/2 and the other m_s=-1/2. M_S can only be zero so only singlet state is possible. However all excited states of He can exist as singlet or triplet state.

A.1.1.4 Interaction between electrons

For the analysis the interaction between electrons was ignored. The effect of the interaction is modeled as a small perturbation on the two-electron wave function and

calculated using first order perturbation theory. The calculation is done for both symmetric and antisymmetric space functions. Calculated perturbation in energy from electron-electron interaction is therefore

$$E' = J \pm K \tag{A-39}$$

where plus and minus refer to S=0 and S=1 states. J is known as direct electrostatic integral and is due to energy of interaction between the two electrons. K is known as exchange integral, as it arises from effect of exchanging the two electrons. K has no classical counterpart, but is of the same form as J and still due to electrostatic interaction between the electrons [Joh 99].

A.1.1.5 Many Electron Systems

The approach used in two electron systems can now be generalized to many-electron systems. The Hamiltonian is of the form [Joh 99] –

$$H = \sum_{1}^{n}\left(-\frac{\hbar}{2m}\nabla_i^2 - \frac{Ze^2}{4\pi\varepsilon_0 r_i}\right) + \sum_{i<j=1}^{N}\frac{e^2}{4\pi\varepsilon_0 r_{ij}} + \sum_{1}^{N}\xi(r_i)(\mathbf{l}_i \cdot \mathbf{s}_i) \tag{A-40}$$

The first sum represents kinetic and potential energies of the electron in the central field of the nucleus. The second sum represents the repulsion between electrons. The last sum describes the potential energy of the magnetic interaction between the electron spin and the magnetic field due to orbital motion of the electron. A number of other smaller interactions are observed, but can be neglected at this stage.

A.1.1.6 Central Field Approximation

As a first approximation in solving equation A-15, the spin-orbit coupling term is ignored. In case of many electron systems, the effect of electron-electron repulsion

cannot be ignored. However, another approximation can be made. The vector $\mathbf{r}_{ij} = \mathbf{r}_i - \mathbf{r}_j$ can be considered to be a sum of two components, one radial one tangential. It is assumed that most of the interaction is in the radial direction, which leads to the central field approximation which states that –

1. Each electron moves independently of all others in a field created by nucleus and the average effect of the repulsion from all other electrons
2. The field created by the nucleus is spherically symmetric – i.e. is a central field.

The corresponding Hamiltonian is

$$H = \sum_{1}^{n}\left(-\frac{\hbar}{2m}\nabla_i^2 - V(r_i)\right) \qquad \text{(A-41)}$$

where the potential r_i is the combined average field and only a function of distance r_i. Since the coupling term is absent, the equation can be separated into N independent one-electron equations, and the overall solution is the product of one-electron functions –

$$\Psi(\mathbf{r}_1, \mathbf{r}_2, \ldots \mathbf{r}_N) = \psi_1(\mathbf{r}_1)\psi_2(\mathbf{r}_2)\psi_3(\mathbf{r}_3)\ldots\psi_N(\mathbf{r}_N) \qquad \text{(A-42)}$$

In the central field potential, the energies are seen to depend on both *n* and *l,* and the energy eigenvalues in the central field approximation are described by the quantum numbers (*n,l*).

The N equations are not independent of each other, since the potential energy V depends upon the overall configuration. The central field V is computed by an iterative scheme. First a hydrogen-like potential is assumed, and the electronic configuration calculated. Then this configuration is used to derive the averaged central field, the new field is used to compute the wave functions. This process is continued until it converges and a self-consistent picture emerges.

A.1.2 Quantum numbers for the Whole Atom and Term Symbols

The product wave functions are not the correct solutions to the many-electron systems. Just like the two electron case, the space wave function must be symmetric or antisymmetric against exchange of electrons, while the complete wavefunction must be symmetric. Such functions are constructed by linear combination of product functions, and include the consideration of spin, and all possible permutations of electrons.

Since the wavefunctions of electrons are coupled, it is useful to consider transitions as between two different states rather than just the motion of one electron. These states are designated as term. The atomic term symbol has the form $^{2S+1}L_J$. It is seen that the exchange interaction between electrons depends on the total angular momentum $\mathbf{L} = \sum \mathbf{l}_i$ and the resultant spin $\mathbf{S} = \sum \mathbf{s}_i$. **L** and **S** then add together to give total angular momentum **J** of the extra-nuclear elecrons of the atom and the quantum number J can take the values: $J = (L+S),(L+S-1),\ldots|L-S|$. Each of the possible L values can occur with each of the possible S values. States with same L values form a *multiplet term* (designated as S,P,D,F..) , the number of whose terms is 2S+1. 2S+1 is called the *multiplicity* and is added to the upper left hand side of the term symbol. In addition the J value is added to the lower right. For example the ground state of helium is represented as $2\ ^1S_0$ first metastable state of helium is labeled $2\ ^3S_{0,1,2}$.

A.1.2.1 Other Corrections

The effect of non-central interaction is computed using perturbation of the present energy levels. As in the two electron case, it produces both direct and exchange contribution. Another major correction comes from the interaction of the electron spin with the magnetic field due to angular momentum of the electron. This is dominant only for outer shell electrons as for all closed shell configurations the quantum numbers **L** and **S** are zero.

A.1.3 Radiative Transitions and Selection Rules

The emission strength of an atomic line is expressed in terms of an emission coefficient ε which is the energy emitted by an infinitesimal volume per second per unit solid angle given by the formula [Joh99]:

$$\varepsilon = \hbar \nu n_2 A_{21} \tag{A-43}$$

Where n_2 is the density of emitting atoms and A_{21} is the Einstein coefficient for transition between two energy levels. The Einstein coefficient expresses the probability of transition between the two states and is expressed as [Joh 99]:

$$A_{21} = \frac{8\pi^2 \nu^3}{3\varepsilon_0 \hbar c^3} d_{12}^2 \tag{A-44}$$

d_{12} is the norm of dipole matrix element between two atomic states. The matrix elements are vector quantities which depend upon the wave functions ψ_1 and ψ_2 of the two states:

$$d_{12} = \int \psi_1 \mathbf{p} \psi_2 d\tau \tag{A-45}$$

where **p** is a physical vector quantity which depends on the 3N co-ordinates for an N particle system. In the simples at more common case **p** is the electric-dipole moment of the system, and the radiation is akin to electric dipole radiation. If the matrix element is zero it represents a *forbidden transition*. In practice the forbidden transition is often

seen, as it may be allowed as a *quadrouple transition* or a *magnetic dipole transition*. Detailed calculations show that the probability of these other transitions is very low compared to dipole transitions.

In practice it is difficult to compute the matrix elements exactly, but allowed transitions can be predicted based on properties of the integral. For dipole transitions there are two *rigorous* selection rules-

1. The initial and final states must have opposite parity (Laporte Rule)
2. $\Delta J = 0,\pm 1$ *and* $J = 0 \rightarrow J = 0$ *not allowed*

Furthermore, the following approximate rules are also valid for light elements:

$\Delta L = 0, \pm 1$

$\Delta S = 0$ (intercombination rule)

For transitions in between two states having same principal quantum number.

A.2 Molecular Structure

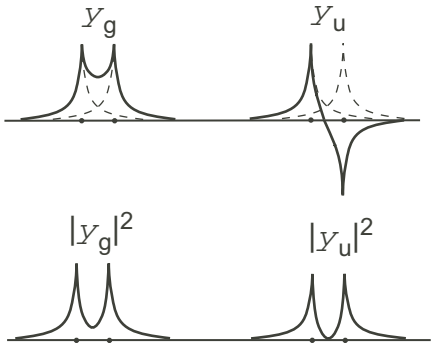

Fig A.2:Illustration showing probability distributions of bonding and anti-bonding anti bonding molecular orbitals

A.2.1 Born-Oppenheimer Approximation

Isolated atoms have three degrees of freedom, specified by the motion along three o-ordinates. When two atoms are bound in a molecule, three of these degrees of freedom

describe the motion of center of mass of the whole system. The remaining degrees of freedom are represented as vibration about the center of mass and rotation about the two axis perpendicular to the internuclear axis. So besides the electronic energy the energy of the system has vibrational and rotational components. The Hamiltonian for the system can be written as [Joh99]:

$$H = T_N + T_e + V_{NN} + V_{ee} + V_{eN} \tag{A-46}$$

Kinetic energy of nuclei - $$T_N = \frac{\hbar^2}{2M_A}\nabla^2_{\mathbf{R}_A} - \frac{\hbar^2}{2M_B}\nabla^2_{\mathbf{R}_B} \tag{A-47}$$

Kinetic energy of electrons- $$T_e = \frac{\hbar^2}{2m}\sum \nabla^2_{\mathbf{r}_i} \tag{A-48}$$

Repulsion between Nuclei $$V_{NN} = \frac{Z_A Z_B e^2}{4\pi\varepsilon_0 |R_A - R_B|} \tag{A-49}$$

Electron-Electron Repulsion $$V_{ee} = -\sum_{i<j} \frac{e^2}{4\pi\varepsilon_0 |r_i - r_j|} \tag{A-50}$$

Electron-Nucleus attraction $$V_{ee} = -\sum_i \frac{Z_A e^2}{4\pi\varepsilon_0 |r_i - R_A|} + \frac{Z_B e^2}{4\pi\varepsilon_0 |r_i - R_B|} \tag{A-51}$$

where $\mathbf{R}_A$, $\mathbf{R}_B$ and $\mathbf{r}_i$ are the position vectors of the nuclei and the electrons.

The Schrödinger equation for the system is impossible to solve, so approximations are made. The Born-Oppenheimer approximation states that nuclei, because of their greater mass, move slowly compared to electrons, so the Schrödinger equation can be solved for fixed values of $\mathbf{R}_A$ and $\mathbf{R}_B$, and then the variation of eigenvalues can be studied as a function of $\mathbf{R} = \mathbf{R}_A - \mathbf{R}_B$. This approximation is equivalent to separation of molecular wavefunction into an electronic and nuclear part, where the electronic wave function depends upon the parameter **R**.

$$\Psi = \psi_e(\mathbf{r}_i, \mathbf{R})\chi_N(\mathbf{R}_A, \mathbf{R}_B) \tag{A-52}$$

A.2.2 Electronic Energy of Diatomic Molecules

To obtain the electronic energy levels and wave function, the Schrödinger equation for electrons in a field of two molecules has to be solved. This is done by assuming each electron outside the closed shell as belonging to both nuclei, usually by writing the resulting *molecular orbital* as a linear combination of two atomic orbitals (LCAO). There are two such combinations which satisfy the requirement that the electron density be invariant of exchange of electrons. One of these increases the electron density between the nuclei (bonding orbital), while the other has the reverse effect (anti-bonding orbital).

A.2.2.1 Hydrogen Molecular ion

The hydrogen ion is the simplest molecule, consisting of two protons and one electron. The Hamiltonian operator for the fixed values of $\mathbf{R}_A$ and $\mathbf{R}_B$ is given by:

$$H_e = -\frac{\hbar^2}{2m}\sum \nabla^2_{\mathbf{r}_i} - \frac{e^2}{4\pi\varepsilon_0|\mathbf{r}-\mathbf{R}_A|} - \frac{e^2}{4\pi\varepsilon_0|\mathbf{r}-\mathbf{R}_B|} + \frac{e^2}{4\pi\varepsilon_0|\mathbf{R}_A-\mathbf{R}_B|} \tag{A-53}$$

Let $\mathbf{r}-\mathbf{R}_A = \mathbf{r}_A$, $\mathbf{r}-\mathbf{R}_B = \mathbf{r}_B$ *and* $|\mathbf{R}_A-\mathbf{R}_B| = R$

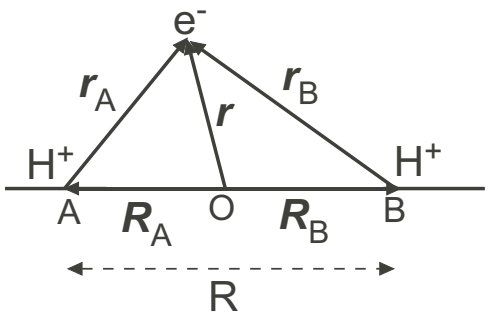

Fig. A.3: The hydrogen molecular ion. The positions of the two nucleii are marked by points A and B and the position of the electron is marked by point O

When the distance R between the protons is large, the electron is localized to either A or B and in its ground state described by the one-electron atomic orbital $\phi_{1s}(\mathbf{r}_A)$ or $\phi_{1s}(\mathbf{r}_B)$. At smaller distances the electron is shared, and has to be symmetric with respect to A and B. There are two such linear combinations that are symmetric between A and B.

$$\psi_g(\mathbf{r},R) = \frac{1}{\sqrt{2}}\left[\phi_{1s}(\mathbf{r}_A) + \phi_{1s}(\mathbf{r}_B)\right] \text{ and}$$

$$\psi_u(\mathbf{r},R) = \frac{1}{\sqrt{2}}\left[\phi_{1s}(\mathbf{r}_A) - \phi_{1s}(\mathbf{r}_B)\right] \qquad \text{(A-54)}$$

ψ_g is even and ψ_g under reflection in the midpoint. (The subscripts g and u stand for "gerade" and "ungerade" which are german for even and odd. Once these wavefunctions are constructed, the total energy is evaluated for the trial functions for different values of R, and the total energy is found to have a minimum at a certain nuclear distance R_0 for the ψ_g orbital. The attractive force arises because the oppositely charged nuclei are attracted to the enhanced negative charge between the nuclei (for ψ_g orbital). At the internuclear distance this attraction is just sufficient to balance the repulsive force between nuclei. For the ψ_u orbital no such minima is seen as there is a reduction of

negative charge density at the centre, leading to increased repulsion. Like an atom the molecule may also be excited to higher orbitals. For example, for H_2^+ there is a bonding $\phi_{2s}(\mathbf{r}_A)+\phi_{2s}(\mathbf{r}_B)$ and an anti-bonding $\phi_{2s}(\mathbf{r}_A)-\phi_{2s}(\mathbf{r}_B)$

When constructing molecular orbitals from p orbitals, the angular momentum quantum number becomes important. Unlike an atom, a molecule has an internally defined direction – the molecular axis. The projection of angular momentum along this axis becomes constant, and the angular momentum vector precesses about this axis. The sign of m_l is not important due to symmetry. The molecular orbital is thus designated in terms of the quantum number $\lambda = |m_l|$ as $\sigma, \pi, \delta, \varphi \ldots for\ \lambda = 0,1,2,3\ldots$ each molecular orbital except σ being doubly degenerate.

A.2.2.2 General Structure of Diatomic Molecules

The filling of orbitals is determined by Pauli's exclusion principle. First the lower bonding orbitals are filled up, and additional electrons go into the anti-bonding orbitals. Three of the 2p orbitals are bonding. The oxygen has four 2p valence electrons, so in O_2 molecule, six of the eight valence electrons go into three bonding orbitals, and two into antibonding orbitals; resulting in two filled bonding orbitals, constituting a "double bond".

For homonuclear molecules, the equilibrium of the electron distribution is symmetric with respect to the two nuclei. The centroids of the electron and nuclear charge distributions coincide and the molecule has no net dipole moment. For hetronuclear molecules, the electron density is favored towards one of the nucleus, leading to a

permanent dipole moment. This is important, because *the appearance of pure vibrational and rotational spectra depends upon the existence of dipole moment* [Her50].

A.2.3 Labeling of Electronic States

Just as atomic states are labeled, molecular configurations which give rise to different energy levels, are labeled according to resultant angular momentum vectors. The quantum numbers λ of the molecular orbitals are added to form the resultant quantum number Λ. States with $\Lambda = 0,1,2,\ldots$ are designated by $\Sigma, \Pi, \Delta, \ldots$. The individual electron spins couple to form a resultant spin S, but it is the axial component of the spins Σ, that are coupled to Λ forming a resultant Ω:

$$\Omega = |\Lambda + \Sigma| \qquad \text{(A-55)}$$

Each state takes 2S+1 different values. A state with S=0 has only one value of Σ (Σ=0), and hence, only one value of Ω. These states are called singlets. States with S=1 are triplets; as Λ=1 and Σ= -1,0,+1 there are three values of Ω(0,1,2) and the states are designated $^3\Pi_0$, $^3\Pi_1$, and $^3\Pi_2$.

There are two further considerations for molecular states. For homonuclear molecules, the states can be symmetric or antisymmetric with respect to the center of nuclei. These states are designated by the subscript g or u.

Secondly, the symmetry with respect to reflection in any plane passing through both nuclei also has to be considered. As Σ states are degenerate, they may be either be symmetric or anti-symmetric with respect to the transition and are labeled Σ^+ or Σ^- repectively. For Π states which are doubly degenerate, suitable states may be constructed

by taking a linear combination of the two basis functions, it is possible to construct the Π^+ and Π^- states. Thus the overall term symbol for molecular states is represented as:

$$Term\,Symbol = {}^{2S+1}\Lambda_{\Omega,(g/u)}^{(+/-)} \tag{A-56}$$

As convention the ground state is labeled X, while A,B,C, … are used for excited states with same multiplicity. States with multiplicity different from ground state are labeled a, b,c,… . For example the ground state of C_2 molecule is designated as X ^3P_u and the first excited state is A^3P_g... and the singlet states are labeled as a^1S_g, b^1P_u. ,. The only exception is N_2 where the convention is to label the triplet states as A,B,C… adnd singlet states as a,b,c… .

A.2.3.1 Vibrational Spectra

We assume that the vibration of a molecule is the harmonic motion of two point like atoms relative to each other. Such a system is modeled as the oscillation of a reduced mass (m) about an equilibrium position. This model is called the "Harmonic Oscillator". Substituting this in the schoredinger equation we get:

$$\frac{\partial^2\psi}{\partial x^2} + \frac{8\pi\mu^2}{h^2}\left(E - \tfrac{1}{2}kx^2\right)\psi = 0 \tag{A-57}$$

The mathetimatical solution to this equation shows that only discrete values of E are allowed and characterized by

$$E(\nu) = \frac{h}{2\pi}\sqrt{\frac{k}{\mu}}\left(\nu + \tfrac{1}{2}\right) = h\nu_{osc}\left(\nu + \tfrac{1}{2}\right) \tag{A-58}$$

where the vibrational quantum number ν can take only integral values. The harmonic oscillator consists of a series of equidistant levels.

A.2.3.2 Anharmonic Oscillator

The harmonic oscillator is characterized by a parabolic potential curve. However for real molecules, when atoms are at a great distance from each other, the potential has a constant value. Therefore the form of the anharmonic oscillator is as shown in Fig. A.4 . The minimum of this curve corresponds to an equilibrium position, and the potential energy near equilibrium can be approximated by a the anharmonic oscillator potential -

$$V = f(r - r_e)^2 - g(r - r_e)^3 \qquad \text{g<<f} \tag{A-59}$$

The motion of an anharmonic oscillator is not a pure sine form (harmonic), but can be represented as a superposition of fundamental and overtone vibrations. For small values of anharmonicity (g<<f) the solution to the schroedinger equation is given by –

$$E_v = hc\omega_e\left(v + \tfrac{1}{2}\right) - hc\omega_e x_e\left(v + \tfrac{1}{2}\right)^2 + hc\omega_e y_e\left(v + \tfrac{1}{2}\right)^3 + \ldots \tag{A-60}$$

where $\omega_e >> \omega_e x_e >> \omega_e y_e$. The energy levels of the anharmonic oscillator are not equidistant but decrease with increasing v.

A.2.4 Rotational Energy Levels

For calculating the rotational energy levels, the molecule is treated as a rigid dumbbell, consisting of masses M_A and M_B, joined by a rigid bar of length R_0, rotating about an axis through the center of mass. Classically, the system has an angular momentum $\mathbf{L} = I\omega$ and energy $I\omega^2/2 = L^2/2I$. Quantum mechanically, the Schrödinger equation for nuclear co-ordinates must be solved. The solutions are the spherical harmonics $Y(\theta,\varphi)$, and the allowed values of angular momentum are $\sqrt{J(J+1)}\hbar$ .The energy eigen-values are given by:

$$E_r = \frac{1}{2I} J(J+1)\hbar^2 \tag{A-61}$$

The energy is usually expressed in terms of wavenumbers and denoted by the symbol F:

$$F(J) = \frac{E_r}{hc} \times 10^{-2} = BJ(J+1)\,cm^{-1} \qquad \text{(A-62)}$$

B depends on the mass of nuclei and the equilibrium inter-nuclear distance R_0. B varies from one electronic state to another due to variation in R_0.

A.2.5 A Selection Rules for Vibrational and Rotational Spectra

Electronic, vibrational and rotational energy levels differ by orders of magnitude in their separation. Thus these different transitions occur in different regions of the spectrum. Rotational spectra are seen in the far infrared region – 0.1 mm to 30 cm. The vibration-rotation spectra between different vibration levels of the same electronic state, is found mainly in the infrared 1-100 μm. Transitions in electronic states occur in near infrared, UV and visible regions. Vibrational and rotational spectra are seen in absorption, rather than emission. This is because the Einstein coefficient for emission shows a strong dependency on wavelength ($\sim\nu^4$).

Rotational spectra occur only if the molecule posses a permanent electric dipole moment. The selection rule for the rotational quantum number is given by:

$$\Delta J = \pm 1$$

Like the rotational spectra, vibrational-rotation spectrum exists only for molecules with permanent dipole moment. Disregarding anharmonic transitions, all transitions occur in such a molecule with the selection rule:

$$\Delta \nu = \pm 1$$

Due to anharmonic correction, overtones to the fundamental are also present. The rotational structure turns each line into a band of a group of lines spaced at equal intervals

of 2B on either side of the band origin. The selection rule $\Delta J = \pm 1$ still holds for rotational quantum number. The transitions with $J' = J'' + 1$ fall to the high wave-number branch of the main line and are known as the R branch, while the low wavenumber side $J' = J'' - 1$ fall on the low wavenumber side and are known as the P branch. The band origin corresponds to the forbidden $J' = 0 \leftrightarrow J'' = 0$ transition.

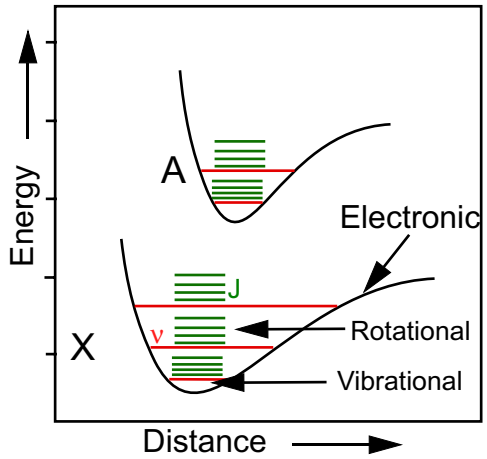

Fig. A.4: General energy diagram for molecular states. The electronic energy levels are represented by the curves for the anharmonic oscillator. Each electronic state has several vibrational and rotational states associated with it.

A.2.5.1 Electronic Energy Levels

The electronic spectrum is seen as a series of bands, due to transition between vibrational and rotational energy levels in each electronic band. Each pair of vibrational levels (ν', ν'') gives rise to a band, which is further composed of transitions between different rotational levels $J' - J''$. The electronic spectrum appears even if the molecule does not have a permanent dipole moment.

The selection rules for transition are different from rotational and vibration spectra. For electric dipole transition the selection rule becomes

$$\Delta J = 0,\pm 1 \;\; with\, J = 0 \rightarrow J = 0 \, forbidden$$

Here J is the total angular momentum, including the contribution if nuclear rotation. This selection rule allows a third rotational branch corresponding to $\Delta J = 0$, known as the Q branch, in addition to the P and R branches. Similar to atomic spectra there are hund's rules governing transitions depending upon the change in angular momentum:

$$\Delta\Lambda = 0,\pm 1$$

$$\Delta S = 0$$

Thus singlet – triplet transitions are forbidden. However this rule tends to break down as the nuclear charge increases. A further selection rule is that Σ^+ cannot combine with Σ^- states, although both can combine with Π states.

According to these selection rules, the wavenumbers of the band origins can be derived as:

$$\nu = \nu_e + \nu_r = \nu_e + \omega_e(\upsilon' + \tfrac{1}{2}) - \omega_e' x_e(\upsilon' + \tfrac{1}{2})^2 + \ldots - \left[\omega_e''(\upsilon'' + \tfrac{1}{2}) - \omega_e'' x_e''(\upsilon'' + \tfrac{1}{2})^2 + \ldots\right]$$

Or
$$\nu \cong \nu_{00} + \omega'\upsilon' - \omega''\upsilon'' \qquad \text{(A-63)}$$

where ν_e is the separation of potential minima of the two electronic states and ν_{00} is the wavenumber of the (0,0) band origin. There is no selection rule for υ in electronic transitions so the entire band system may extend over several units of ω' and ω'' which may extend over 100 nm or more. If $\omega' \cong \omega''$, bands with same $\Delta\upsilon$ appear on top of each other. A band system with a common upper or lower vibrational level is known as a progression; a υ' progression for fixed υ'' and a υ'' progression for fixed υ'. The number of strong bands is determined by the population of the different bands and transition probabilities of those levels.

A.2.5.2 Intensity in Electronic Bands: Franck-Condon Principle

Franck-Condon principle states that the electronic jump in a molecule takes place so rapidly in comparison to vibrational motion that immediately afterwards the nuclei have not appreciable altered their position or velocity compared to the state before. This means that the nuclear distance R does not change during a transition, so on a potential energy diagram these transitions appear vertical.

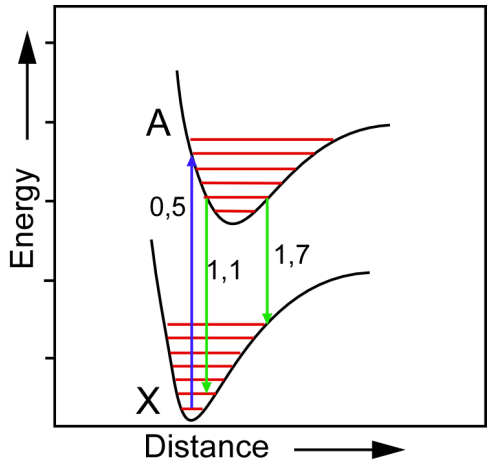

Fig. A.5: Diagram illustrating the Frank-condon principle which governs the intensity of bands in spectra. The position of the electron does not change in a radiative transition. So in absorption the transition marked with the upward arrow is likely to be the strongest, while in emission transitions marked with down arrows will be the brightest. Another way of stating it is that the intensity if proportional to the overlap integral of the two bands.

A.3 Spectra of Some Common Molecules

Using the background information discussed above, molecular emission spectra for some common chemicals can be investigated. The discussion here is limited to the most common species seen in the discharge.

A.3.1 Nitrogen

The energy level diagram of Nitrogen is shown in Fig. A.6 [Her50]. The ground state of Nitrogen molecule is : $KK(\sigma_g 2s)^2(\sigma_u 2s)^2(\pi_u 2p)^4(\sigma_g 2p)^2$. For the Nitrogen molecule

in its ground state both the $\pi_u 2p$ and $\sigma_g 2p$ orbitals are completely filled, and therefore the ground state is $^1\Sigma_g^+$ state. The next orbital is $\pi_g 2p$ which is an anti-bonding orbital hence nitrogen has a large gap between ground state and first excited state.

There are a large number of band systems attributed to neutral nitrogen molecule. In emission the first and the second positive systems are the most easily developed. Both are these are transitions between the triplet state. The first positive system ($B\ ^3\Pi–A^3\Sigma$) spans the range 503 nm – 1051 nm and has about 50 band heads . Most prominent bands are seen at 654.4 nm, 646.8 nm, 891.2 nm and 1051 nm. The first positive system ($B\ ^3\Pi–A^3\Pi$) span the range 281,4 nm – 497.6 nm, and are usually seen as triple headed bands. The most prominent emissions are at 337.1 nm, 357.6 nm, 375.5 nm and 380.4 nm.

A.3.2 CN Free radical

Bright emission from the CN radical is readily seen in air discharges containing even a minute amount of hydrocarbons. This is because the ground state and exited states of CN are close to N_2^+ so energy is efficiently transferred by ion collisions.

The energy level diagram of CN is shown in Fig. A.7 [Her50]. There are two strong systems attributed to CN known as cyanogen red and violet system. The red system arises from the transition $A^2\Pi–X^2\Sigma$ and spans the range 437.3 nm –1505 nm. The strongest lines are observed at 548.5 nm, 635.5 nm, 650.2 nm, 791.5 nm and 1100.0 nm.

The violet system arises from the transition ($B^2\Pi–X^2\Sigma$) and has a wavelength range of 358.3 nm – 460.6 nm. They are usually more prominent than the red system. The most prominent bands are 388.3 nm, 387.1 nm and 421.6 nm.

A.3.3 C_2 Free radical

C_2 bands are readily seen in sources containing carbon. They are also observed in nitrogen discharges containing traces of CO or hydrocarbons. There are many strong bands systems attributed to C_2; the strongest among them is the swan bands. These arise from the transition ($A\ ^3\Pi_g$–$X^3\Pi_u$) and span the range 435.5 nm – 667.7 nm. The strongest emission is seen at 516.5 nm, 473,7 nm and 471.5 nm

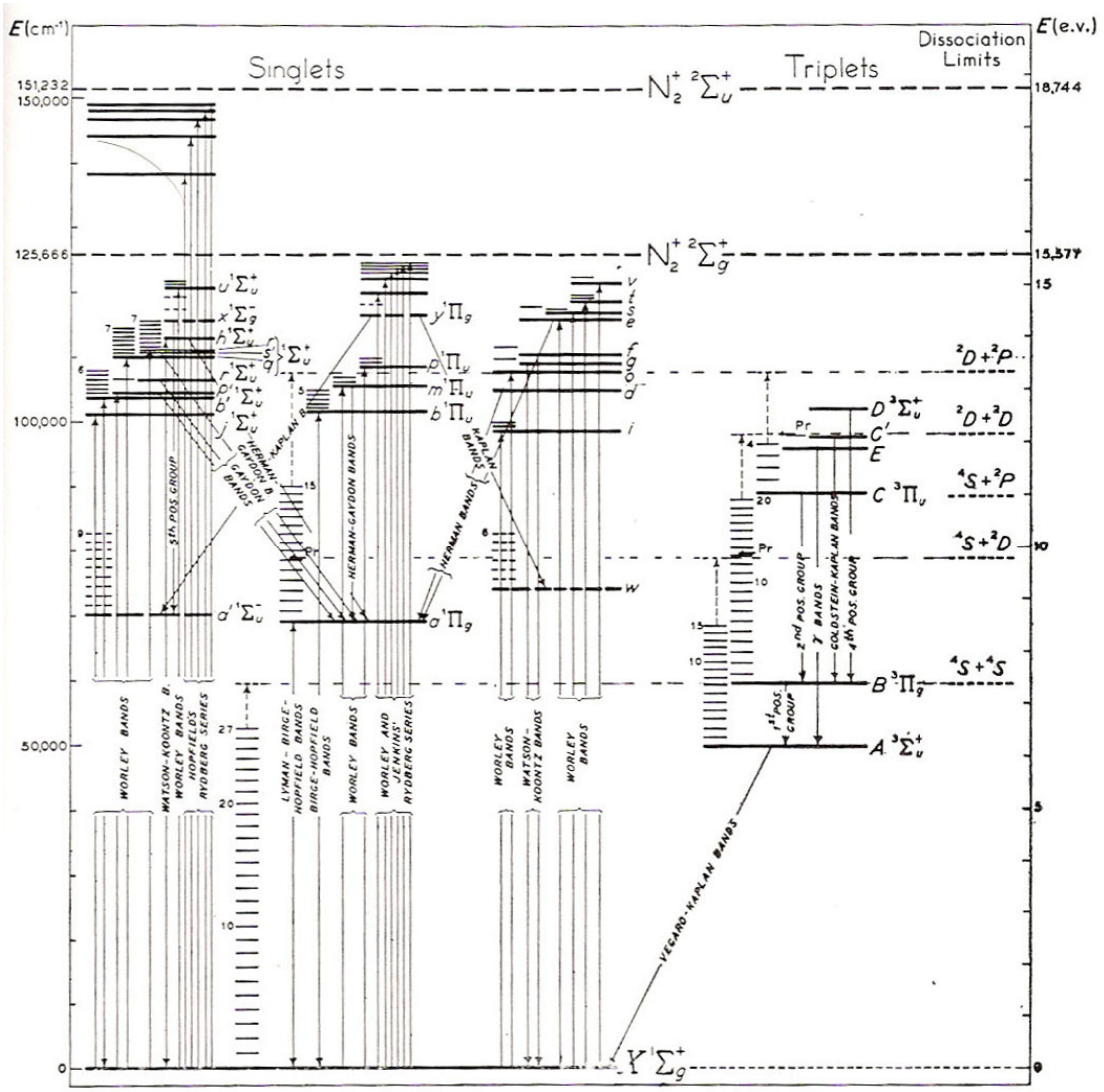

Fig. A.6: Energy level diagram of N_2 molecule (from [Her50]). In low temperature discharges like the one described in this work, the 1'st and the 2'nd positive systems are the most prominent. Nitrogen has a long lived metastable state $A\ ^3\Sigma_u$, which plays an important role in the discharge and afterglow.

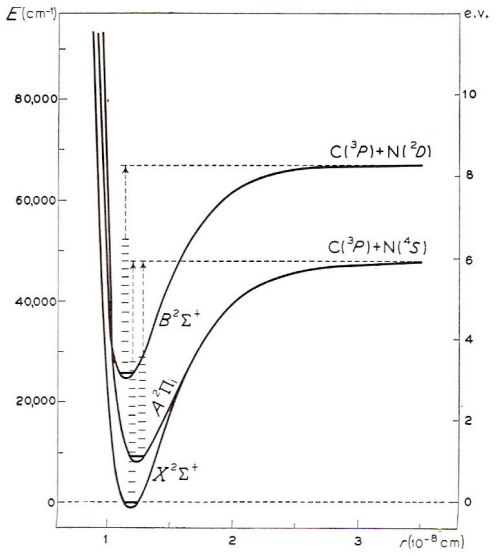

Fig. A.7: Energy level diagram of CN molecule from [Her50]. The (B-A) transitions are the strongest and comprise the CN violet system. The (A-X) transition (red system) spans the red and infrared regions.

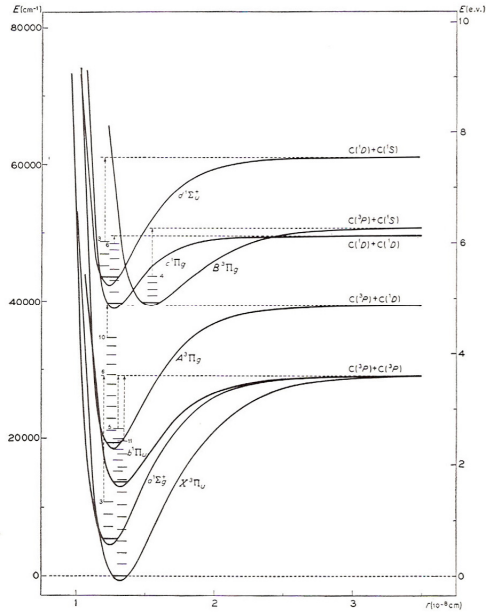

Fig. A.8: Energy level diagram of C_2 molecule (from [Her50]). The transitions A-X (swan bands) are the most common prominent.

References

[Aub07] X. Aubert, G. Bauville, J. Guillon, B. Lacour, V. Puech, A. Rousseau, "Analysis of the self-pulsing operating mode of a microdischarge", *Plasma Sources Science and Technology*, 16(1), pp. 23-32, Feb. 2007

[Bal00] A. Hierlemann, D. Lange, C. Hagleitner, N. Kerness, A. Koll, O. Brand, H. Baltes, "Application-specific sensor systems based on CMOS chemical microsensors," *Sensors and Actuators B*, 70, pp. 2-11. 2000

[Bra68] R.S. Braman, A. Dynako "Direct current discharge spectral emission type detector," *Anal. Chem*., 40(1), pp. 95–106, Jan 1968

[Bro59] S.C Brown, *Basic Data of Plasma Physics,* M.I.T. Press, Cambridge, Mass. 1959

[Bro 02] J.A.C. Broekaert, "The development of microplasmas for spectrochemical analysis," *Anal. Bioanal. Chem.,* 374, pp. 182-187, 2002

[Bro03] H. Nam, G.S. Cha, T.D. Strong, J. Ha, J.H. Sim, R. Hower, S.M. Martin, R.B. Brown, "Micropotentiometric sensors," *Proceedings of the IEEE*, 91 (6), pp. 870-880, June 2003

[Bro05] S.M. Martin, F.H. Gebara, B.J. larivee, R.B. Brown, "A CMOS-Integrated microinstrument for trace detection of heavy metals," *IEEE Journal of Solid State Circuits*, 40 (12), pp. 2777-2785, Dec. 2005

[Cha80] B. Chapman, *Glow Discharge Processes: Sputtering and Plasma Etching*, Wiley, New York, 1980

[Che72] R. Chen, "Measurements of absolute values in biochemical fluorescence spectroscopy," *J. Research National Bureau Standards*, 76A(6), pp. 593-606, 1972

[Che89] H-. S. Chen, S.S. Li, R.M. Fox, W.A. Krull, "Increased junction breakdown voltages in silicon-on-insulator diodes", *IEEE Transactions on Electron Devices.* 36(3), pp. 488 – 492, March 1989

[Cho99] H. Chou, C. Spence, A. Scherer, S. Quake, "A microfabricated device for sizing & sorting DNA molecules," *Proc. Natl. Acad. Sci.*, 96, pp. 11-13, 1999

[Cob41] J. D. Cobine, *Gaseous Conductors*, Mcgraw-Hill, New York, 1941

[Dav95] P. B. Davies, "Infrared laser and microwave spectroscopy of electric discharges", *Chem. Soc. Rev.*, 24, 151 – 157, 1995

[Dav05] C.E. Davis, C.K. Ho, R.C. Huges, M.L. Thomas, "Enhanced detection of m-xylene using a preconcentrator with a chemical sensor," *Sensors and Actuators B*, 104, pp. 207-216, 2005

[Eij00] J.C.T. Eijkel, H. Stoeri, A. Manz "A dc microplasma on a chip employed as an optical emission detector for gas chromatography," *Anal. Chem.,* 72, pp. 2547-2552, June 2000

[Ede02] S-J. Park, J. Chen, C.J. Wagner, N.P. Ostrom, C. Liu, J.G.Eden, "Microdischarge arrays: a new family of photonic device", *IEEE Journal of Selected Topics in Quantum Electronics*, 8(1), pp. 139-147, 2002

[Ede03] J.G. Eden, S-J Park, N.P. Ostrom, S.T. McCain, C.J. Wagner, B.A. Vojak, J. Chen, C. Liu, P. von Allmen, F. Zenhausern,D.J. Sadler, C. Jensen, D.L. Wilcox and J.J. Ewing, "Microplasma devices fabricated in silicon, ceramic, and metal/polymer structures: arrays, emitters and photodetectors", *Journal of Physics D, Applied Physics*, 36 (23), pp. 2869-2977, Nov. 2003

[Eng65] A. von Engel, *Ionized Gases*, Clarendon Press, Oxford, 1965

[Eva03] E.H. Evans, J.A Day, W.J. Price, C.M.M. Smith, K. Sutton, "Atomic spectrometry update. Advances in atomic emission, absorption and fluorescence spectrometry and related techniques," *Journal of Analytical Atomic Spectrometry,* 18(7), pp. 672-711, 2003

[Fas76] G.D. Fasman, *Handbook of Biochemistry and Molecular Biology, Proteins I*, CRC Press, 1976, pp.183-203

[Fis04] A.J. Fischer, A.A. Allerman, M.H. Crawford, K.H.A. Bogart, S.R. Lee, R.J. Kaplar, W.W. Chow, S.R. Kurtz, K.W. Fullmer, J.J. Figiel, "Room-temperature direct current operation of 290 nm light-emitting diodes with milliwatt power levels," *Applied Physics Letters*, 84(17), pp. 3394-3396, 2004.

[Fra60] G. Francis, *Ionization Phenomena in Gases*, Butterworth, London, 1960

[Fre99] C. B. Freidhoff, R. M. Young, S. Sriram, T. T. Braggins, T. W. O'Keefe, J. D. Adam, H. C. Nathanson, R. R. A. Syms, T. J. Tate, M. M. Ahmad, S.

Taylor and J. Tunstall, "Chemical Sensing Using Nonoptical Microelectromechanical Systems," *J. Vac. Sci. Technol. A,* 17 (4), pp. 2300-2307, Jul/Aug 1999

[Fri04] A. Fridman, L. Kennedy, "Plasma Physics and Engineering,"Taylor and Francis, New York, 2004

[Fry99] Ming Fang, Kevin Vetelino, Michael Rothery, Jacqueline Hines, Gregory C. Frye, "Detection of organic chemicals by SAW sensor array," *Sensors and Actuators B*, 56, pp. 155-157, 1999

[Gar99] J. W. Gardner and P. N. Bartlett, *Electronic noses: principles and applications*, Oxford, Oxford University Press, 1999.

[Gol94] H. Golnabi, H. Samimi, "Triggerable spark gap switches for pulsed gas lasers," 65(9), pp. 3030-3031, Sept. 1994

[Hau96] R. P. Haugland, *Handbook of fluorescence probes and research chemicals*, Molecular Probes, Eugene, OR, 1996

[Hop00] J. Hopwood, "A microfabricated inductively coupled plasma generator," *Journal of Microelectromechanical Systems*, 9 (3), pp. 309-313, 2000

[Hop05] J. Hopwood, F. Iza, S. Coy, B.B. Fenner, "A microfabricated atmospheric-pressure microplasma source operating in air," *J. Phys. D,* 38, pp. 1698-1703, 2005

[Her50] G. Herzberg, *Molecular Spectra and Molecular Structure I: Diatomic Molecules*, Prentice-Hall, New York 1939

[Hir92] E. Hirota, "Microwave and infrared spectra of free radicals and molecular ions," *Chemical Reviews*, 92(1) pp. 141- 173, 1992

[Jan 97] Karel Domansky, Jing Li, Jiri Janata, "Selective doping of chemically sensitive layers on a multisensing chip," *J. Electrochem. Soc.,* 144 (4), pp. L75-L78, 1997

[Jan03] J. Janata, "Electrochemical microsensors," *Proc. of IEEE,* 91(6), pp. 864 – 869, June 2003

[Jen01] G. Jenkins, A. Manz, "Optical emission detection of liquid analytes using a micro-machined DC glow discharge device at atmospheric pressure," *Proc. of the Micro Total Analysis Symposium,* 2001

[Joh99] A. Thorne, U. Litzen, S. Johannson, *Spectrophysics: Principles and applications,* Springer, Berlin, 1999

[Kar04] V. Karanassios, "Microplasmas for chemical analysis: analytical tools or research toys? " *Spectrochimica Acta Part B*, 59(7), pp. 909-928, July 2004

[Kat04] T.M. Katona, T. Margalith, C.Moe, M.C. Schimidt, S. Nakamura, J.S. Speck, S.P. DenBaars, "Growth and fabrication of short wavelength UV LEDs," *Proc. of SPIE,* 5187, pp. 250-259, 2004

[Kin00] V. Majidi M. Moser, C. Lewis, W. Hanga and F. L. King, "Explicit chemical speciation by microsecond pulsed glow discharge time-of-flight mass spectrometry: concurrent acquisition of structural, molecular and elemental information," *J. At. Anal. Spectrom.,* vol. 15, pp. 19-25, 2000

[Kus05] M. J. Kushner, "Modelling of microdischarge devices: plasma and gas dynamics", *Journal of Phys. D: Applied Physics*, 38(11) pp. 1633-1643, 2005

[Lak92] J R Lakowicz, H Szmacinski, K Nowaczyk, and M L Johnson, "Fluorescence lifetime imaging of free and protein-bound NADH," *Proc. Natl. Acad. Sci. U S A*., 89(4) pp. 1271–1275, 1992

[Lad00] A.S. Ladokhin, "Fluorescence spectroscopy in peptide and protein analysis," in *Encyclopedia of Analytical Chemistry*, Ed. R.A. Meyers, John Wiley & Sons Ltd., 2000, pp. 5762-5779.

[Lid02] D.R. Lide, Ed., *CRC Handbook of Physics and Chemistry*, CRC Press, New York, 2002

[Lie94] M.A. Lieberman and A.J. Lichtenberg, *Principles of Plasma Discharges and Materials Processing*, Wiley, Toronto, Canada

[Lig55] L.H. Light and P.M. Hooker "Transistor D.C. Convertors," *Proc. of IEE, Part B,* 102, pp. 775-786, 1955

[Lu05] C. -J. Lu, W. H. Steinecker, W. -C. Tian, M. C. Oborny, J. Nichols, M. Agah, J. A. Potkay, H. K. Chan, J. A. Driscoll, R. D. Sacks, K. D. Wise, S. W. Pang, and E. T. Zellers, "First Generation Hybrid MEMS Gas Chromatograph," *Lab On A Chip*, 5, pp. 1123-1131, August 2005

[Mar68] G.V. Marr, *Plasma Spectroscopy*, Elsevier, London, 1968

[Mar00] M.A. Dempster, R.K. Marcus, "Analysis of amino acids and organometallic compounds by particle beam–hollow cathode glow discharge," *J. At. Anal. Spectrom.*, vol. 15, pp. 43 – 48, 2000

[Mas04] G. Frye-Mason, R. Kottenstette, C. Mowry, C. Morgan, R. Manginell, P. Lewis, C. Matzke, G. Dulleck, L. Anderson and D. Adkins*, "*Hand-held Miniature Chemical Analysis System (μChemLab^{TM}*)* for Detection of

Trace Concentrations of Gas Phase Analytes" *Proceedings Micro Total Analysis Systems Workshop,* ed. J. M. Ramsey and A. van den Berg, Kluwer, Dordrecht, The Netherlands, May 2001, pp. 658–660. Spain, March 14–19th, 2004

[Mor69] J.C Morris, R.U. Krey and R.L. Garrison, "Bremsstrahlung and recombination radiation of neutral and ionized Nitrogen", *Physical Review*, 180 (1), pp. 167-183, 1969

[Mil01] R. A. Miller, E. G. Nazarov, G. A. Eiceman, and A. T. King, "A MEMS radio-frequency ion mobility spectrometer for chemical vapor detection*," Sens. Actuators A, Phys*., 91, pp. 301–12, July 2001.

[Mit03] B. Mitra, C. Wilson, L. Que, and Y. B. Gianchandani. "A Micro-Fluidic Ultra-Violet Emission Source for Direct Fluorescence of Tryptophan," *Proc. of the IEEE Engineering in Medicine and Biology Society Conference*, Cancun, Mexico, September 2003.

[Mit04] B. Mitra, Y.B. Gianchandani "On the temporal evolution of micro-discharge spectra and detection of organic vapors in air," *Proceedings of the 8th International Conference on Micro Total Analysis Systems (MicroTAS)*, pp. 420-22, Malmo, Sweden, Sept. 2004

[Mit05A] B. Mitra and Y.B. Gianchandani, "The Micromachined FlashFET: A Low-Power, Three-Terminal Device For High Speed Detection of Vapors at Atmospheric Pressure," *IEEE International Conference on Micro Electro Mechanical Systems*, Miami, 2005

[Mit05B] B. Mitra and Y.B. Gianchandani, "Microdischarge-microplasma hybrids for detection of vapors at atmospheric pressure," *IEEE Conference on Sensors,* Irvine CA, Nov. 2005

[Mit06] B. Mitra, C.G. Wilson, L. Que, P. Selvaganapathy and Y.B. Gianchandani, "Microfluidic Discharge-Based Optical Sources for Detection of Biochemicals," *Lab-on-a-Chip* (IOP), 6(1), pp. 60-65, 2006

[Mit07] B. Mitra and Y.B. Gianchandani, "The detection of chemical vapors in air using optical emission spectroscopy of pulsed microdischarges from two and three electrode microstructures," submitted to the *IEEE/ASME Journal of Microelectromechanical Systems*

[Nil64] F.E. Niles, W.W. Robertson, "Atomic emission in the helium afterglow," *Journal of Chemical Physics*, 40 (12) pp. 3568-71, 1964

[Nie03] K. Kunze, M. Miclea, J. Franzke, K. Niemax, "The dielectric barrier discharge- A powerful microchip plasma for diode laser spectrometry," *Spectrochim. Acta B*, 58(8), pp. 1435-1443, August 2003

[Pea62] R.W.B Pearse and A.G. Gaydon, *The identification of molecular spectra,* Chapman and Hall Publications, New York, 1962

[Que05] L. Que, C. Wilson, Y.B. Gianchandani, "Microfluidic electrodischarge devices with integrated dispersion optics for spectral analysis of water impurities," *Jour. of Microelectromechanical systems*, 14 (2), pp. 185-191, 2005

[Rob88] R. T. Robiscoe, A. Kadish and W. B. Maier II, "A lumped circuit model for transient arc discharges", *J. Appl. Phys*., 64(9), pp. 4355-4363, Nov. 1988

[Rai89] Yu. P. Raizer and M.N. Shneider, "Simplified kinetic equation for electrons in nonuniform fields of arbitrary strength in connection with the cathode sheathof a glow discharge", *Sov. J. Appl. Phys.*, 15(3), Mar 1989

[Rai97] Yu. P. Raizer, *Gas Discharge Physics*, Springer Verlag, Berlin, 1997

[Spa00] G. E. Spangler "Fundamental Considerations for the Application of Miniature Ion Mobility Spectrometry to Field Analytical Applications" *Field Analytical Chemistry & Technology*, 4 (5) pp 255-267, 2000

[Stu62] R.V. Stuart and G.K. Wehner, "Sputtering at very low bombarding energies,"*Jour. Applied Physics,* 33 (7) pp. 2345-2352, 1962

[Sur90] M. Surendra, D.B. Graves, G.M. Jenkins, "Self-consistent model of a direct-current glow discharge: Treatment of fast electrons", *Physical Review A*, 41 (2), pp. 1112-1125, 1990

[Tay00] S. Taylor, B. Srigengan, J. R. Gibson, D. Tindall, R. Syms, T. J. Tate, and M. M. Ahmad, "A miniature mass spectrometer for chemical and biological sensing," in *Proc. SPIE*, 2000, pp. 187–193

[Thr02] E. Thrush, O. Levi, K. Wang, J.S. Harris, S.J. Smith, A. Dittmar, D. Beebe, "Integrated semiconductor fluorescent detection system for biochip & biomedical applications," *Proc. SPIE*, 4626, pp. 289-96, 2002

[War99] M. Warren, W.C. Sweatt, J.R. Wendt, C.G. Bailey, C.M. Matzke, D.M. Arnold, S.A. Kemme, A.A. Allerman, T.R. Carter, R.E. Asbill, S. Samora, "Integrated micro-optical fluorescence detection system for microfluidic electro-chromatography," *Proc*. *SPIE*, 3878, pp. 185-92, 1999

[Web01] J. Webster, M.A. Burns, D.T. Burke, and C.H. Mastrangelo, "Monolithic capillary electrophoresis device with integrated fluorescence detector," *Anal. Chem*, 73, pp. 1622-6, 2001

[Wil01] D.S. Wilson, S. Hoyt, J. Janata, K. Booksh and L. Obando "Chemical sensors for portable, handheld field instruments," *IEEE Sensors Journal,* 1(4) pp. 256-274, Dec 2001

[Wil02] C.G. Wilson, Y.B. Gianchandani "LEd-SpEC: Spectroscopic detection of water contaminants using glow discharge from liquid electrodes," *IEEE Transactions on electron devices,* 49 (12), Dec 2002, pp. 2317-22

[Wil03A] C. G. Wilson, "Microplasmas and Microdischarges for Manufacturing and Sensing Applications", *Ph.D Thesis,* University of Wisconsin, Madison, January 2003

[Wil03B] C. G. Wilson, Y.B. Gianchandani R.R. Arslanbekov, V. Kolobov, and A.E. Wendt, "Profiling and Modelling of DC Nitrogen Microplasmas," *Jour. of Applied Physics,* 94 (5), pp. 2845-2851, 2003

[Wri07] S.A. Wright and Y.B. Gianchandani, "Controlling pressure in microsystem packages by on-chip microdischarges between thin-film titanium electrodes," *Journal of Vacuum Science and Technology B (Microelectronics and Nanometer Structures)*, 25(5), pp. 1711-1720, Sept. 2007.

[Yos01] H. Yoshiki, Y. Horike, "Capacitvely coupled microplasma source on a chip at atmospheric pressure," *Jpn. J. Appl. Phys.*, 40, pp. L360-L362, Apr. 2001

[Zel02] Q. –Y. Li, E.T Zellers, "Dual-Chemiresistor GC detector employing monolayer protected metal nanocluster interfaces," *Anal. Chem.*,74, pp. 3533-3539, 2002

[Zhu94] H. Zhu, S.M. Clark, S.C. Benson, H.S. Rye, A.N. Glazer, R.A. Mathies, "High-sensitivity capillary electrophoresis of double-stranded DNA fragments using monomeric and dimeric fluorescent intercalating dyes," *Anal. Chem.*, 66, pp. 1941-8, 1994